Resonant-cavity-enhanced Multispectral Infrared Photodetectors for Monolithic Integration on Silicon

By

Jianfei Wang

B. Eng. Materials Science and Engineering
Tsinghua University, 2003

M. Eng. Materials Science and Engineering
Tsinghua University, 2005

Submitted to Department of Materials Science and Engineering in Partial Fulfillment of the Requirements for the Degree of

Doctor of Philosophy in Materials Science and Engineering
at the
Massachusetts Institute of Technology

September 2010

Signature of Author: ___
Department of Materials Science and Engineering
August 6th, 2010

Certified by: ___
Lionel C. Kimerling
Thomas Lord Professor of Materials Science and Engineering

Accepted by: ___
Christopher Schuh
Professor of Materials Science and Engineering
Chair, Departmental Committee on Graduate Students

感谢我的父亲, 王利

对我的培养和教育

Resonant-cavity-enhanced Multispectral Infrared Photodetectors for Monolithic Integration on Silicon

by

Jianfei Wang

Submitted to the Department of Materials Science and Engineering on August 6th, 2010, in Partial Fulfillment of the Requirement for the Degree of Doctor of Philosophy in Materials Science and Engineering.

Abstract

Multispectral infrared (IR) detection has been widely employed for numerous applications including hyperspectral imaging, IR spectroscopy, and target identification. Traditional multispectral detection technology is based on the combination of broadband focal plane arrays (FPA) and spectral filters, grating spectrometers, or Fourier transform spectrometers, which requires bulky, high-cost mechanical scanning instruments and have a slow response. Hybrid structures integrating FPA and silicon readout integrated circuits (Si ROIC) greatly limit the yield and result in extremely expensive devices. Single photodetectors capable of detecting multiple wavebands simultaneously and monolithic integration with Si ROIC, however, enable dramatically simplified system design with superior mechanical robustness, and thus attract a lot of interest around the world today.

In this thesis, we focus on the development of novel IR sensitive material and resonant-cavity-enhanced (RCE) photodetector devices that address the emerging need in the field

of IR radiation detection. Polycrystalline PbTe films have been identified as the IR absorbing layers due to their high photosensitivity and fabrication flexibility; on the device side, we have established a universal design theory for multispectral detection and demonstrated fully functional mid-IR RCE photodetectors capable of monolithic integration with Si ROIC.

We have developed room-temperature-sensitized, polycrystalline PbTe films using single source thermal evaporation for detecting IR light up to 5 μm in wavelength. Thinner PbTe layers yields enhanced performance than thicker layers due to strong thickness dependence of both photo-responsivity and detectivity. Structural, electrical, and optical property studies reveal photoconductivity mechanism in the films and point out directions of further material optimization.

We have established a versatile and scalable design theory for cavity-enhanced multispectral photodetectors using phase-tuned propagation. Critical coupling condition is identified as the prerequisite to achieve near unity quantum efficiency in RCE photodetectors. Coupling-matching layers are positioned between cascaded planar resonant cavities for controlling optical phase and coupling strength between incident light and resonant modes to obtain critical coupling condition. After developing another two IR transparent layers as low and high index materials, evaporated As_2S_3 and sputtered Ge, we design and fabricate distributed Bragg reflectors (DBR) for mid-IR resonant cavities. In our design example of dual waveband RCE photodetectors, peak quantum efficiencies over 80% have been realized in both wavebands (1.55 μm and 3.6

μm) with only 50 nm and 100 nm thick PbTe IR absorbers, and spectral cross talk as low as 0.1% is obtained. Preliminary results on our first attempt of fabricated dual waveband RCE photodetectors demonstrate the two resonant cavity modes at 1.61 μm and 3.70 μm. And quantum efficiencies as high as 92% and 68% have been achieved in two wavebands respectively.

We have developed and optimized a multi-step lift-off patterning technique to fabricate RCE photodetectors on a Si platform. Single waveband RCE photodetectors for mid-IR (3.5 μm) have been designed according to critical coupling condition to achieve near unity quantum efficiency. The fabricated devices show high quantum efficiency (90%) and peak responsivity at the resonant wavelength of 3.5 μm, which is 13.4 times higher than blanket PbTe film of the same thickness. We demonstrate detectivity as high as 0.72×10^{9} $cmHz^{1/2}W^{-1}$, comparable with commercial polycrystalline mid-IR photodetectors. As low temperature processing (150 °C) is accomplished in the entire fabrication process, this demonstration paves the way for monolithic integration of RCE photodetectors with Si ROIC.

Lastly, for the first time, we fabricate and test integrated devices of single waveband (3.6 μm) RCE photodetectors and Si ROIC. Both hybrid and monolithic integration structures are investigated. We have developed the fabrication process to accommodate Si ROIC chips of only 3 mm × 5 mm in area, and successfully integrated RCE photodetectors on Si ROIC directly. Our preliminary results show high promise for monolithic integration of RCE photodetectors and Si ROIC in the future.

Thesis Supervisor: Lionel C. Kimerling

Title: Thomas Lord Professor of Materials Science and Engineering

Acknowledgements

I can still remember the excitement at the moment when seeing the "OFFER" from MIT after a long time of application and waiting in 2005. It's the happiest season in China around the year, the spring festival period, and I became such a lucky guy. It's not only the time when "a dream comes true", but also the beginning of a new dream in my life...

Being the top most school in materials science and engineering and having so many world-famous professors and researchers, at the very beginning, MIT gave me the first challenge: looking for a thesis advisor. Different professors have distinct styles: some may respond emails very quickly; some may need to schedule a discussion time beforehand with their assistants; some may be working in the office and you could knock the door directly. I haven't realized the benefit of this process until the job-hunting season, although it's much simpler when I look back now. MIT helps me build up the knowledge and research foundation through in-class courses and thesis work, as well as strengthen my confidence to express myself.

I am so proud I could join Professor Lionel C. ("Kim") Kimerling's group, Electronic Materials (EMAT) group, and luckily could be one of the several witnesses of a series of magic: integrated Ge photodetectors, integrated GeSi modulators, and mostly recently, 1st Ge laser in the world. In our EMAT family, students not only focus on their own projects and become experts in specific areas, but also learn from each other and gain broader research insight. Being my PhD thesis advisor, Kim could always help me identify the key challenges and point out possible solutions I could further explore. His knowledge,

wisdom, experience, and personality have become priceless assets I will cherish and learn from throughout my future career. Thank you for your support and guidance, Kim!

Principal Research Scientist Dr. Anu Agarwal serves as my co-advisor for my PhD study. Back to 2007, the early stage of our MIDAS project (Multispectral Infrared Detector Arrays), she has envisioned what I could learn in this project: from very basic material study, to device design and simulation, and to device fabrication and test system development. Now everything in the whole picture she described has been embedded in this thesis. After our weekly discussion and brainstorming, the complicated project at the first glance never seems unconquerable and I could make progress step by step. She is also a very warmhearted and pleasant person and I feel blessed to have the opportunity to work with her. I would like to send her my deep gratitude for all the help to me during my thesis work.

I also feel very lucky to have three senior consultants whom I could always ask for help: Dr. Piotr Becla, Professor Juejun (JJ) Hu, and Dr. Xiaochen Sun. Piotr is an amazing research scientist on photodetectors covering a very broad wavelength range, from γ ray to long infrared radiation. I could not imagine how I would make progress without Piotr's expertise in material characterization, photodetector test, and measurement system construction. Thank you for your tremendous support, Piotr! JJ and Xiaochen are my officemates in EMAT and they are pioneers working on multispectral photodetectors in the visible wavelength range. JJ gives me suggestions on every aspect for my research and also serves as the key mentor during my job search. He is always the first person

proofreading my manuscripts for publishing and giving me advice that is very to-the-point. He helps me enormously in polishing my job application package, preparing interview questions, and giving me mock interviews. Xiaochen is an expert on both software and hardware. His simulation code and electrical characterization tools really save me enormous amount of time if I were to explore all these areas as a green hand. Thank you for your great help, JJ and Xiaochen!

I sincerely thank the support of my thesis committee members, Professor Caroline Ross, Dr. Theodore Harman, and Professor Darrell Irvine. Being Professor Ross's teaching assistant in 2006 for the class "Micro/Nano Processing Technology", I became familiar with material deposition techniques and device fabrication process. I also benefit a lot from discussion with Dr. Harman on PbTe materials. He is the pioneer working on PbTe and PbSnTe single crystalline materials, and his research paves the way for me to do investigation on the polycrystalline counterpart. Professor Irvine's questions and suggestions provide me visions from another professional perspective. I feel so honored to have the world-class experts on my committee, and their help have made my thesis research ever possible.

I have worked on the ATAC (All-To-All Computing/Communication) project with Dr. Jurgen Michel, Principal Research Scientist in EMAT, and a creative physicist. I benefit a lot from the fruitful discussion with him on the intriguing scientific problems: Si ring resonators, ultra-low-loss waveguide crossing, high dynamic range Ge photodetectors, and Si nanowire solar cells. I have always enjoyed interactions with Professor Kazumi

Wada. He shares new concepts and novel ideas with me leading to brainstorm for my research in his unique way. Dr. Xiaoman Duan gives me endless support in research and career development. And I am deeply grateful for her motherly care in the everyday life, which makes me feel at home in the US. I also greatly appreciate Professor Jifeng Liu's input whenever I feel confused with some physics concept and turn to him for help. Jifeng has set a high academic standard for all the Tsinghua graduates at MIT DMSE and he is the model I have always been studying from. Dr. Anat Eshed and Mr. Mark Beals have helped us on maintaining the PVD systems and optics lab, which is very important for me to perform materials deposition and device measurement smoothly without the headache of tool's breakdown. I would also like to thank Dr. Lirong Zeng for her continuous support and encouragement during my research and job-hunting period.

I have shared office with Kevin McComber, and thanks to his "EMAT America", a serial introduction of American slang phrase, I could get use to oral English and learn more American culture. I have also shared office with JJ, Xiaochen, Michiel Vanhoutte, and Yan Cai. I will miss the office parties and all the fun discussions we had together. During my thesis work, I have enjoyed interacting with other EMAT students, post-docs, and friends: Professor Clara Dimas, Jing Cheng, Dr. Rong Sun, Timothy W. Zens, Xing Sheng, Bing Wang, Rodolfo Camacho, Vivek Singh, Neil Patel, Vivek Raghunathan, Dr. Sajan Saini, Dr. Winnie Ye, Dr. Ning-Ning Feng, Dr. Jae Hyung Yi, Dr. Samerkhae Jongthammanurak, Dr. Yasha Yi, Dr. Ching-ying Hong, and Sarah Bernardis. I would also like to thank our secretaries, Ms. Lisa Page and Ms. Mindy Baughman. They give us great help in our everyday work, and I think EMAT cannot survive without their efforts.

I would like to thank our collaborators: Professor Chang Joseph Sylvester, Dr. Shu Wei, and Mr. Ron Synowicki. Joseph and Shu Wei are trustworthy experts on electronic circuits and they provide me a higher system level perspective for my research. Collaboration with them is a very pleasant experience since we could always generate sparkling novel ideas and overcome different challenges together. Ron is a brilliant and creative expert on ellipsometry. He gives me strong support on IR ellipsometry characterization of our polycrystalline PbTe film, which is a prerequisite for the photodetector design in the next step.

Many research specialists in the MTL (Microsystems Technology Laboratory) and CMSE (Center for Materials Science and Engineering) have helped me a lot with device processing and materials characterization. Dr. Li-wen Wang gives me the first introduction to the fabrication process in MTL. Mr. Kurt Broderick has always been very helpful when I encounter problems in the fabrication process. Mr. Tim McClure and Ms. Libby Shaw are working next door from my office, and I indeed benefit a lot from this location advantage on my thin film measurement. I would also like to thank Dr. Scott A Speakman and Dr. Yong Zhang for their help on XRD and SEM/TEM experiments.

Many thanks to Ms. Maggie Le aka Mei-Yee Shek, Dr. Mihaela Balseanu, Dr. Li-Qun Xia, and Dr. Yong-Won Lee at Applied Materials (AMAT) for hosting my summer internship in 2008. I have learned so much on PECVD in AMAT. I would like to thank

Dr. Victor Nguyen, Dr. Weifeng Ye, and Dr. Xun Wang for their help in introducing me the working and everyday life in California. I have a great summer with you!

I also want to thank a lot of Professor Ce-Wen Nan and Professor Yuan-Hua Lin at Tsinghua University, Beijing, China. They co-advised my Master's study in 2003-2005 on "Electrical and Magnetic Properties of NiO-based Materials". With their guidance and support, I transformed from an undergraduate to a materials scientist and prepared myself for new challenges abroad. I could always retain momentum in my research from Professor Nan's encouragement, "No pay, no gain". 谢谢你们，南老师，林老师!

我还要深深感谢把我从小养大的奶奶和远在大洋彼岸的父母。最疼爱我的奶奶于我读书期间去逝，而我却不能见她最后一面，留下永久的遗憾...希望她在天之灵看到我今天学业上的进步，能够感到欣慰和高兴。由于历史的原因，我的父母都仅仅读到高中毕业就参加工作了。像所有的父母一样，他们对我寄予厚望。你们对我的培养，教育，和无私的爱我终身难忘！我爱你们!

Last but not least, I would like to thank my wife, Qiao Zhang (张俏). Our first meeting in the US itself is a miracle. I believe God has heard my prayer during a meteor shower, "Please let me find and marry a girl who I love and loves me." Thank you for your love, Qiao! I want to say to you: "我能想到最浪漫的事，就是和你一起慢慢变老...", meaning "The most romantic exploration I could imagine in my life, is to grow older with you together ..." Love you forever, fei.

Table of Content

---

[i] Work presented in this section has been published in: "Structural, electrical, and optical properties of thermally evaporated nanocrystalline PbTe films," *J. Appl. Phys.* **104**, 053707 (2008).

[ii] Work presented in this section will be summarized in a paper entitled "Highly textured, room-temperature-sensitized nanocrystalline PbTe film on silicon for infrared detection", to be submitted to *Phys. Rev. B.*

[iii] Work presented in this section has been published in: "One-dimensional Photonic Crystal and Photoconductive PbTe Film for Multi-spectral Mid-infrared Photodetector," in Integrated Photonics and Nanophotonics Research and Applications, (Optical Society of America, 2008), IWE6.

[iv] Work presented in this section has been published in: "Cavity-enhanced multispectral photodetector with phase-tuned propagation: theory and design," *Optics Letters* **35** (5), 742-744 (2010).

[v] Work presented in this section has been published in: "Resonant-cavity-enhanced mid-infrared photodetector on a silicon platform," *Opt. Express* **18** (12), 12890-12896 (2010).

Chapter 1. Introduction

1.1. Infrared radiation detection: challenges and opportunities

Detection of infrared (IR) radiation is now of special interest to many technical applications which rely on this part of the electromagnetic spectrum. Optical telecommunication most often utilizes 1310 nm or 1550 nm wavelengths due to the optimized performance of silica fibers in these two windows. High-performance, CMOS-compatible germanium photodiodes, which cover both telecommunication bands, have been successfully demonstrated[1]. Besides telecommunications, in longer wavelength range of 3~12 μm, infrared detection finds more applications in night vision, chemical/biological sensing, spectroscopy, medical imaging, fire-fighting, industrial product quality control, etc.

Many materials and physical phenomena have been utilized for infrared detection. From the development history of IR detectors, a simple theorem, after Norton[2], can be put as: "All physical phenomena in the range of about 0.1~1 eV can be proposed for IR detectors". The effects that have been used for IR detection include[3]: interband absorption (intrinsic photodetectors), impurity absorption (extrinsic photodetectors), intersubband absorption (Quantum Well Infrared Photodetectors, i.e. QWIPs), thermoelectric power (thermocouples), change in electrical conductivity (bolometers), thermal expansion (MEMS detectors using bimorph beams), gas expansion (Golay cell), photon drag, Josephson effect (Josephson junctions, SQUIDs), internal emission (Pt-Si Schottky barriers), different type of phase transitions, etc.

Most of the aforementioned detector technologies may be categorized into two types: photodetectors (or photon detectors) and thermal detectors. In a photodetector, incident photons generate extra electrical carriers --- electrons or holes (or both), which results an electrical output in the form of voltage (photovoltage) or current (photocurrent). Photodiodes and photoconductors that make use of intrinsic, extrinsic or intersubband electronic transitions as well as Schottky photodiodes belong to this category. By engineering the detector material and processing techniques, photodetectors can achieve high responsivity and low leakage current. A significant advantage of photodetectors is that they can operate at very high bandwidth even on the order of several hundreds of GHz[4]. However, photodetectors are generally more expensive due to complicated materials growth process and they also require cryogenic cooling for long-IR (8~12 μm) detection to suppress noise.

In a thermal detector, absorption of infrared photons leads to Joule heating of the active material. The resulting temperature change causes physical property modifications such as electrical resistance or refractive index change that can be measured. Typical thermal detectors include bolometers, most MEMS detectors and pyroelectric detectors. Compared to photodetectors, thermal detectors are usually less expensive[5]. Some thermal detectors are capable of room temperature operation, which significantly reduces the operation cost. The main drawback of thermal detectors lies in their low responsivity and slow response, whose bandwidth typically ranges from a few tenths to several hundreds of Hz.

For almost all types of IR detectors (especially for photodetectors) that work in mid-IR (3~5 μm) or long-IR (8~12 μm) range, a problem yet to be resolved is noise reduction. The energy of mid-IR or long-IR photons is small (<0.2 eV), which becomes comparable with the thermal energy of electrons at room temperature (~0.026 eV). Thermal excitation of carriers results in a significant dark current and hence large dark noise. Therefore most long-IR detectors (with exceptions of some thermal detectors[6], which still have limitations such as small bandwidth and complicated fabrication) require cryogenic cooling down to liquid nitrogen or even liquid helium temperature in order to suppress dark noise. Thus the development of low-cost, uncooled or non-cryogenically cooled mid-IR and long-IR detectors has been a focus of intensive research efforts.

Given the features of high performance, high speed, and compatibility with current Si CMOS technology, photodetectors are chosen as the topic in this thesis. Most photodetectors can be classified into two categories: photodiode (or alternatively called photovoltaic detector) and photoconductor. A photodiode utilizes the photovoltaic effect of semiconductor p-n junction or semiconductor-metal Schottky junction to generate photo-carriers, which are then collected by electrical readout. In principle a photodiode does not need external power or bias to operate, although a photodiode is often reversely biased to increase the photo-carrier collection efficiency. In contrast to a photodiode, a photoconductor (usually made of semiconductor that has appropriate band gap energy) has to be biased with a fixed voltage or current and the current flow through the photoconductor is monitored. When there is incident light, photo-generated electron-hole

pairs contribute to electrical conduction and result in a current or voltage change, i.e. photocurrent or photovoltage, which serves as the electrical output signal.

IR photodetectors are developed during the 20th century, and have evolved through several generations. The first generation, linear arrays of photoconductive detectors, has been produced in large quantities and is in widespread use today. The second generation, two-dimensional arrays of photovoltaic detectors, is now in high-rate production. Third generation IR photodetectors, which is defined by Rogalski[7] to include more innovative device structures such as two-color detectors and hyperspectral arrays, are now in development and demonstration period.

The capability of multicolor detection is highly desirable for advanced IR systems. A lot of applications could benefit from this unique characteristic, such as multi-chemical detection, temperature determination, multispectral imaging, spectroscopy, and so on. Figure 1.1 illustrates two examples of these applications. In Figure 1.1 (a), under the same excitation, different chemicals have different characteristic light emission wavelengths, thus a photodetector with multiple waveband detection capability could be employed to identify a specific type of chemical or even several different chemicals at the same time.

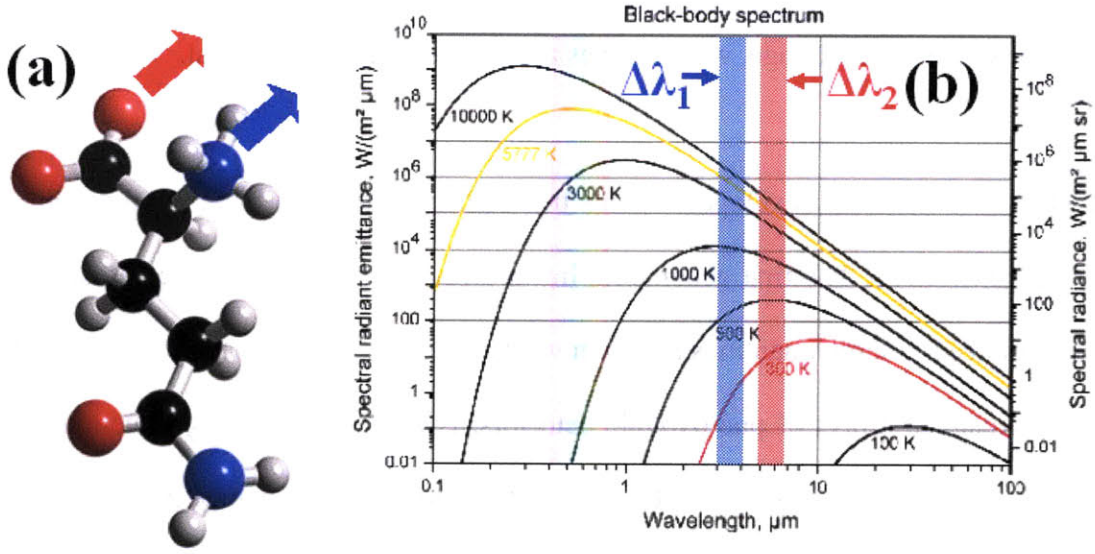

Figure 1.1 Illustration of applications with multicolor detection technology in (a) chemical sensing, and (b) temperature determination (adapted from reference 8).

Another application is temperature determination as shown in Figure 1.1 (b)[8]. By acquisition data in separate IR wavelength bands, absolute temperature of the targets in the scene can be identified. In real applications, the photodetector is pointed toward the target which is at a temperature T and at first can be treated as a blackbody described by Plank's law:

$$r(\lambda) = \frac{2h\nu^2}{\lambda^3 \exp\left[(h\nu / kT) - 1\right]} \tag{1.1}$$

where $r(\lambda)$ is the radiance per unit wavelength as a function of wavelength λ, ν is the radiation frequency, and h and k are Plank constant and Boltzmann constant. Radiance spectra of blackbodies of different temperatures are calculated and shown in Figure 1.1 (b).

In the case of two waveband detection as illustrated in Figure 1.1 (b), two measurements are performed to collect electrical signals at two separate wavelength bands centered at λ_1 and λ_2 respectively ($\Delta\lambda_1$ and $\Delta\lambda_2$). The ratio of the two detected signals can be derived as[9]:

$$\mathbb{R} = \left(\frac{\varepsilon_1}{\varepsilon_2}\right)\left(\frac{\lambda_1}{\lambda_2}\right)^5 \left(\frac{\sigma_2 \Delta\lambda_2}{\sigma_1 \Delta\lambda_1}\right) \exp\left[\frac{hc}{kT}\left(\frac{1}{\lambda_2} - \frac{1}{\lambda_1}\right)\right] \tag{1.2}$$

where ε_1, ε_2, σ_1, and σ_2 are constants related to the instrument, and c is the speed of light in vacuum. And the signal ratio can be written as:

$$\mathbb{R} = C_1 \exp\left(\frac{C_2}{T}\right) \tag{1.3}$$

where C_1 and C_2 are constants related with the instrument and two detected wavebands. Taking logarithm for both sides of Equation 1.3:

$$\ln \mathbb{R} = \ln C_1 + \frac{C_2}{T} \tag{1.4}$$

and finally T can be solved as:

$$T = \frac{C_2}{\ln \mathbb{R} - \ln C_1} = \frac{(hc/k)\left[(1/\lambda_2) - (1/\lambda_1)\right]}{\ln \mathbb{R} + \ln(\varepsilon_2/\varepsilon_1) + 5\ln(\lambda_2/\lambda_1) + \ln(\sigma_1 \Delta\lambda_1 / \sigma_1 \Delta\lambda_1)} \tag{1.5}$$

If the emissivity of the target does not very from λ_1 to λ_2, then the two waveband detection technique suggests that the temperature of the target becomes independent of its emissivity and this technique is thus inherently self-calibrated. This can be extremely beneficial for missile detection where there exists a large temperature difference between the surface of the missile and the missile's exhaust plume.

Traditionally, multispectral detection capability has been realized by several approaches, including spatial registration, i.e. color filter array[10,11], temporal registration (mechanical filter wheel)[12], tandem structure[13], and quantum well IR photodetectors (QWIPs)[9,14,15]. The first two methods require cumbersome spatial alignment and temporal registration, thus complicate the photodetector and silicon readout integrated circuits (Si ROIC) design and raise the issue of system reliability. Thus a single photodetector with multispectral capabilities that circumvent these problems is highly desirable because it can significantly simplify the design and reduce the size, weight and power consumption. In a tandem detector, the top detector serves as a pass band filter for the bottom detector. The problem associated with this design is that only certain spectral bands are accessible due to limited material choices. Despite their high leakage current, QWIPs are capable of multispectral detection by varying applied bias. However, the time multiplexing involved prohibits simultaneous detection of different wavelength within a single pixel[16]. QWIPs based on III-IV alloys also suffer from low quantum efficiency (< 10%) due to the intrinsic low IR absorption coefficient and polarization sensitivity, thus have limited device optimization strategy[17]. HgCdTe and InSb photodiodes could also offer multispectral capability in the near-IR (1~3 μm), mid-IR (3~5 μm) and long-IR (8~12 μm) atmospheric transparency windows[9]. Recently, three-color HgCdTe (mercury cadmium telluride, MCT) photodiodes have been demonstrated, but their spectral cross talk is still large (> 10%)[18]. The challenge with these crystalline alloys is the difficult and expensive material and device fabrication technology for large-area detector arrays, which require tight material and mechanical specifications and extensive molecular beam epitaxy (MBE) expertise and proofing.

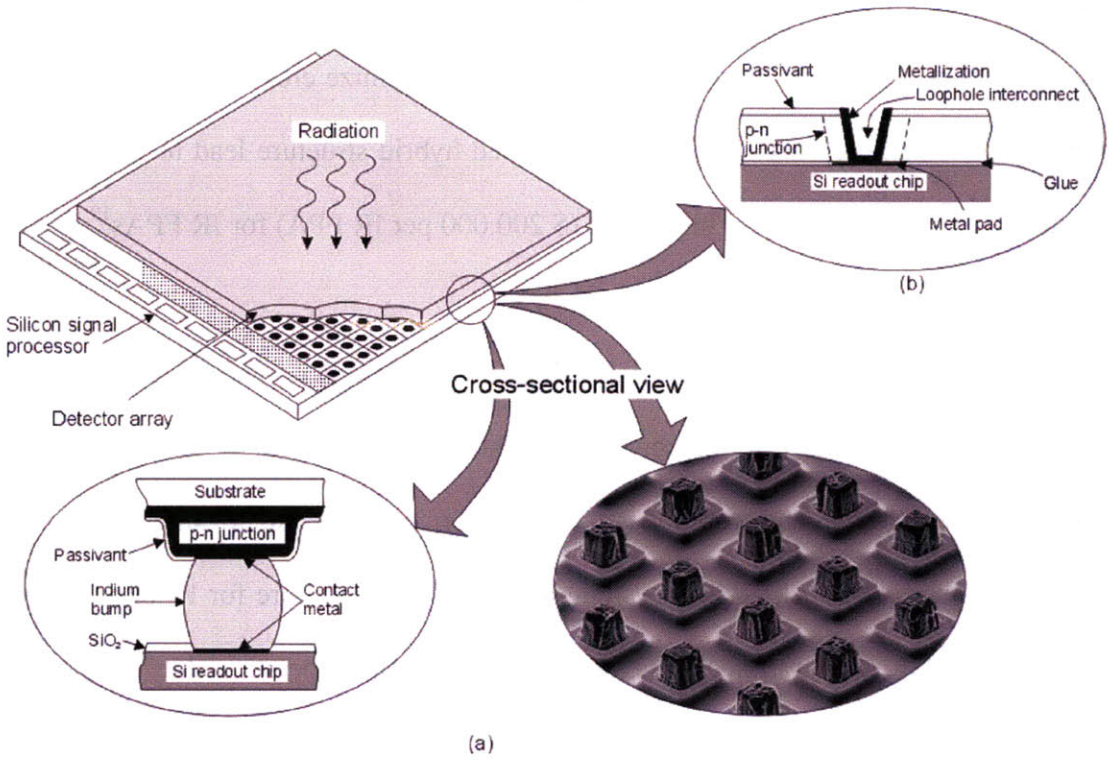

Figure 1.2 Hybrid IR FPA with signal detector array and Si ROIC: (a) indium bump technique; (b) loophole technique[9].

Furthermore, as shown in Figure 1.2, hybrid structures are commonly adopted for the integration of IR photodetector arrays and Si ROIC to form IR focal plane arrays (FPAs)[9]. Even though IR photodetector array and Si ROIC could be optimized independently, these two parts have to be integrated by using either indium bumps (indium bump technique) or glue (loophole technique). Due to the backside illumination, photons will have to pass through the photodetector array substrate. In HgCdTe hybrid FPAs, transparent CdZnTe substrate is usually chosen. However, because of thermal mismatch between the photodetector array and Si ROIC, the maximum chip size is greatly limited (on the order of 20 mm square). To solve this problem, technology based

on alternative substrates such as sapphire or silicon for HgCdTe layer epitaxy has been developed. But when using these opaque materials, substrates must be thinned to below 10 μm to obtain sufficient quantum efficiencies and minimize cross talk. The challenges arising from material epitaxy and flip-chip bonded hybrid structure lead to unacceptable low yield (~ 5%) and extremely high price ($ 200,000 per IR FPA) for IR FPAs[19].

This thesis addresses the above problems of high cost and limited intelligence capabilities of current multispectral infrared technologies. Three major challenges are identified and targeted: (1) expensive and complicated fabrication process due to single crystalline materials grown by MBE/MOCVD system, and hybrid architecture for IR photodetector array and Si ROIC integration; (2) heavy and cumbersome operation due to cryogenic cooling to suppress noise in mid-IR; (3) lack of **TRUE** multispectral detection methodology, i.e. multiple IR wavebands detected by single photodetector at the same time. To solve the first challenge, a monolithic integration approach have been proposed and demonstrated. Figure 1.3 shows the integrated architecture schematically. Polycrystalline and amorphous materials are investigated and developed to detect IR radiation. Without lattice match constraint, materials can be deposited onto Si ROIC directly and photodetectors can be fabricated by standard photolithography. Less expensive deposition techniques like thermal/e-beam evaporation and sputtering can be used to deposit multiple materials, giving more flexibility in choosing materials and designing photodetectors. For the second challenge, since most types of noise including generation-recombination noise, shot noise, and Johnson noise scale with the IR absorbing material's volume, the small IR absorber thickness will help to reduce detector

noise and increase signal-to-noise ratio. In order to maintain high quantum efficiency or responsivity at the same time, Figure 1.4 shows a schematic resonant-cavity-enhanced (RCE) photodetector design, which could trap light of specific wavelength in the IR absorbing layer to enhance absorption. This strategy will greatly relieve the requirement of cryogenic cooling (~77 K) and enable thermoelectric cooling (TEC), which can be more easily integrated with photodetectors and Si ROIC. For the third challenge, a novel design theory of RCE multispectral photodetectors has been developed and demonstrated both theoretically and experimentally, which can be generalized to detect virtually any arbitrary number of wavelengths in a single photodetector.

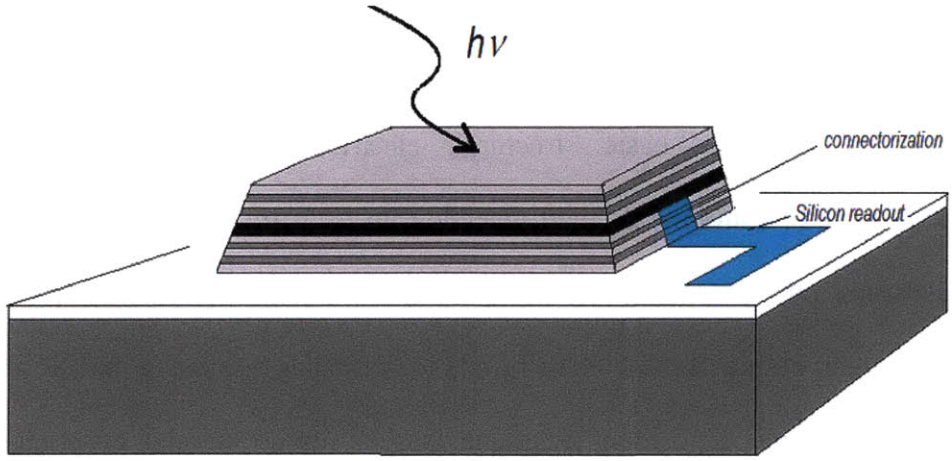

Figure 1.3 Schematic illustration of integrated architecture with photodetectors fabricated onto Si ROIC monolithically.

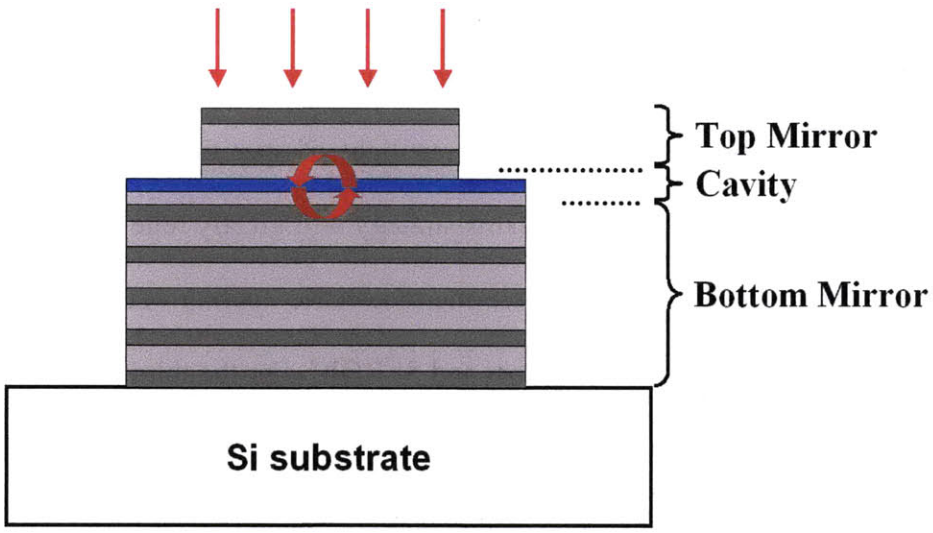

Figure 1.4 Resonant-cavity-enhanced (RCE) photodetector design employed to trap light of specific wavelength in the thin IR absorbing layer (blue color) to maintain high quantum efficiency.

1.2. Outline of the thesis

Chapter 2 discusses the basic structural, electrical, and optical properties of polycrystalline PbTe films for IR light detection up to 5 μm in wavelength. We begin with discussion on how we choose appropriate polycrystalline materials for this wavelength range. Polycrystalline PbTe film is identified as promising mid-IR absorbing layer given its simple deposition technique (single source thermal evaporation) and preliminary results on photoconductivity. Microstructure study confirms the films are stoichiometric single-phase polycrystalline with (200) texture. Electrical properties of the films are analyzed in the framework of a grain boundary channel conduction model. Index of refraction and extinction coefficient of PbTe film are extracted from infrared spectroscopic ellipsometry measurement in the wavelength range of 2~8 μm, yielding an optical band gap of 0.386 eV and evidence for the presence of an Urbach band tail. The optical band gap is larger than the typical value for bulk material due to quantum

confinement effect. The electrical and optical property studies are important and necessary to understand the mechanism of photoconductivity in polycrystalline PbTe films and photodetector design, which will be discussed in more detail in chapter 3 and chapter 4 afterwards.

Chapter 3 demonstrates the feasibility of using thin polycrystalline PbTe film as IR absorbing layer in order to enhance signal-to-noise ratio. Photoconductivity experiment demonstrates the strong dependence of responsivity and detectivity on film thickness, and film as thin as 100 nm can be used as IR absorbing layer in the wavelength range of 0.8~5 μm. Microstructure evolution is revealed when films of different thicknesses (0.1~1 μm) are compared. We discuss the photoconductivity mechanism and demonstrate long-term stability in polycrystalline PbTe films. Direct relationship is constructed for responsivity with material properties, device dimensions, and external bias current. All possible noises in polycrystalline PbTe photoconductors are evaluated and compared with experimental results. Johnson noise is identified as dominant intrinsic noise in PbTe photoconductors and a model predicting Johnson-noise-limited detectivity is developed.

Chapter 4 discusses a novel design of cavity-enhanced multispectral photodetectors using phase-tuned propagation. We begin with design and fabrication of mid-IR distributed Bragg reflectors (DBR), or mirror stacks used for cavity structures. Based on individual layer's optical properties, quarter wavelength stack of thermally evaporated As_2S_3 and sputtered Ge films is designed, fabricated, and tested. We demonstrate photonic band gap between 3 μm and 5 μm and reflectance higher than 99% in the range of 3.5~3.8 μm for

DBR designed to reflect 3.6 μm light. Then we theoretically analyze the novel design of resonant-cavity-enhanced (RCE) photodetectors capable of sensing multiple wavelengths simultaneously in a single photodetector. In our design example, peak quantum efficiencies over 80% have been realized in both wavebands (1.55 μm and 3.6 μm) with only 50 nm and 100 nm thick PbTe IR absorbers, and spectral cross talk as low as 0.1% is obtained. The design is based on phase-tuned propagation of resonant modes in cascaded planar resonant cavities, and due to its versatility and scalability, this concept can be generalized to detect virtually any arbitrary number of wavelengths. Preliminary results on our first attempt of fabricated dual waveband RCE photodetectors demonstrate the two resonant cavity modes at 1.61 μm and 3.70 μm. And quantum efficiencies as high as 92% and 68% have been achieved in two wavebands respectively.

Chapter 5 presents the design, fabrication, and test of single waveband RCE photodetectors on a silicon platform for mid-IR (3.5 μm). Single waveband RCE photodetectors can serve as building blocks for multiple waveband RCE photodetectors, so this step is essential for the development of multispectral photodetectors. We demonstrate high quantum efficiency (90%) and enhanced peak responsivity at the resonant wavelength of 3.5 μm, which is 13.4 times higher compared to blanket PbTe film of the same thickness. Detectivity as high as 0.72×10^{9} $cmHz^{1/2}W^{-1}$ has been obtained, comparable with commercial polycrystalline mid-IR photodetectors. As low temperature processing (150 °C) is implemented in the entire fabrication process, this demonstration shows promise for monolithic integration of RCE photodetectors with Si readout integrated circuits (Si ROIC).

Chapter 6 presents the preliminary results on our first attempt in fabricating single waveband (3.6 μm) RCE photodetectors integrated with Si ROIC. Both hybrid and monolithic integration strategies are evaluated. We have developed the fabrication process enabling monolithic integration of RCE photodetectors on Si ROIC chips with the area of only 3 mm × 5 mm. The devices are characterized by photoconductivity measurements. Under monochromatic light illumination, no output voltage has been observed due to low bias current and limited cooling restricted by Si ROIC. Under broadband light source illumination, a linear relationship between the output voltage from Si ROIC and the bias current is obtained as expected, which shows high promise for monolithic integration of RCE photodetectors and Si ROIC in the future.

Chapter 7 summarizes major results and achievements of this thesis, and presents the directions of future work.

Chapter 2. Polycrystalline lead telluride (PbTe) films[20]

The wavelength range of our interest includes near-IR (1~3 μm) and mid-IR (3~5 μm). Identifying and developing appropriate photoactive material for the range of 1~5 μm become the key challenges which should be solved with the first priority. Figure 2.1 shows various photodetector materials in the spectral range of 1~14 μm which are mostly studied or commercially available[7]. As discussed before, HgCdTe alloys lack monolithic integration capability with Si ROIC, and thus are out of consideration. III-V compounds and alloys such as InAs and InSb are mostly grown by metalorganic chemical vapor deposition (MOCVD) and therefore have the same issue. Then the only two candidates left in Figure 2.1 are PbTe and PbSe, both of which belong to the so-called lead salts or lead chalcogenides (the third one is PbS). Highly sensitive mid-IR PbSe photodetectors have been demonstrated through annealing as-deposited polycrystalline films in an oxidizing atmosphere[21,22]. However, this annealing process has to be done at high temperatures which is beyond the thermal budget of Si ROIC. Thus the only candidate left is PbTe.

2.1. Band structure of PbTe

PbTe is polar semiconductor in which the bonding to a large extent is due to the electrostatic forces between the ions forming the crystal. This ionic character is reflected by the fact that PbTe has the sodium chloride or rock salt structure. Its space lattice is face-centered cubic, with a basis of one Pb ion and one Te ion associated with each lattice point. People have extensively investigated the band structure of PbTe both

experimentally and theoretically. The first Brillouin zone of PbTe is shown in Figure 2.2 (a) and the band structure is shown in Figure 2.2 (b)[23].

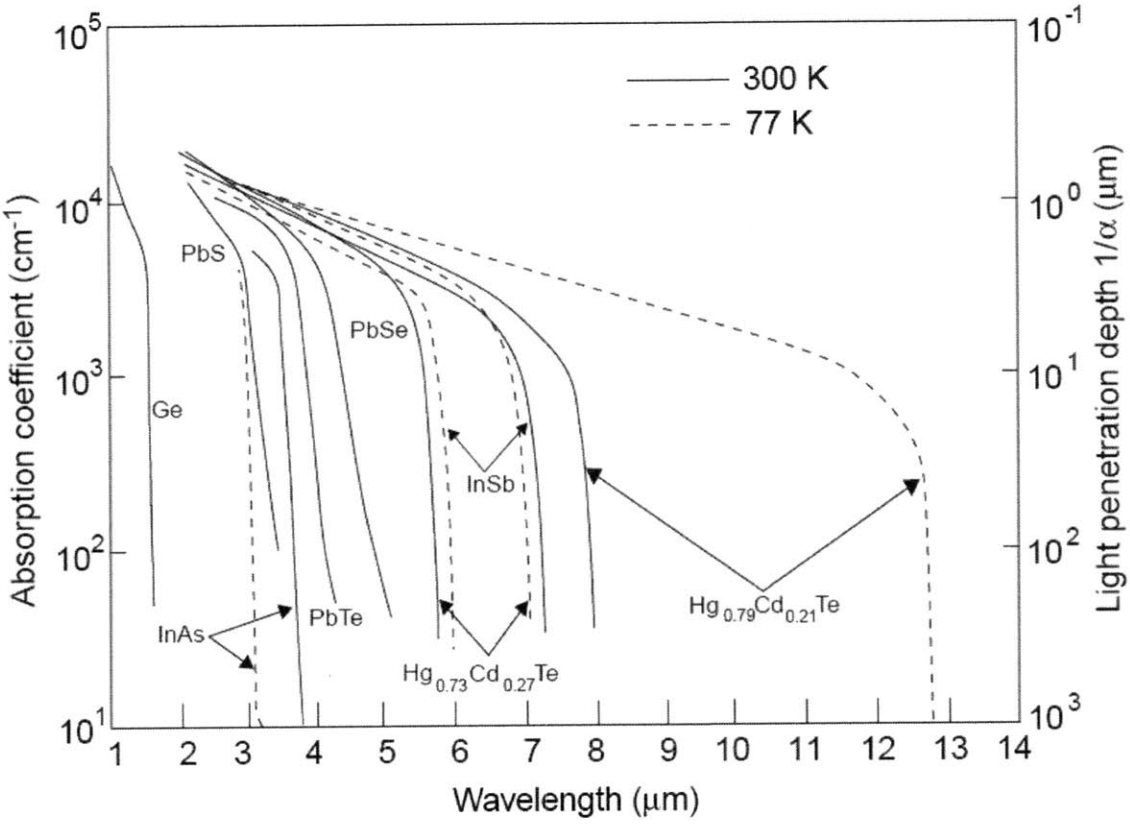

Figure 2.1 Absorption coefficients of various photodetector materials in the spectral range of 1~14 μm[7].

In the first Brillouin zone, the eight equivalent L points are each at the center of a hexagonal Brillouin zone face, at its intersection with a [111] direction. The six equivalent X points are each at the center of a square zone face at its intersection with a [001] direction. The Γ point is at the zone center. The experimental results indicate that the surfaces of constant energy for both the conduction and valence bands are prolate ellipsoids of revolution. The centers of the ellipsoids are at L points and the major exes are in [111] directions. Thus there are eight equivalent constant energy ellipsoids for the

conduction band states and eight for the valence band states. The portions of two such ellipsoids lying inside the first zone are shown in Figure 2.2 (a).

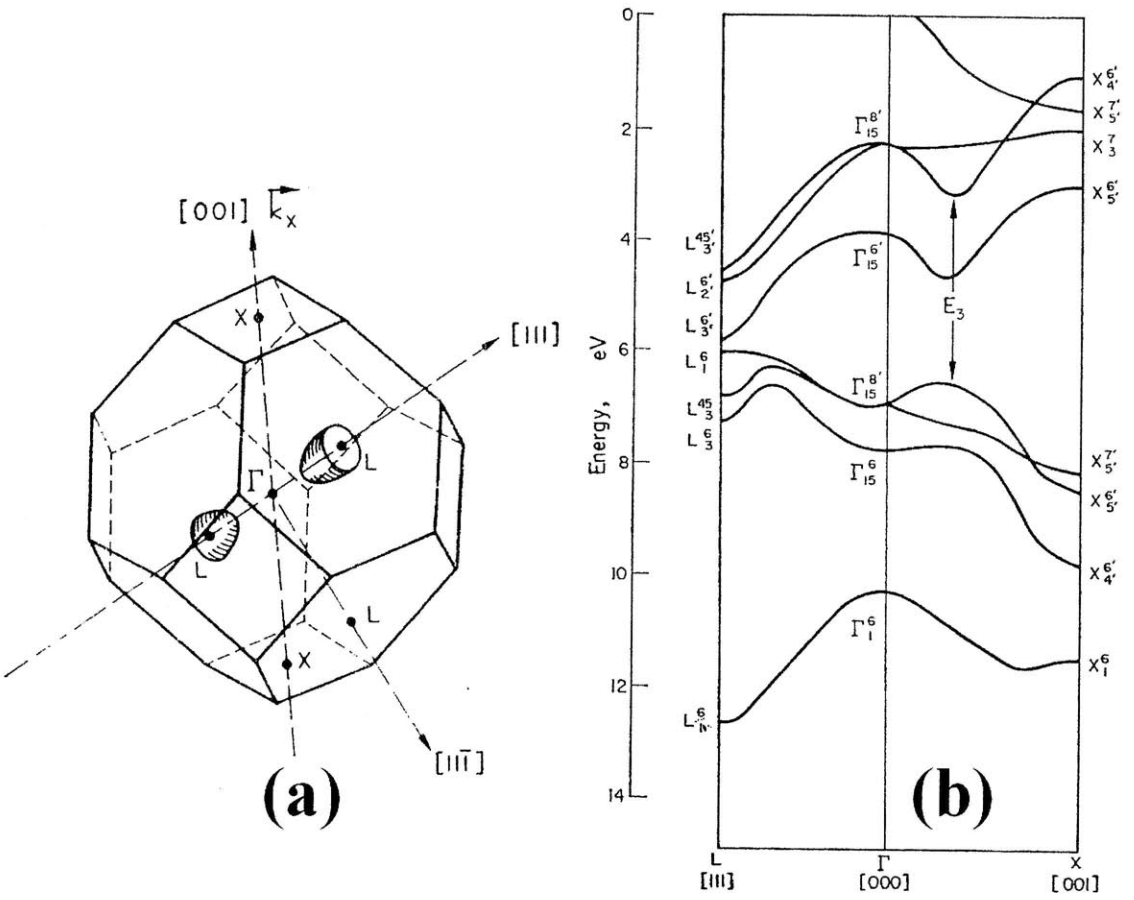

Figure 2.2 (a) First Brillouin zone of PbTe: the symmetry points Γ, L, and X are shown, as are two ellipsoids of constant energy (after Dalven[23]). (b) Band structure of PbTe: the minimum energy gap E_g is direct at L: $L_1^6 \rightarrow L_{3'}^{6'}$. The higher energy transition E_3 is also shown (adapted from the results of Lin and Kleinman[24]).

Figure 2.2 (b) shows the energy E of an electron as a function of wave vector k for two directions in k space. The right-hand side shows E as a function of k in [001] direction from the zone center (Γ). The left-hand side shows E as a function of k in [111] direction

from the Γ point. The symbols (e.g., Γ_1^6) denote symmetry properties of the bands. An energy scale has been added with an arbitrary zero. The valence band maximum and the conduction band minimum both occur at the L point, which results in a direct minimum energy gap E_g. Experimental evidence for the fact that E_g is direct is the observation of laser emission at the gap energy from PbTe p-n junction lasers.

The experimental values of E_g are plotted as a function of temperature in Figure 2.3[25,26]. The data exhibit the well-known and unusual positive temperature coefficient (dE_g/dT) of the direct energy gap E_g. The variation of E_g between 80 K and 373 K is linear and the slope (dE_g/dT) calculated is 4.5×10^{-4} eV/K. The energy gap of PbTe at 300 K is 0.31 eV corresponding to a cut-off wavelength of 4 μm. Thus in order to obtain a cut-off wavelength at 5 μm, PbTe should be cooled down to 162 K (-111 °C). Commercial multi-stage thermoelectric cooler (TEC) is available which could cool the materials down to -100 °C corresponding to a cut-off wavelength of 4.9 μm[27].

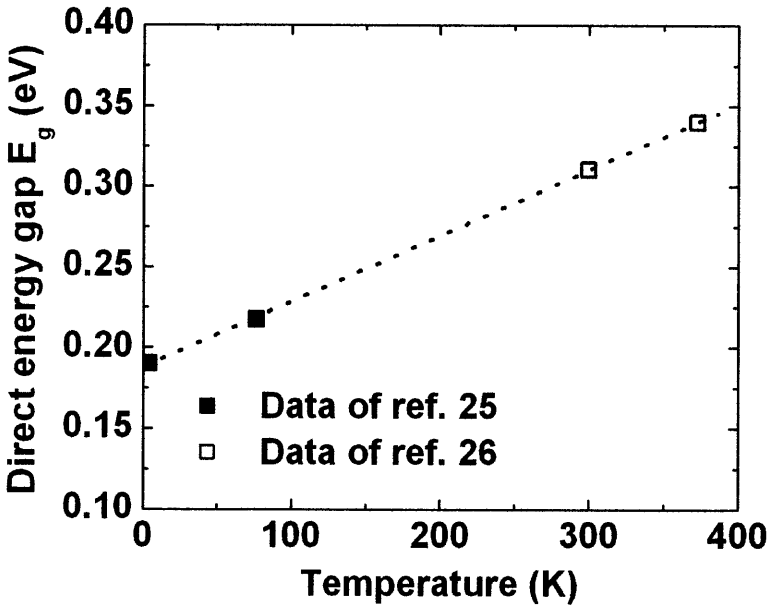

Figure 2.3 Temperature dependence of the direct energy gap E_g of PbTe. The straight dotted line is for guidance to show the linear dependence.

Another attractive character of PbTe is the formation of $Pb_{1-x}Sn_xTe$ alloy with narrower direct band gap. From phase diagram shown in Figure 2.4, PbTe and SnTe can be alloyed to form complete solid solution continuously over the entire composition range at relatively low alloying temperature[28]. Figure 2.5 shows the energy gap of single crystal $Pb_{1-x}Sn_xTe$ as a function of x, the mole fraction of SnTe, at 12 K and 77 K respectively[29]. The band gap energy of the alloy decreases gradually with increasing SnTe component, thus through alloying with SnTe, the light absorption and photo-detection spectrum of PbTe can be extended to longer wavelength, e.g. long-IR (8~12 μm). Figure 2.6 is the responsivity spectrum of single crystal $Pb_{1-x}Sn_xTe$ photoconductors, demonstrating photoconductivity covering both mid-IR and long-IR (3~12 μm) at 77 K[30].

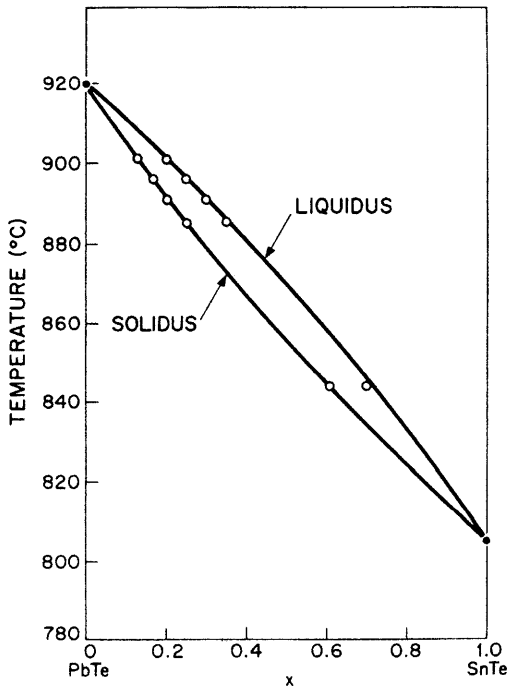

Figure 2.4 Temperature-composition phase diagram of the pseudobinary $Pb_{1-x}Sn_xTe$ system[28].

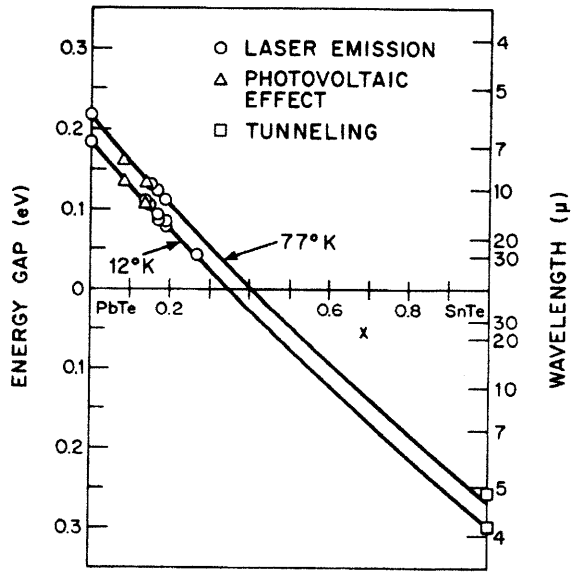

Figure 2.5 Energy band gap of single crystal $Pb_{1-x}Sn_xTe$ as a function of x, the mole fraction of SnTe, at 12 K and 77 K[29].

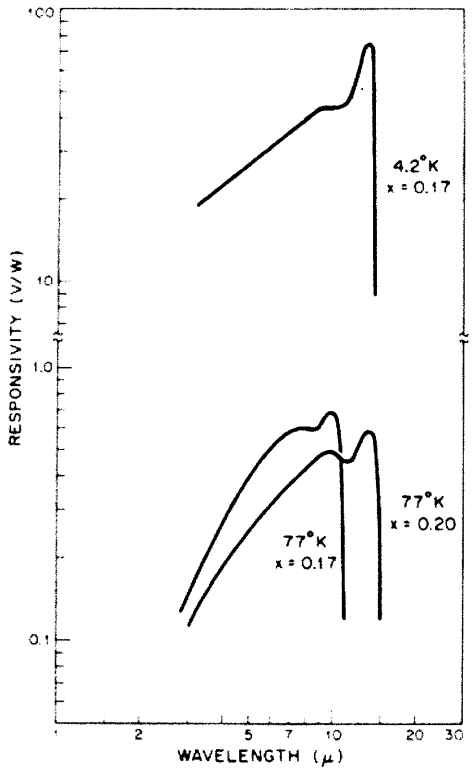

Figure 2.6 Responsivity of single crystal $Pb_{1-x}Sn_xTe$ photoconductors[30].

2.2. Structural properties

Different deposition techniques have been employed for PbTe film deposition, including flash evaporation[31,32] and a hot-wall technique[33]. We use single source thermal evaporation to deposit PbTe films. Commercial bulk PbTe of 99.999% purity is pulverized and used as the source material for thermal evaporation. Optically polished CaF_2 discs, pre-cleaned glass microscope slides, and oxide coated Si wafers (4" Si wafers with 400 nm thermal oxide) are used as starting substrates. The thermal evaporation runs are carried out at a base pressure of 5×10^{-7} Torr. The substrates are held at room temperature throughout the depositions. The film thickness and the deposition rate are monitored in situ through a pre-calibrated quartz crystal oscillator. The deposition rate is maintained at 5~7 Å/s.

Thickness of the films is measured by a surface profilometer and the measurement gives a film thickness of 950 nm ± 4% across an entire 4" substrate. A JEOL JXA-733 superprobe equipped with WDS attachment is employed for film composition analysis, and it shows an atomic ratio of Pb to Te close to unity within the error of WDS measurement (~ 1%), indicating that the films are nearly stoichiometric. An XRD spectrum of PbTe film deposited on a glass slide is shown in Figure 2.7. As expected, the film contains a single face-centered-cubic (FCC) crystalline phase with a rock salt structure. The diffraction peak intensities in the measured spectrum differ from those quoted from the standard PDF card[34], indicating (200) texture in the film deposited on an amorphous glass substrate. Films on other substrates show a similar preferred orientation. The texture structure suggests that (200) is the preferred film growth orientation due to its low surface energy. This is consistent with the result of co-evaporated PbTe thin films on glass substrates reported by Khairnar et al, which showed that (200) diffraction peak intensity varied with film thickness and substrate temperature during deposition[35].

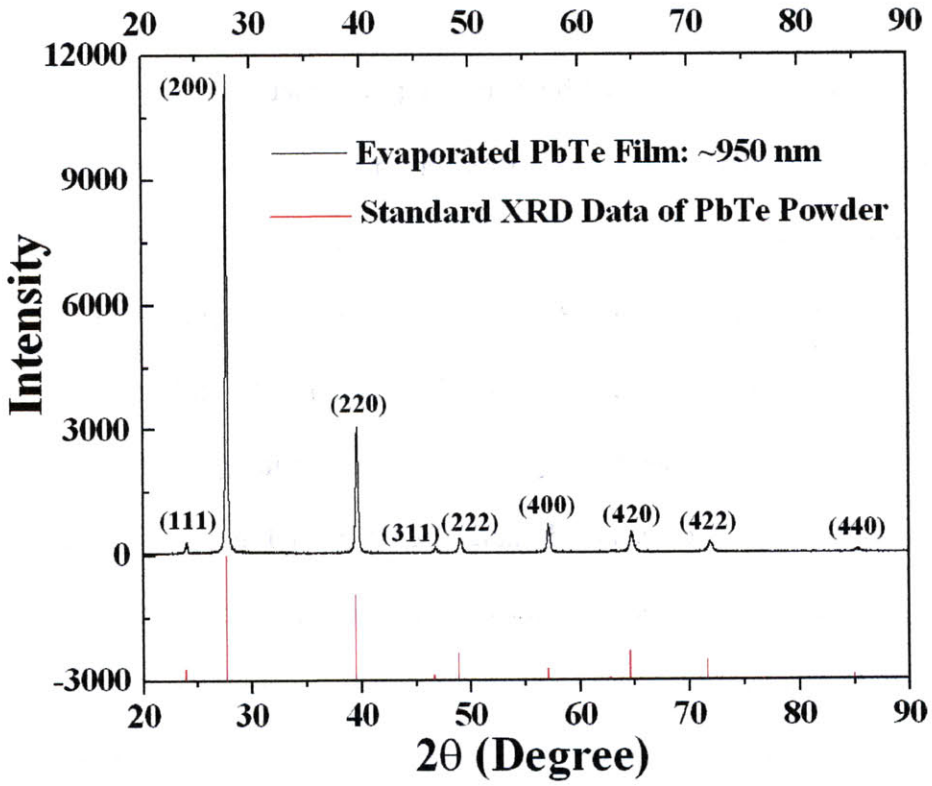

Figure 2.7 XRD spectrum of thermally evaporated PbTe film on a glass substrate: the film is polycrystalline single FCC phase with (200) texture. Standard XRD data of PbTe powder sample from Ref 34 is also shown at the bottom for comparison.

Figure 2.8 shows the surface morphology of PbTe films on (a) a glass slide substrate and (b) a 400 nm SiO_2 coated Si substrate obtained by AFM. Both films show similar surface features: they have a grain size in the range of 50 to 100 nm and root mean square (RMS) surface roughness of 14 to 16 nm. The microstructural and morphological similarity between PbTe films deposited on different substrates is not coincidental and is indicative of the polycrystalline nature of PbTe films. From a device integration perspective, this roughness value has a negligible effect on the performance of photonic crystal cavities operating in mid-IR wavelengths according to Maskaly et al[36,37].

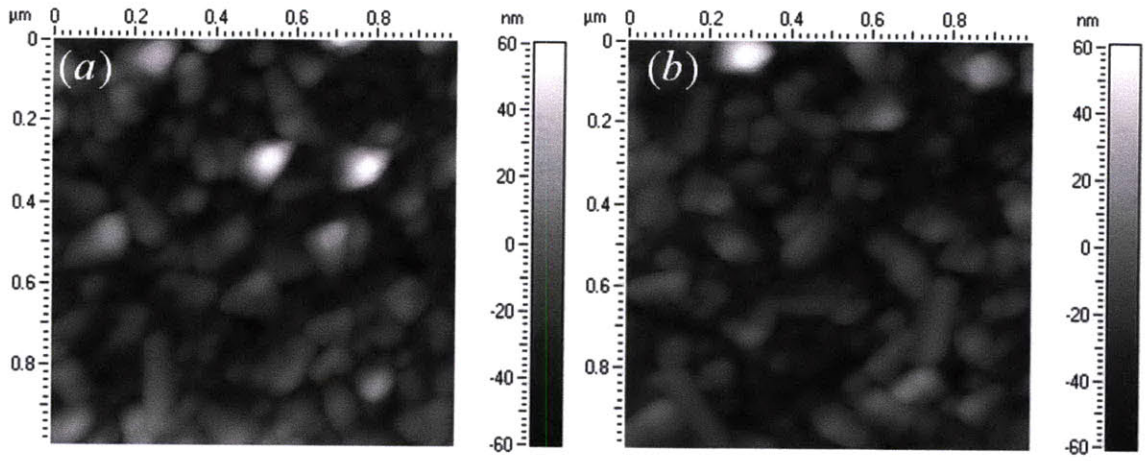

Figure 2.8 AFM surface height images of thermally evaporated PbTe films on (a) a soda-lime glass substrate, and (b) a Si substrate coated with 400 nm thermal oxide.

2.3. Electrical properties

Tin (Sn) electrodes are evaporated onto PbTe films through shadow mask and used as metal contacts for electrical conductivity and Hall measurements. In the conductivity measurement, current-voltage (I-V) curves are recorded using a digital deep level transient spectroscopy (DLTS) system at temperatures from 80 K to 340 K. Voltage is applied through a pair of metal probes and the current flowing through the two metal contacts is monitored. We observe linear I-V characteristics in the whole temperature range, confirming ohmic nature of the contacts. Conductance at different temperatures is extracted by least squares linear fit of I-V curves, and error of the measurement is estimated to be smaller than 1 pS. Hall measurement is performed at room temperature using the van der Pauw configuration in a magnetic field of 1 T.

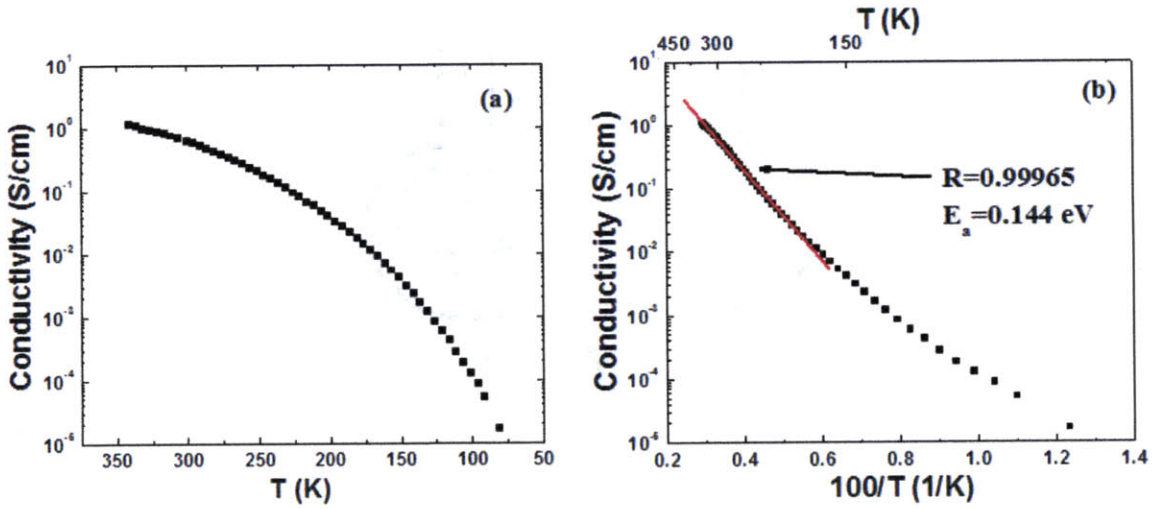

Figure 2.9 DC electrical conductivity of thermally evaporated PbTe film: (a) conductivity data on a logarithm scale plotted as a function of temperature; lack of linear dependence in the plot suggests that electrical conduction in PbTe is not dominated by the percolation process; (b) conductivity data plotted as a function of inverse temperature showing thermal activation nature of conduction at high temperature (> 200 K) and a weaker temperature dependence at lower temperatures. The black dots are experimental data, and the red solid line is linear curve fit of the data at high temperature (> 200 K).

The PbTe film shows p-type conduction and carrier mobility of 53 cm^2/Vs from Hall measurement. The measured carrier concentration is 2.1×10^{17} cm^{-3} at room temperature. To elucidate the conduction mechanism in thermally evaporated PbTe films, temperature dependence of film DC electrical conductivity is measured and the result is plotted in Figure 2.9. Qualitatively, our result gives a DC conductivity temperature dependence similar to that of In-doped PbTe films reported by Dashevsky and Komissarova[38]: the conductivity exhibits thermally activated behavior in the high temperature range and relatively weak temperature dependence at low temperatures, suggesting different regimes where distinct conduction mechanisms are dominant.

Several models have been previously proposed for electrical conductivity in PbTe and other chalcogenide films at different temperatures. Gudaev et al. proposed a percolation model to explain the temperature dependence of electrical conductivity in polycrystalline chalcogenide films, which suggest that DC conductivity obeys the inverse Arrhenius law:

$$\sigma \propto \exp(T/T') \tag{2.1}$$

where T' is a constant determined by the percolation parameters[39]. However, such an inverse Arrhenius temperature dependence is not observed in our films, as is shown in Figure 2.9 (a).

Alternatively, conduction channels on the surface of crystal grains have been suggested to be the main electronic transport path in polycrystalline lead chalcogenide films[40]. In the framework of this theory, adsorbed oxygen or lattice defects lead to formation of acceptor states in grain boundaries. These acceptor states induce band bending on the surface of crystalline grains, and thus p-type conduction channels are formed on the grain surfaces. A schematic of the band diagram on near a grain boundary is shown in Figure 2.10. According to this model, DC electrical conductivity is thermally activated and can be described by an activation energy $E_a = (E_F - E_V) - E_S$, where $(E_F - E_V)$ is the energy separation between valence band edge and Fermi level in crystalline PbTe grains and E_S corresponds to the band bending. Figure 2.9 (b) shows the conductivity plotted as a function of inverse temperature, and in the high temperature range (approximately > 200 K) the temperature dependence of conductivity can be well fitted with a single activation energy value of 0.144 eV. This model also agrees with our observation of p-type conduction in the films. However, since the exact carrier concentration and hence Fermi

level in the grains are unknown, we cannot infer the value of band bending from the activation energy E_a.

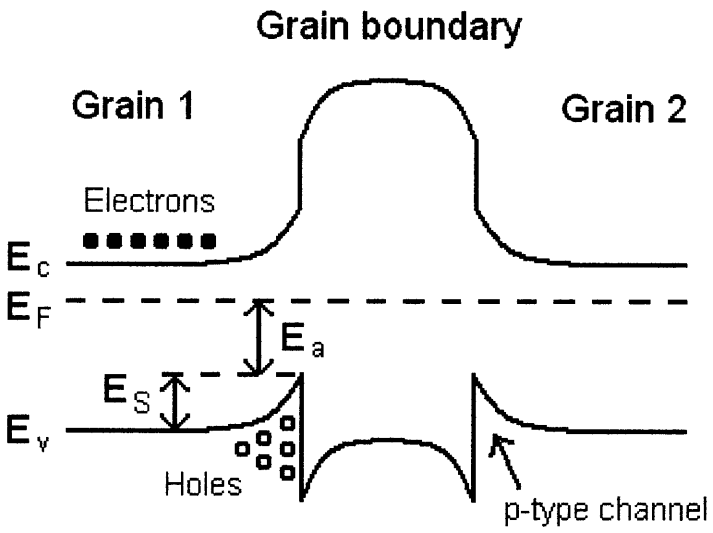

Figure 2.10 Schematic energy band diagram near a grain boundary, and the relevant energy points are: E_c conduction band edge; E_v valence band edge; E_F Fermi level; E_S bend banding on the surface of a grain; and E_a activation energy of electrical conduction according to the grain boundary conduction channel model.

In the low temperature range (< 200 K) we can see clear deviation from the thermal activation model with weaker temperature dependence. Based on impedance spectroscopy measurement results, Komissarova et al. inferred that tunneling transport through grain boundary barriers dictates the electrical properties of In-doped polycrystalline PbTe films at low temperature[38]. Alternatively, hopping conduction between localized states in the mobility gap also exhibit weak temperature dependence characterized by the famous $T^{-1/x}$ law, where x is a constant greater than one depending on the system dimensionality and the form of density of states function near Fermi level[41].

Hopping conduction has been identified to be a major electronic transport mechanism in many chalcogenide materials, especially amorphous glasses[42]. In order for hopping transport to occur, two conditions need to be met: (1) Fermi level should locate within the mobility gap; and (2) there should be non-vanishing density of states near Fermi level. Lattice defects in grains or near grain boundaries often lead to localized states in the mobility gap, possibly contributing to hopping conduction. The position of Fermi level in the films with respect to mobility edges, however, is a question for further investigation. More experimental efforts will be necessary to confirm the low temperature conduction mechanism in the films.

2.4. Optical properties

PbTe films evaporated on CaF_2 are used for optical property measurements given the IR transparency of CaF_2. A Cary 5E UV-Vis-NIR dual beam spectrophotometer and a Nicolet Magna 860 Fourier transform infrared spectrometer (FTIR) are used to record the transmittance spectra in the wavelength ranges of 0.4~3.0 μm and 3.0~13 μm respectively. Refractive index and extinction coefficient of the PbTe films are extracted by fitting the amplitude ratio upon reflection, the phase shift, and transmission intensity data, all measured on a variable angle infrared spectroscopic ellipsometer (IR-VASE of J. A. Woollam Co.) from 2 μm to 8 μm wavelength.

The transmittance spectrum of the PbTe film on CaF_2 disc is shown in Figure 2.11. The fringes of the curves are due to the interference effect at certain wavelength, and the distance between the fringes is dependent on both the refractive index and the thickness

of the films[43]. From Figure 2.11, one observes transmittance peak value around 3.3 μm is much lower than the value around 4.8 μm, indicating the absorption edge is around this wavelength range.

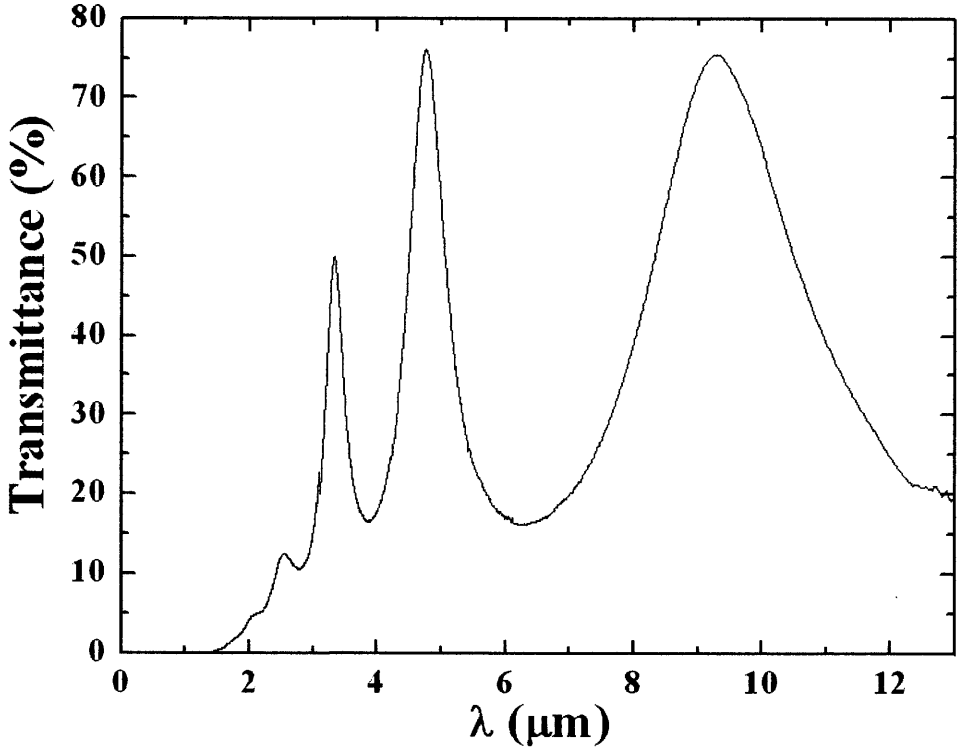

Figure 2.11 Transmittance spectrum of PbTe film on CaF_2 disc.

Figure 2.12 shows the measured refractive index and extinction coefficient of PbTe films at 2~8 μm wavelengths. Absorption coefficient α can be calculated from extinction coefficient using the following relation:

$$\alpha = \frac{4\pi k}{\lambda} \tag{2.2}$$

where k is the extinction coefficient and λ is the wavelength, and is plotted in Figure 2.13. Optical absorption due to electronic transition across the band gap in a direct gap semiconductor obeys:

$$\alpha = \alpha_0 \left(h\upsilon - E_g \right)^{1/2} \tag{2.3}$$

where α_0 is a constant determined by the joint density of states in the parabolic bands, $h\upsilon$ denotes incident photon energy, and E_g is the optical band gap energy[44,45].

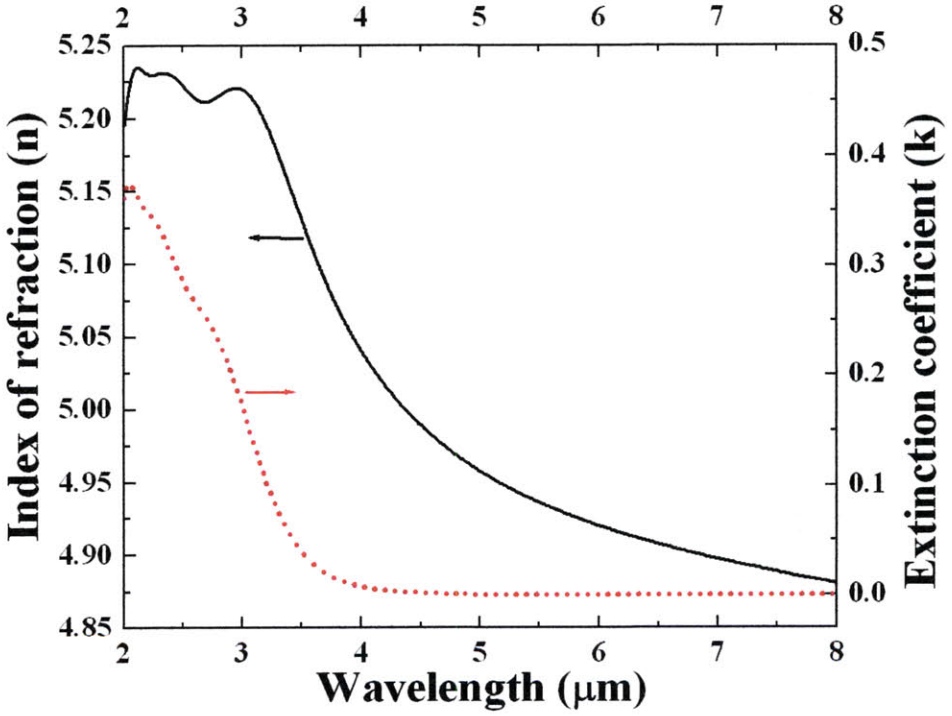

Figure 2.12 Refractive index and extinction coefficient of PbTe film measured by infrared ellipsometry.

Fitting of our experimental data using the formula (shown in Figure 2.13 inset) yields an optical band gap of 0.386 eV. In addition to optical transitions across the band gap, sub-band gap absorption is identified from 0.2 eV to 0.4 eV where the absorption coefficient spans almost four orders of magnitude. This sub-band gap absorption is absent in single

crystalline PbTe bulks and films, and is attributed to Urbach band tail resulting from defect states in polycrystalline materials. Optical absorption by Urbach band tail can be described by the formula:

$$\alpha \sim \exp\left(\frac{h\upsilon}{E_e}\right) \tag{2.4}$$

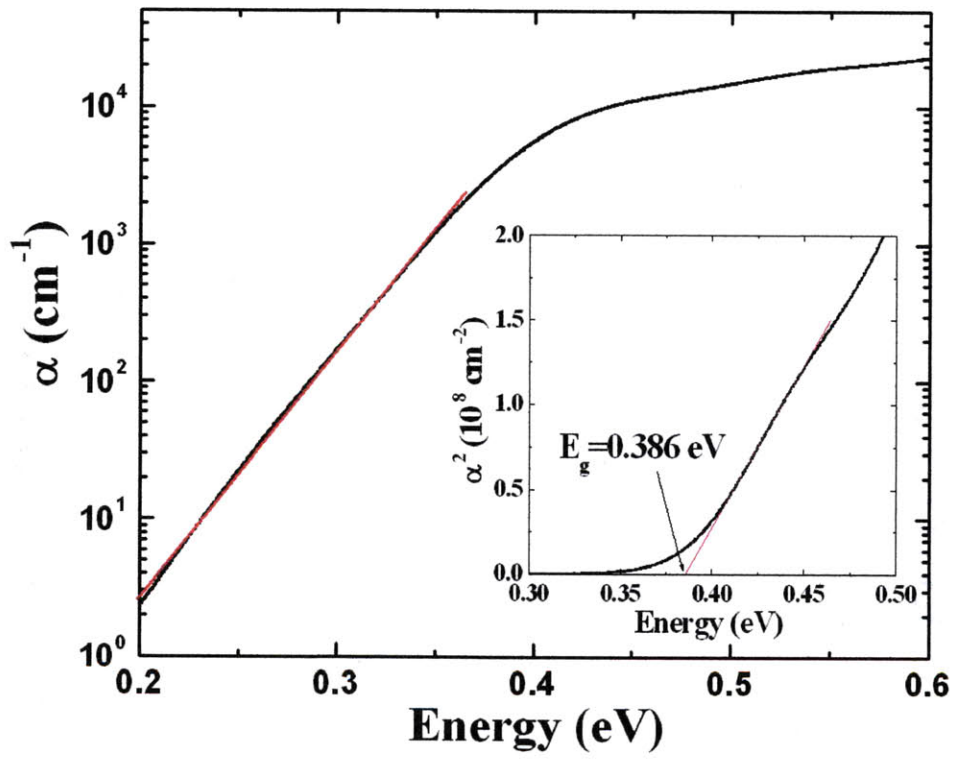

Figure 2.13 Absorption coefficient α of PbTe film as a function of photon energy. The inset shows α^2 plotted against photon energy for determination of optical band gap energy E_g.

The energy E_e is a measure of structural disorder in the material, and the typical values of E_e in disordered semiconductors range between 0.05 eV and 0.08 eV[46]. E_e is fitted from the curve slope in Figure 2.13 to be 0.056 eV, indicating disorder-like behavior of

the PbTe films. Given the nanocrystalline nature of the films, we infer that structural defects in the grain boundaries account for the Urbach band tail.

It is worth pointing out that the fitted optical band gap energy in our nanocrystalline PbTe films is much larger than the bulk value of 0.31 eV due to quantum confinement effect[31]. As is shown in Figure 2.8, typical grain size of the film is in the range of 50~100 nm, much smaller than the exciton Bohr radius of 152 nm in PbTe. Therefore, the PbTe nano-crystallites in our films can lead to strong three dimensional quantum confinement effect, which may account for the optical band gap energy increase[47]. The quantum confinement effect in polycrystalline PbTe films has also been observed by Lawson et al[48], who reported increasing blue shift of photoconductivity onset as average grain size of PbTe films decreases.

2.5. Summary

Identifying and developing proper photoactive material for the range of our interest (1~5 μm) are the key problems we need to solve at the very beginning. After investigating possible photodetector material candidates, we choose PbTe due to its mid-IR cut-off wavelength, unusual positive temperature coefficient (dE_g/dT) of the direct gap energy, and ease of material deposition and processing. In this chapter, we present a systematic study on the structural, electrical, and optical properties of thermally evaporated PbTe films. As-deposited films are stoichiometric, single FCC phase polycrystals and generally exhibit (200) texture on different substrates including amorphous glasses. The films feature grain size in the range of 50~100 nm and surface roughness of 14~16 nm. We

experimentally verify thermally activated behavior of p-type DC electrical conductivity in the films at temperatures higher than 200 K, and such temperature dependence is explained by the grain boundary channel conduction model. At reduced temperature the electrical conductivity exhibits weaker temperature dependence possibly due to hopping or tunneling transport. Refractive index and extinction coefficient of the films are measured at infrared wavelengths, and the optical band gap energy is determined to be 0.386 eV using a direct transition model, larger than the bulk value reported in single-crystalline PbTe. Such a band gap increase is pertinent to the nanocrystalline nature of the films and is a consequence of the ensuing quantum confinement effect. We also observe sub-band gap absorption due to an Urbach band tail, indicating the presence of defect states possibly arising from disordered regions in grain boundaries.

Chapter 3. Photoconductivity in polycrystalline PbTe films[49-52]

Photoconductivity is an optical and electrical phenomenon in which a material becomes more electrically conductive due to the absorption of electro-magnetic radiation such as visible light, ultraviolet light, infrared light, or gamma radiation. In our case, we choose polycrystalline PbTe film as IR light absorber due to its narrow direct band gap and thus large absorption coefficient. Since we propose to use thin photoactive layer to enhance signal-to-noise ratio besides cooling, three critical questions will be addressed in this chapter. (1) When film thickness is decreased, will it have any kind of influence on material properties? (2) Does the thermally evaporated polycrystalline PbTe film really show photo-response in mid-IR range? (3) Can we use thin PbTe film to enhance signal-to-noise ratio? Varying the film thickness, we perform a systematic study on polycrystalline PbTe film properties including microstructure, electrical properties, optical properties, and photoconductivity. Study and discussion on the photoconductivity mechanism in polycrystalline PbTe films will be presented afterwards in order to make further improvement with PbTe photoconductor's performance in the future.

3.1. Thickness dependence of polycrystalline PbTe film properties

PbTe films with five different thicknesses ranging from 100 nm to 1000 nm are prepared using single-source thermal evaporation from stoichiometric PbTe bulks as described in chapter 2. All films are deposited under the same conditions by carefully repeating the same procedure except the stopping time for different thicknesses. Optically polished CaF_2 discs and oxide coated Si wafers (6" Si wafers with 3 μm oxide) are used as starting substrates. The thermal evaporation runs are carried out at a base pressure lower than 5 ×

10^{-7} Torr. The substrates are held on a rotating substrate holder kept at room temperature throughout the depositions (8 rpm). Film deposition rate is monitored in real-time through a quartz crystal sensor and is maintained at 8~10 Å/s. The thermal evaporation technique allows deposition of films with high uniformity across an entire large-area substrate, with improved throughput and much lower cost compared to MBE. Thickness of the films is measured using a KLA Tencor P-16 surface profilometer, and we confirm excellent thickness uniformity across an entire substrate with thickness variations < 3%. In order to maintain the same deposition condition and get rid of possible contamination due to the used boat for thermal evaporation, we use brand new tantalum (Ta) boat for each deposition.

3.1.1. Microstructure evolution

Film phase composition and structure are evaluated using XRD. Grain size and surface roughness of the films are measured using AFM. Cross-sectional images are taken using a JEOL 200CX General Purpose TEM.

XRD spectra in Figure 3.1 (a) confirm PbTe films of all the thickness are polycrystalline and contain a single face-centered-cubic (FCC) crystalline phase with a rock salt structure. Detailed peak-by-peak analysis indicates all the films have a lattice parameter of 6.459 ± 0.001 Å, which is consistent with the value of 6.454 Å in the standard PDF card. However, the diffraction peak intensities in the measured spectra differ vastly from those quoted from the standard PDF card in Figure 3.1 (a), indicating strong (200) texture in the films deposited on an amorphous substrate. The degree of texture can be studied

quantitatively by the peak intensity ratio between (200) peak and (220) peak as shown in Figure 3.1 (b). Compared with the peak intensity ratio of randomly oriented polycrystalline PbTe, i.e. 1.45, our films show strong (200) texture and the degree of texture increases prominently with decreasing film thickness. For the 100 nm thick film, this ratio is more than two orders of magnitude higher than randomly oriented standard sample. Notably, this degree of texture is almost 50 times stronger compared to PbTe films deposited on soda-lime glass substrates in our previous study in chapter 2[20].

The evolution of texture as a function of film thickness and substrate type can be explained based on a two-step nucleation and growth model shown in Figure 3.2. Figure 3.2 (a) illustrates the kinetics of early stage nucleation and film growth which are primarily determined by interface energy between PbTe and SiO_2/Si substrate. In this stage, (200) becomes the preferred film growth direction due to the lower interface energy between (200) planes and the substrate, and thus strong (200) texture is expected. In thick films shown in Figure 3.2 (b), the growth of (200) grains creates new nucleation sites in the grain boundary regions, where nucleation of grains with random orientation occurs. As a consequence, the degree of texture decreases in thick films.

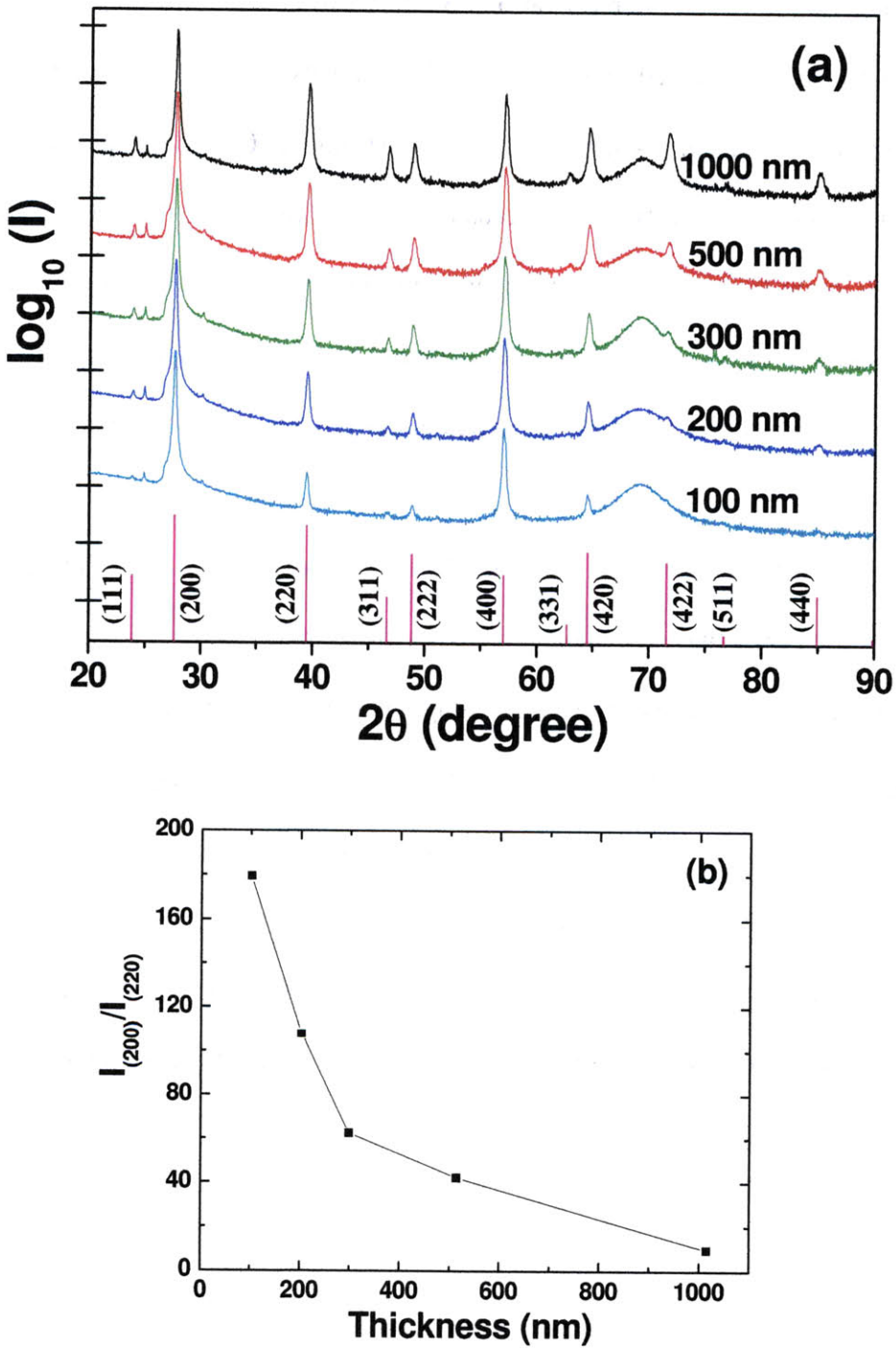

Figure 3.1 (a) XRD spectra of thermally evaporated PbTe films on oxide-coated Si substrates: the film is polycrystalline single FCC phase with strong (200) texture. Standard XRD data from Powder Diffraction File (PDF) card of # 03-065-0137 is also shown at the bottom for comparison. (b) Thickness dependence of peak intensity ratio, i.e. I(200)/I(220), showing the degree of texture increases sharply with decreasing film thickness. This ratio for standard randomly oriented PbTe sample of PDF card # 03-065-0137 is 1.45.

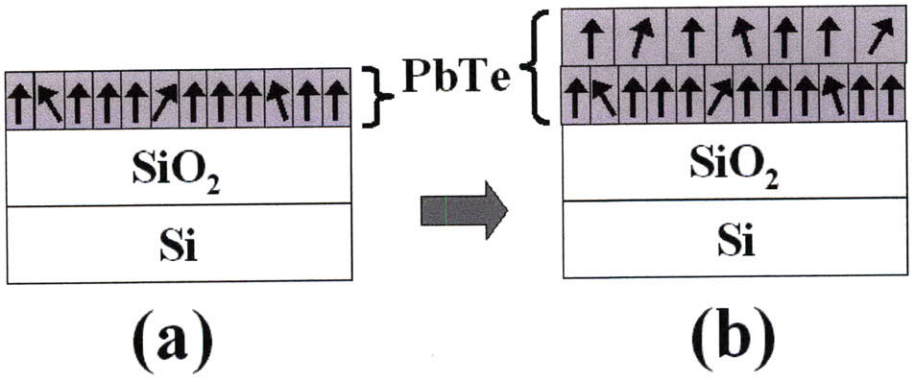

Figure 3.2 Schematic illustration of two-step nucleation and growth model for polycrystalline PbTe films on SiO_2/Si substrate. (a) Initial nucleation and growth of PbTe grains on SiO_2/Si substrate. The arrows are pointing to [200] direction in PbTe. (b) Film growth stage. New grains with more random orientations are nucleate and grow on nucleation sites created in step (a).

The two-step growth model is further verified by AFM surface morphology studies. As shown in Figures 3.3 (a)-(e), the average grain size monotonically increases with increasing film thickness from 100 nm to 1000 nm. Indicated by arrows in Figure 3.3 (d), nonequiaxial grains evolve in thick films, consistent with our hypothesis of two-stage nucleation and growth model. Figure 3.3 (f) plots the thickness dependence of average grain size and RMS surface roughness. As film thickness decreases, average grain size decreases from 50 nm for 500 nm thick film to 25 nm for 100 nm thick film, accompanied by an RMS surface roughness decrease. As we will discuss in more detail later, the fine grain structure of the films is ideal for enhanced oxygen diffusion and low-temperature sensitization process. Cross-sectional TEM image in Figure 3.4 shows the columnar structure of a 500 nm thick film. The through thickness grain boundaries are

clearly seen as indicated by the arrows, serving as diffusion "short-cuts" for oxygen incorporation.

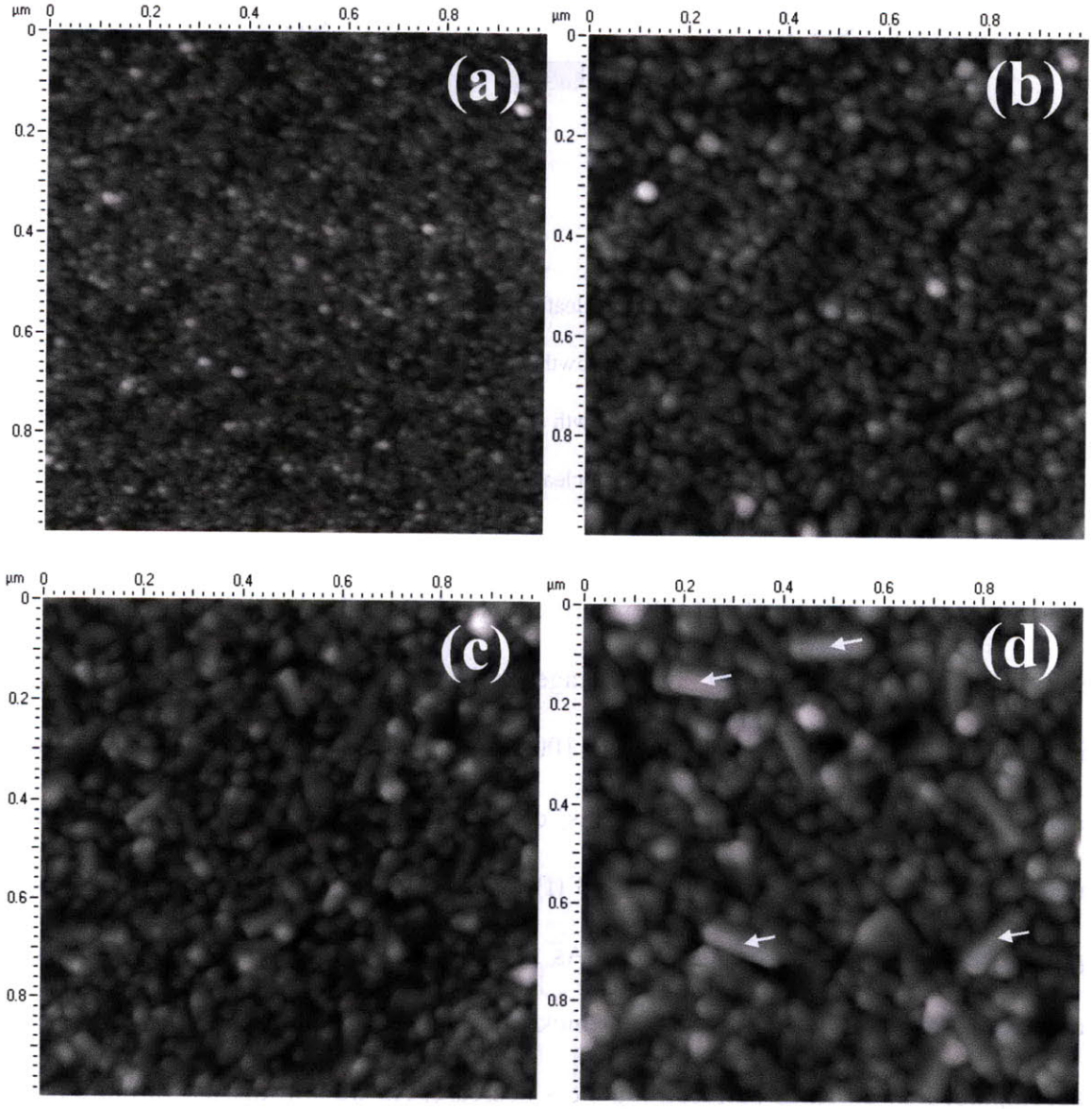

Figure 3.3 AFM surface morphology images of thermally evaporated PbTe films show the nanocrystalline structure: (a) 100 nm, (b) 200 nm, (c) 300 nm, (d) 500 nm, and (e) 1000 nm. Arrows in (d) indicate randomly oriented grains. (f) Thickness dependence of surface roughness and average grain size. Both surface roughness and average grain size decrease rapidly with decreasing film thickness.

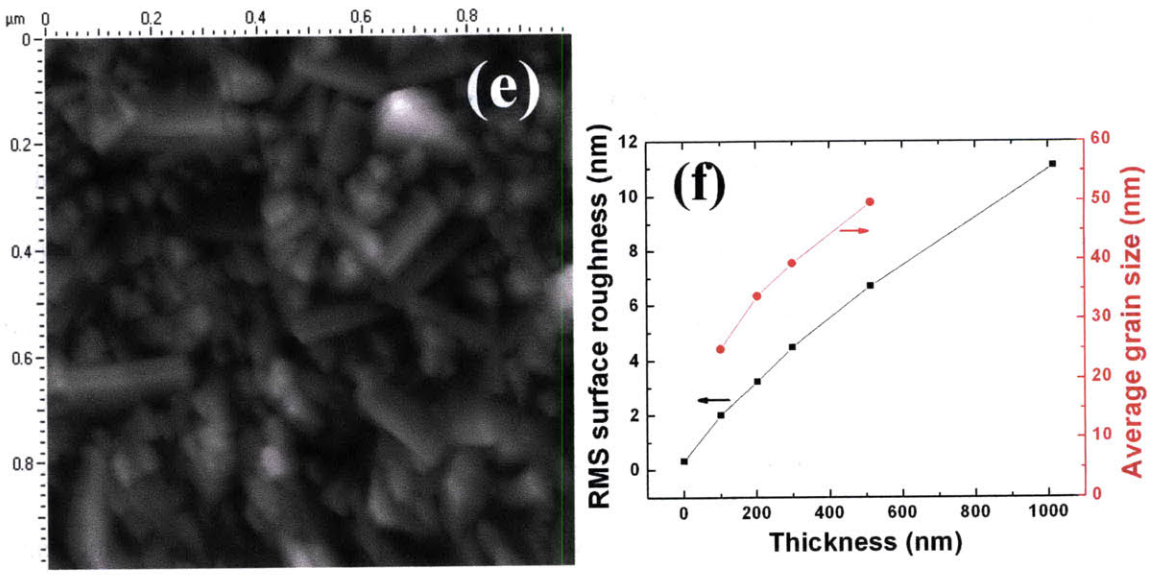

Figure 3.3 (Continued) AFM surface morphology images of thermally evaporated PbTe films show the nanocrystalline structure: (a) 100 nm, (b) 200 nm, (c) 300 nm, (d) 500 nm, and (e) 1000 nm. Arrows in (d) indicate randomly oriented grains. (f) Thickness dependence of surface roughness and average grain size. Both surface roughness and average grain size decrease rapidly with decreasing film thickness.

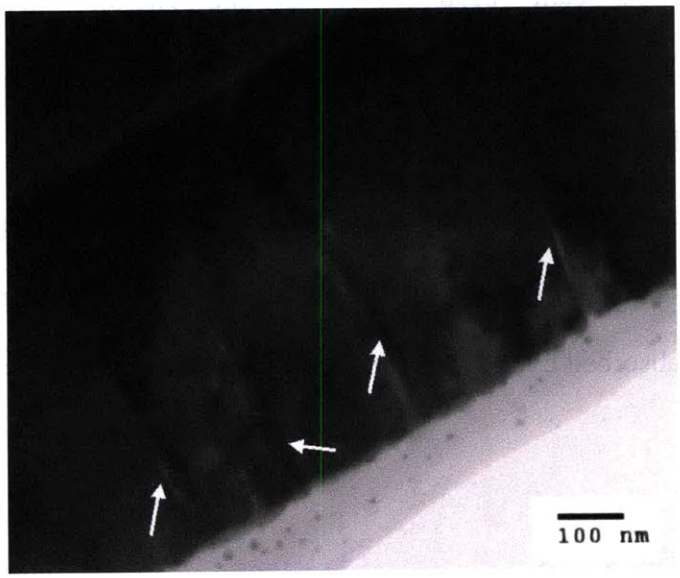

Figure 3.4 Cross-sectional TEM image shows the columnar structure of a 500 nm thick film. The through thickness grain boundaries are indicated by the white arrows.

3.1.2. Quantum efficiency

One key parameter determining the photoconductive signal is the quantum efficiency (QE). Quantum efficiency in this work is defined as the ratio of the number of photon generated excess electron-hole pairs over the number of incident photons. Due to the fact that PbTe is direct band gap semiconductor, we have made the assumption that all absorbed photons contribute to generating electron-hole pairs. Thus quantum efficiency equals to the absorbance value and could be measured by optical experiments. Due to strong interference effect in PbTe films observed in Figure 2.11, both transmittance and reflectance values need to be measured in order to calculate quantum efficiency.

PbTe films evaporated on CaF_2 are used for optical property measurements given the IR transparency of CaF_2. Transmittance and reflectance spectra are measured using a Cary 5E UV-Vis-NIR dual-beam spectrophotometer and Thermo Nicolet 6700 Fourier Transform Infrared Spectrometer (FTIR). Figures 3.5 (a) and 3.5 (b) show the measured results for PbTe films of thicknesses from 100 nm to 1000 nm. Strong interference effect can be observed in both transmittance and reflectance spectra, suggesting from only transmittance or reflectance value it is not possible to calculate or predict how much incident light gets absorbed by the films and thus the quantum efficiency.

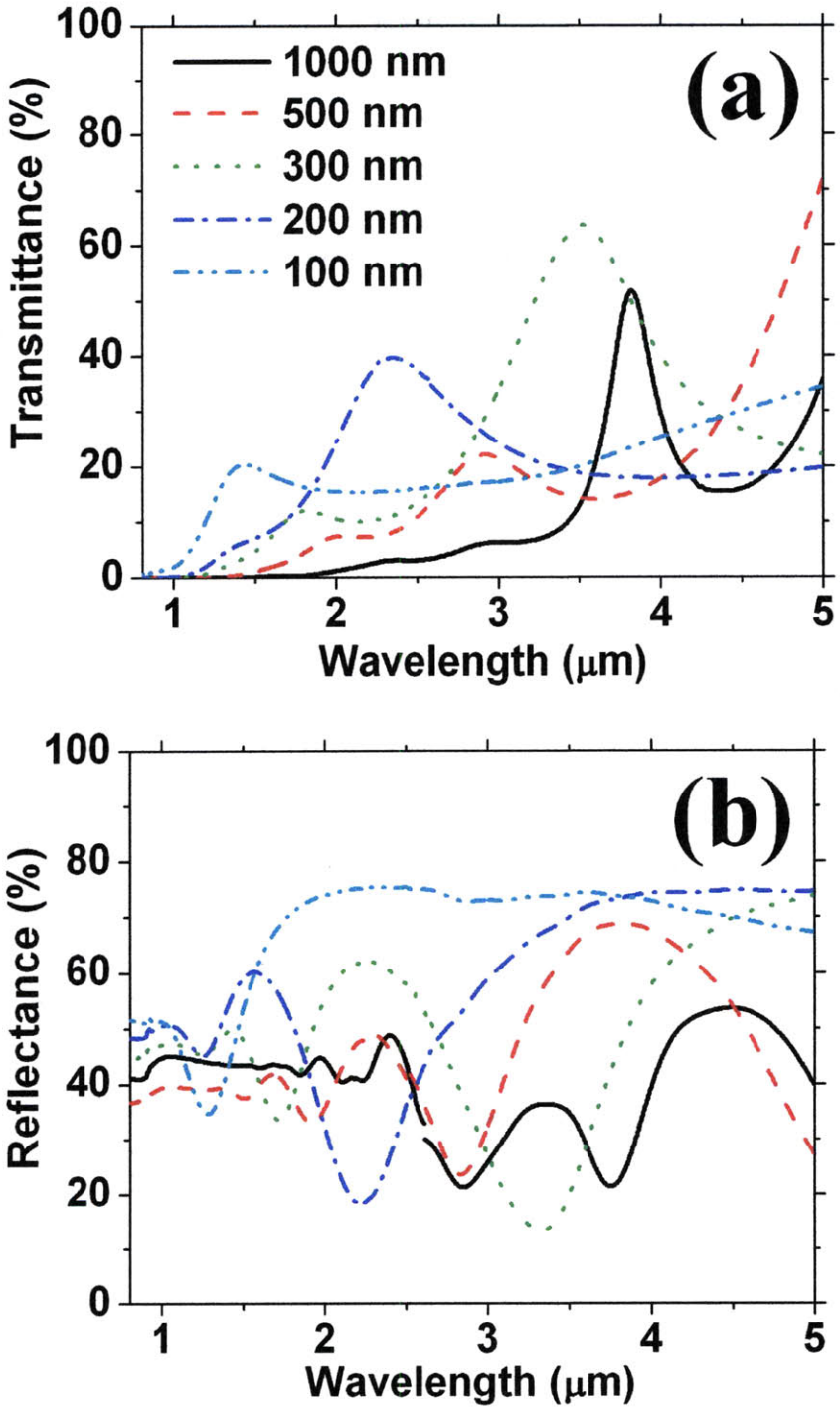

Figure 3.5 (a) Transmittance and (b) reflectance spectra for polycrystalline PbTe films of thicknesses from 100 nm to 1000 nm. Strong interference effect is observed in both results.

Based on results in Figure 3.5, quantum efficiency as a function of wavelength can be calculated by:

$$QE(\lambda) = 100\% - T(\lambda) - R(\lambda) \tag{3.1}$$

where QE(λ), T(λ), and R(λ) denote the quantum efficiency, transmittance, and reflectance respectively, and they are all functions of wavelength λ. This result is shown in Figure 3.6 for all studied thicknesses. In shorter wavelength range (λ<1.2 μm), the absorption coefficient of PbTe is high enough for the films to absorb more than half of the incident light. Light not being absorbed is mostly reflected. In longer wavelength range (λ>1.2 μm), film thickness plays an important role in determining the interference patterns and the quantum efficiency at certain wavelength.

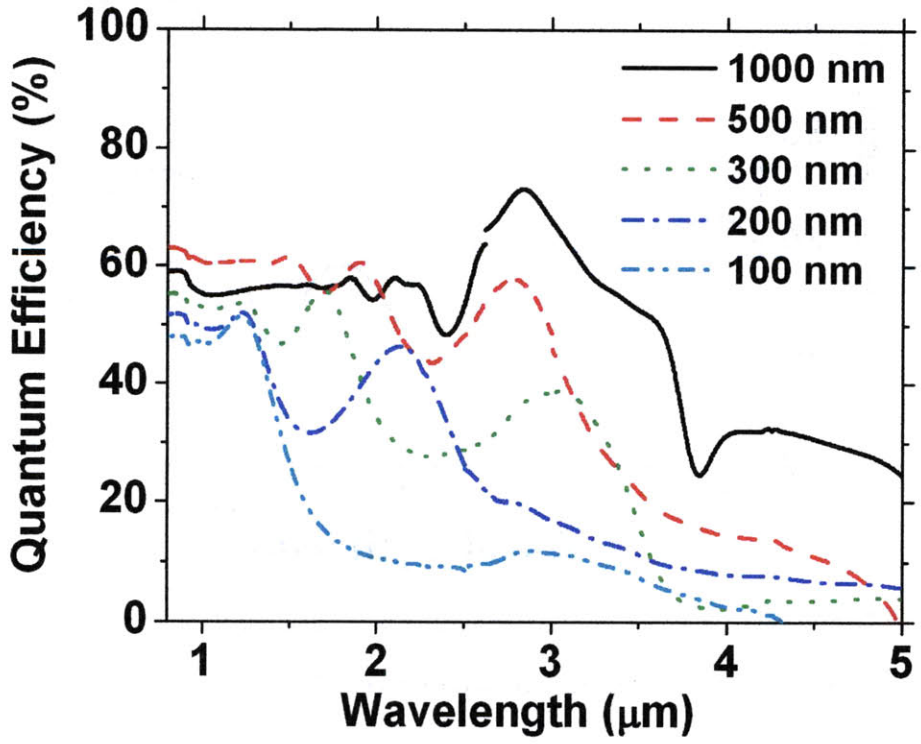

Figure 3.6 Quantum efficiency as a function of wavelength for polycrystalline PbTe films of different thicknesses (100~1000 nm). Strong interference effect is observed.

3.1.3. Carrier concentration and Hall mobility

Tin electrodes are deposited through a shadow mask by e-beam evaporation and are used as contacts for Hall experiments and electrical measurements. We observe linear I-V characteristics at temperatures from 80 K to 340 K, confirming the ohmic nature of electrical contact. Hall experiments are performed using a van der Pauw technique at a magnetic field of 4000 G.

Thinner PbTe film features finer microstructure as concluded from the results in Figure 3.1 and Figure 3.3. Thus one may expect distinct electrical properties in thinner film compared to thicker film, such as resistivity, carrier concentration, and Hall mobility. However, in this part we will show that our polycrystalline PbTe films of all thicknesses have similar electrical properties and no thickness dependence of these material properties has been observed.

From Hall measurements, we confirm that all films of different thicknesses are p-type after exposure to air at room temperature. Data measured over a period of four months indicate that the carrier concentration remains stable at an average value of $(1.2 \pm 0.3) \times 10^{-17}$ cm^{-3}, and Hall mobility reaches an average value of (81 ± 13) $cm^2V^{-1}s^{-1}$. We also study the stability of films exposed to oxygen in an ambient atmosphere. As is shown in Figure 3.7, no thickness or time dependence of either carrier concentration or Hall mobility has been observed for our films. Further, we note that the carrier concentration of $(1.2 \pm 0.3) \times 10^{-17}$ cm^{-3} is among the lowest values reported in PbTe films at room

temperature (the calculated intrinsic value is 0.8×10^{-16} cm^{-3}). As we will show in the next section, such low carrier concentration contributes to improved infrared photoconductivity of our films.

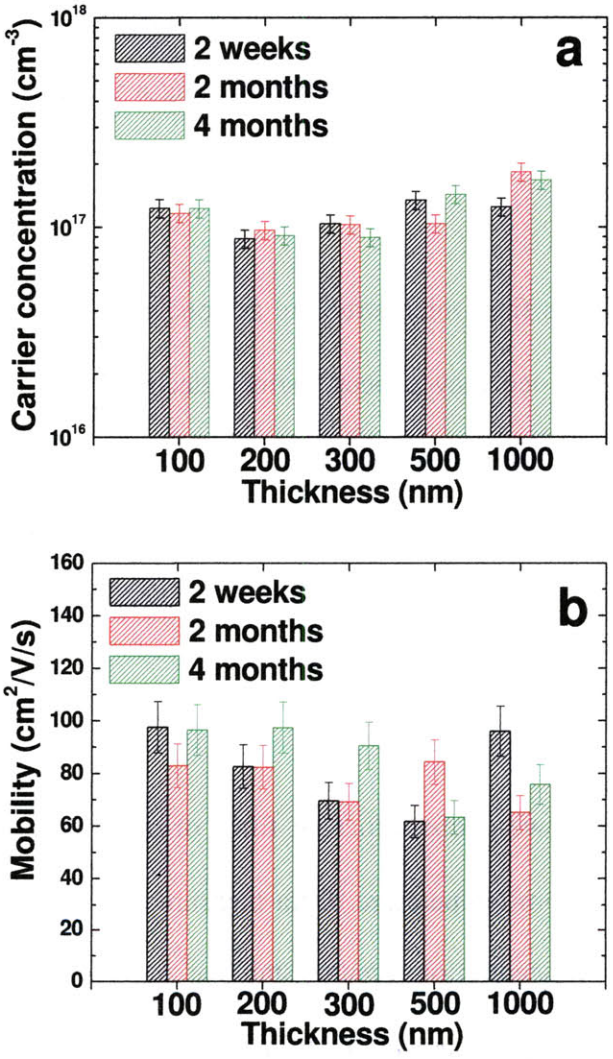

Figure 3.7 (a) Carrier concentration and (b) Hall mobility vs. PbTe film thickness taken at room temperature at three different time intervals after deposition using a van der Pauw technique. No thickness or time dependence of either carrier concentration or Hall mobility has been observed. The carrier concentration has an average value of 1.2×10^{17} cm^{-3} and a standard deviation of 0.3×10^{17} cm^{-3}. Hall mobility has an average value of 81 $cm^2V^{-1}s^{-1}$ and a standard deviation of 13 $cm^2V^{-1}s^{-1}$. $(1.2 \pm 0.3) \times 10^{17}$ cm^{-3} is among the lowest reported carrier concentrations at room temperature for PbTe.

Hall experiment is also performed at different temperatures from 213 K to 300 K in order to separate two components' contribution in film resistivity, i.e. carrier concentration and mobility. The former could help locate the Fermi level in the band structure, and the latter could facilitate understanding the scattering process in electrical conduction. All the films in the studied temperature range are p-type, and films of all thicknesses yield similar results and key parameters are summarized in Table 3.1. Figure 3.8 shows typical temperature dependence of carrier concentration and Hall mobility of a 200 nm thick film. Figure 3.8 (a) suggests thermally activated process exists in the polycrystalline PbTe films and the activation energy is fitted to be 0.111 eV. The activation energy fitted for films of other thicknesses are listed in Table 3.1, and all values are around 0.11 eV.

For p-type semiconductors, hole concentration p can be calculated by:

$$p = N_v \exp\left(-\frac{E_F - E_v}{kT}\right) \tag{3.2}$$

where N_v is the effective density of states of the valence band, E_F is the Fermi level, E_v is the valence band edge, k is the Boltzmann constant, and T is the absolute temperature. This indicates Fermi level is 0.11 eV above the valence band edge. Compared to the band gap energy of PbTe at room temperature, i.e. 0.31 eV, this demonstrates the Fermi level is near mid-gap and therefore results in very low carrier concentration in our polycrystalline PbTe films.

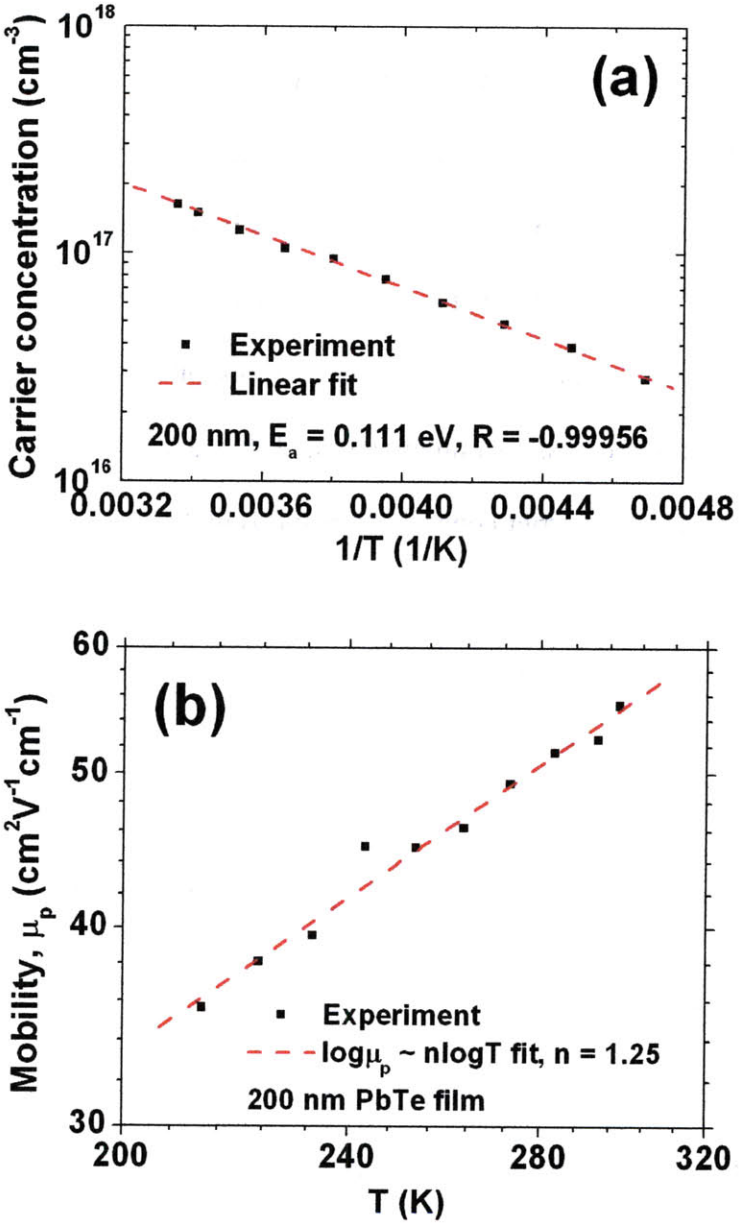

Figure 3.8 (a) Carrier concentration and (b) Hall mobility as a function of temperature. Temperature dependence of carrier concentration suggests thermally activated process in the PbTe film and Fermi level is 0.111 eV above the valence band. Temperature dependence of mobility shows ionized defect scattering dominates the electrical conduction in the PbTe film.

Mobility is usually a strong function of material impurities and temperature. An approximation of the mobility function can be written as a combination of influences from lattice vibrations (phonons) and from impurities:

$$\frac{1}{\mu} = \frac{1}{\mu_{\text{lattice}}} + \frac{1}{\mu_{\text{impurities}}} \tag{3.3}$$

where $\mu_{\text{lattice}} \propto T^{-\frac{3}{2}}$ and $\mu_{\text{impurities}} \propto T^{\frac{3}{2}}$. Fitting temperature dependence of mobility gives a power law with a factor of 1.25 as shown in Figure 3.8 (b) for 200 nm thick film. The fitted power factors for other thicknesses are summarized in Table 3.1. The result indicates that ionized defect scattering dominates the electrical conduction in PbTe films, which could be expected given the polycrystalline nature of the films. Following the discussion on p-type inversion channel conduction in part 2.3, and the microstructure study of the polycrystalline PbTe films in part 3.1.1, we speculate the defects mainly exist in the grain boundary regions. Later we will show further evidence of oxygen's existence and diffusion in the PbTe films, and its influence on the electrical properties. Thus the origin of the defects could also be identified.

Table 3.1 Activation energy and power factor fitted from temperature dependence of carrier concentration and Hall mobility for polycrystalline PbTe films of different thicknesses.

Film thickness (nm)	Activation energy (E_F-E_v) (eV)	Power factor
100	0.108	1.50
200	0.111	1.25
300	0.112	0.85
500	0.106	0.65
1000	0.109	1.86

3.1.4. Photoconductivity

IR light from a blackbody is monochromatized through a sodium chloride prism and modulated at 10.3 Hz for the photoconductivity measurement. An SP2402 thermoelectric cooler (TEC) from Marlow Industries Inc. is used for cooling samples down to -60 °C. The incident IR light power density on the PbTe photoconductor is calibrated using a thermopile as reference. Figure 3.9 shows the electric circuit used in the photoconductivity measurement. PbTe photoconductor is biased under fixed current by a Keithley 220 current source, and the photovoltage caused by the IR light illumination is recorded by a lock-in amplifier. Photon incident flux and spectral shape are obtained from the thermopile reference detector with known area (A_{ref}) and responsivity ($\Re_{ref}$). With known PbTe photoconductor's area (A_d), and measured photovoltage signals from both reference detector (V_{ref}) and PbTe photoconductor (V_d), sample's responsivity can be calculated by:

$$\Re_d = \frac{V_d}{\frac{V_{ref} / \Re_{ref}}{A_{ref}} \cdot A_d} = \Re_{ref} \cdot \frac{V_d}{V_{ref}} \cdot \frac{A_{ref}}{A_d} \tag{3.4}$$

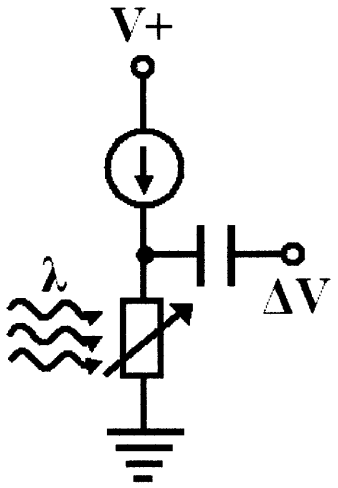

Figure 3.9 Electric circuit used to measure photo-response from PbTe photoconductors. Samples are biased under fixed current and the photovoltage caused by the IR light illumination is recorded by a lock-in amplifier.

We measure excellent photoconductive signal in the wavelength range of 0.8~5 μm in the polycrystalline PbTe films of all thicknesses, as shown in Figure 3.10. Experiment is performed under 0.1 mA bias current and at two temperatures (-60 °C and -40 °C). For all thicknesses, responsivity at -60 °C is about 4~6 times higher than at -40 °C showing the advantage of cooling. The influence of temperature on responsivity will be discussed in detail later. Responsivity is also found out to be linearly dependent on bias current when we perform the measurement with different bias current. And the result is plotted in Figure 3.11.

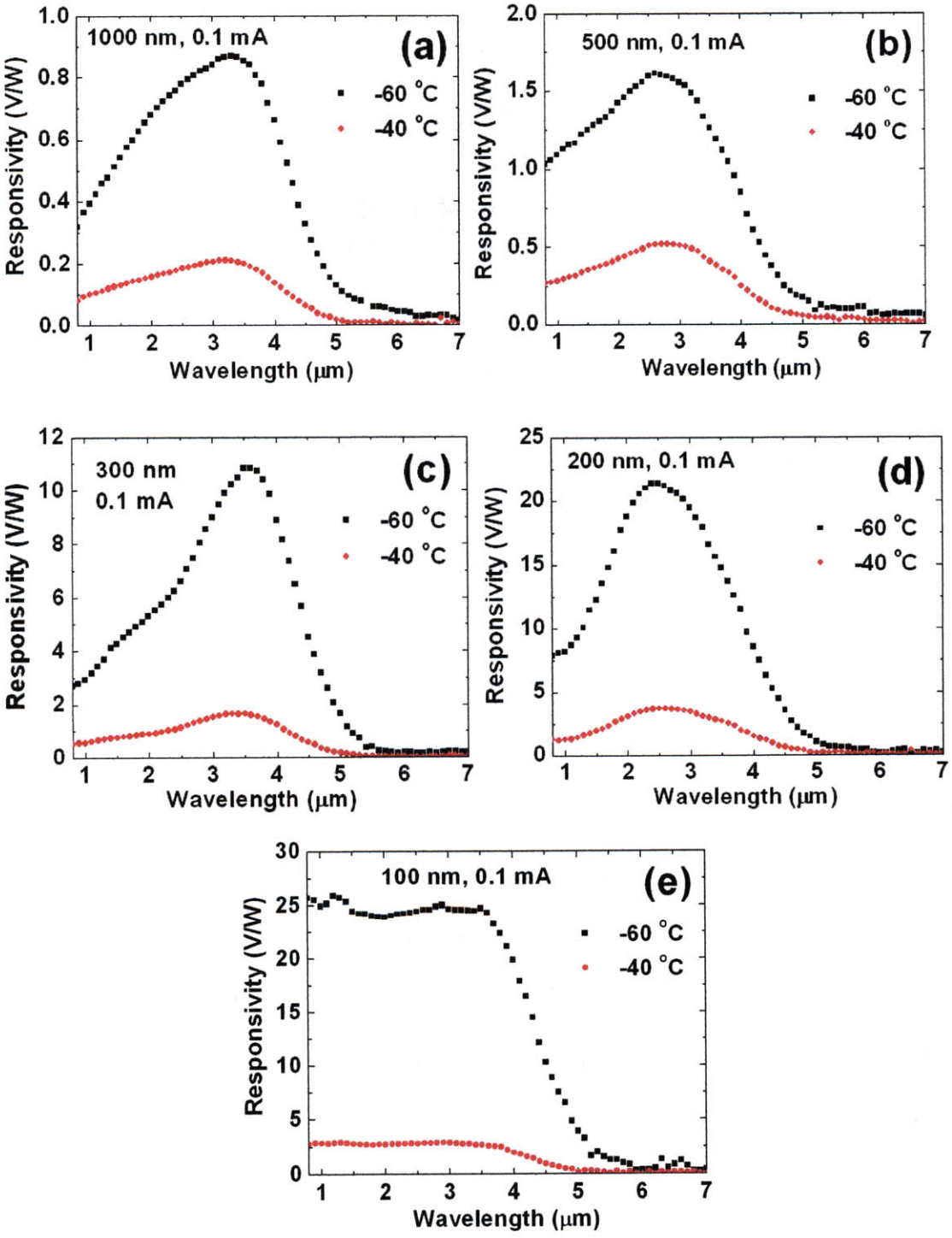

Figure 3.10 Responsivity spectra of polycrystalline PbTe films of different thicknesses: (a) 1000 nm, (b) 500 nm, (c) 300 nm, (d) 200 nm, (e) 100 nm. The experiment is performed at fixed bias current of 0.1 mA and at two temperatures, i.e. -60 °C and -40 °C.

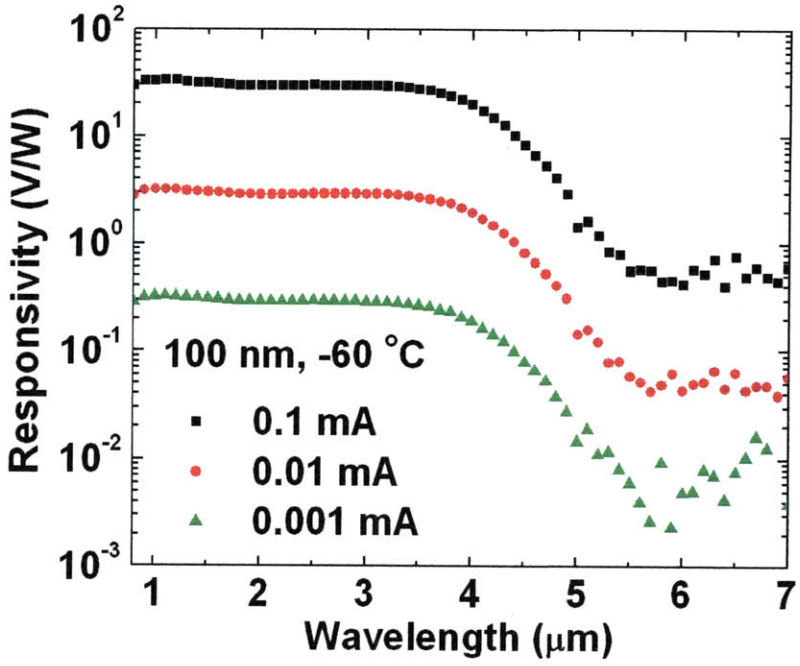

Figure 3.11 Responsivity spectra taken at different bias current shows linear dependence of responsivity on bias current. The measurement is performed on a 100 nm thick polycrystalline PbTe film at -60 °C.

One prominent character observed from Figure 3.10 is that under the same bias current, responsivity is strongly dependent on film's thickness. This trend can be seen more clearly in Figure 3.12, which plots responsivity spectra for films of different thicknesses (100~1000 nm) taken at the same bias current (0.1 mA) and temperature (-60 °C). Thin film interference effect determines the peak responsivity location for films of different thicknesses, which agrees with quantum efficiency spectra of these films shown in Figure 3.6. Even though quantum efficiency of 100 nm thick film is 5~6 times lower than that of 1000 nm thick film, responsivity obtained in 100 nm thick film is more than 20 times higher than in 1000 nm thick film. In order to understand this "contradiction", more detailed study on responsivity's dependence on quantum efficiency, material property, photoconductor's geometry, and external bias will be discussed.

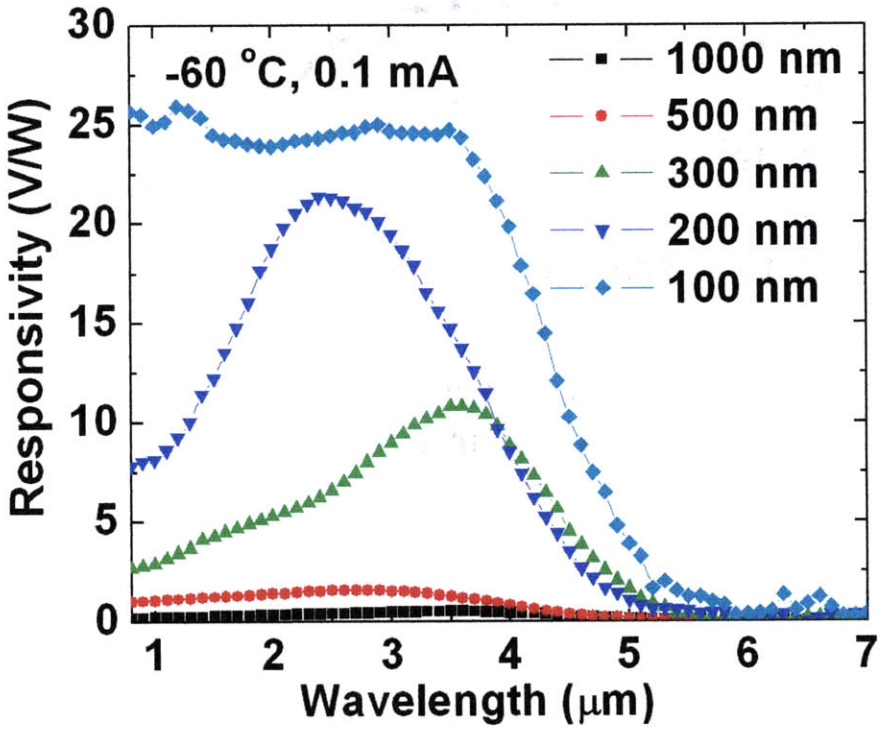

Figure 3.12 Responsivity spectra of polycrystalline PbTe films of different thickness under 0.1 mA bias current and at -60 °C cooled by a thermoelectric cooler (TEC). All films show excellent photoconductive signal in the wavelength range of 0.8~5 μm, and the peak responsivity location is determined by interference effect. More than 20 times higher photo-signal for 100 nm thick film is observed compared with 1000 nm thick film.

Here we refer to two theories that underlie the photoconductive mechanism in lead chalcogenide films: number modulation theory[53-55] and barrier modulation theory[56]. Number modulation theory attributes photoconductivity in lead chalcogenide to the increase of carrier concentration under illumination, while the latter suggests that increase of effective mobility by lowering of intercrystalline potential barriers accounts for photoconductivity in lead chalcogenide. According to the discussions by Moss[31] and

Yasuoka[57-59], the number modulation model is consistent with the majority of experimental observations in lead chalcogenide films. Since we measure no mobility change in PbTe films in dark and under illumination, we employ the number modulation model to quantitatively analyze our data. Based on this theory, responsivity ($\Re$) can be expressed explicitly as:

$$\Re = \frac{I\tau(1+b)\lambda \mathrm{QE}}{hcew^2d^2p^2\mu_p} \tag{3.5}$$

where I is the bias current, QE denotes quantum efficiency, τ is the lifetime of photo-generated carriers, b gives the ratio of electron mobility against hole mobility, λ is the wavelength of light, h represents the Plank constant, c is the speed of light in vacuum, e is the elementary charge, w is the width of photoconductor, d is the thickness of photoconductor, and p and μ_p are hole concentration and mobility, respectively.

The measured strong thickness dependence of responsivity in our films shown in Figure 3.12 is consistent with Equation 3.5. Under the same bias current, there are three types of contributions of film thickness to the responsivity: quantum efficiency, geometric factor of photoconductor's resistance, and carrier concentration change upon illumination. The first contribution in quantum efficiency is the least explicit part due to the very strong interference effect for thin films, while both of the last two contributions are linearly dependent on the inverse of thickness. As confirmed from quantum efficiency spectrum study in Figure 3.6, the last two contributions are dominant over the first one in our case, and thus the responsivity increases with decreasing film thickness.

If we plot the responsivity as a function of QE/d^2, where the quantum efficiency (QE) can be calculated using experimentally measured optical absorbance, a linear relationship would be expected according to Equation 3.5, which is confirmed in Figure 3.13. Equation 3.5 also shows the strong dependence of responsivity on the carrier concentration and mobility. According to results in Figure 3.8 and Table 3.1, carrier concentration has an exponential dependence on temperature and mobility obeys a power law. As temperature decreases, both carrier concentration and mobility decrease, resulting in enhanced responsivity by cooling. This also explains why photoconductivity is mostly obtained in films with very low carrier concentration and high resistivity.

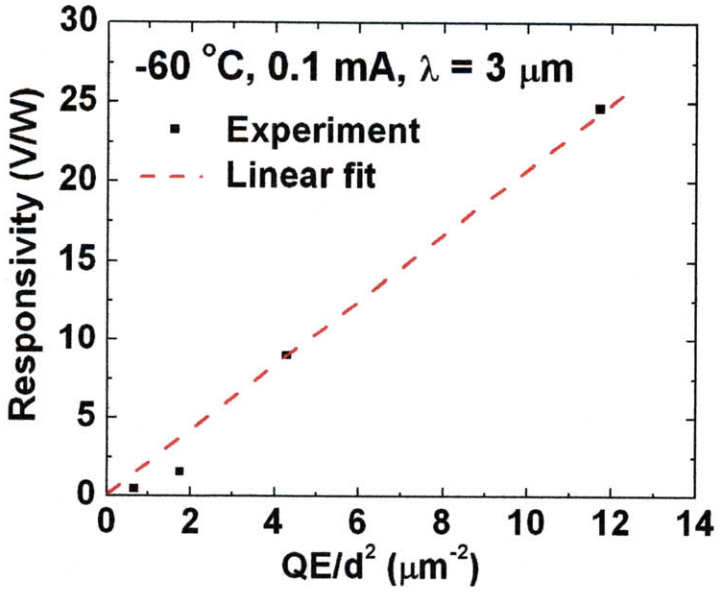

Figure 3.13 Plot of responsivity vs. QE/d^2 shows the thickness dependence of responsivity at 3 μm wavelength. A linear relationship is observed, consistent with Equation 3.5. The red dashed line is the linear fit to the experimental data.

Noise analysis shows that 1/f noise dominates at low modulation frequencies (< 100 Hz) for all the films (will be discussed in detail later). As observed from experiment, 1/f noise level is independent on film thickness only when the electric field rather than the bias current is held as constant when comparing films of different thicknesses. Therefore, responsivity normalized to the same electric field of 100 V/cm and hence identical 1/f noise level is plotted in Figure 3.14 to compare the thickness-dependent infrared detection signal-to-noise ratio (SNR) at 3 μm wavelength. The high SNR achieved in thin films highlights the competitive advantage of using thin PbTe films for infrared detection. The low quantum efficiency of thin films can be further overcome by incorporating a photonic-crystal resonant cavity structure which will be discussed in chapter 4.

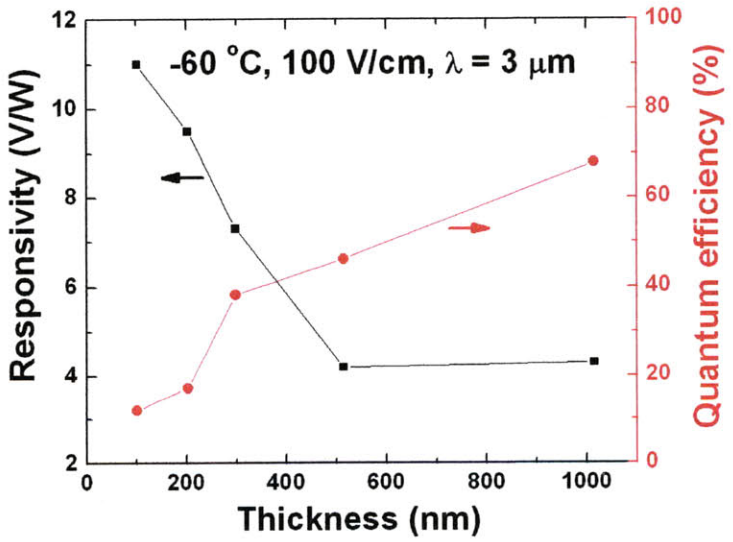

Figure 3.14 Thickness dependence of responsivity and quantum efficiency at 3 μm wavelength. The responsivity data is taken under an electric field of 100 V/cm. Thinner films show much higher photo-signals than thicker films despite their lower quantum efficiency. The quantum efficiency for thinner films can be enhanced by incorporating a cavity structure.

3.1.5. Noise analysis and detectivity of polycrystalline PbTe photoconductors

Besides quantum efficiency and responsivity, for any kind of IR photodetectors, signal-to-noise ratio (SNR) is one of the most important characteristics. Detectivity (D^* or D-star) is a commonly used parameter to compare performance of different IR photodetectors. It is the signal-to-noise ratio at a particular electrical frequency and in a 1 Hz bandwidth when 1 Watt of radiant power is incident on a 1 cm^2 active area detector. The higher the D* value, the better the detector. Mathematically, D* is defined as follows:

$$D^* = \frac{\Re\sqrt{A_d \Delta f}}{v_n} \tag{3.6}$$

where $\Re$ is the responsivity of the photodetector, A_d is the area of the photodetector, Δf is the effective noise bandwidth, and v_n is the noise voltage of the photodetector.

In photoconductors, major noise sources include generation-recombination noise (G-R noise), 1/f noise, and Johnson noise[60]. G-R noise is the most complicated one since it has three contributions: background irradiance on the photoconductor, signal irradiance on the photoconductor, and thermal generation. G-R noise voltage (v_{nGR}) can be calculated by:

$$v_{nGR} = 2G \cdot e \cdot R_d \cdot \sqrt{\left(QE \cdot E_{qb} \cdot A_d + QE \cdot E_{qs} \cdot A_d + g_{th}\right) \cdot \Delta f} \tag{3.7}$$

$$G = \frac{(1+b) \cdot \mu_p \cdot E \cdot \tau}{l} \tag{3.8}$$

$$R_d = \frac{1}{p \cdot e \cdot \mu_p} \cdot \frac{l}{w \cdot d} \tag{3.9}$$

$$A_d = l \cdot w \tag{3.10}$$

$$g_{th} = \frac{n \cdot w \cdot d \cdot l}{(1+b)^2 \cdot \tau} \cdot \frac{1}{1+(2\pi f \cdot \tau)^2} \tag{3.11}$$

where G is the photoconductive gain, E is the electric field across the photoconductor, l and A_d are the length and area of the photoconductor, R_d is the resistance of the photoconductor, E_{qb} and E_{qs} are the background and signal irradiance on the photoconductor (in the unit of #/cm^2/s), g_{th} is the thermal-generation rate of carriers in the photoconductor (in the unit of #/s), n is the electron concentration in p-type photoconductors, f is the optical modulation frequency in photoconductivity measurement, and all other parameters are defined in the same way as in Equation 3.5.

1/f noise voltage can be calculated by:

$$v_{n1/f} = R_d \cdot I \cdot \sqrt{\frac{B_{1/f} \cdot \Delta f}{f}} \tag{3.12}$$

where I is the bias current in the photoconductivity measurement, $B_{1/f}$ is a constant related with the equipment.

Johnson noise voltage can be calculated by:

$$v_{nJ} = \sqrt{4kT \cdot R_d \cdot \Delta f} \tag{3.13}$$

The total noise voltage should be calculated by:

$$v_n = \sqrt{v_{nGR}^2 + v_{n1/f}^2 + v_{nJ}^2} \tag{3.14}$$

According to Equation 3.5, with known PbTe photoconductors' geometry and experimental conditions, and measured responsivity, carrier concentration, and mobility, we calculate the carrier lifetime in our polycrystalline PbTe photoconductors is on the order of ns (-40~-60 °C). Based on Equations 3.7~3.13, all major noise voltages except 1/f noise can be calculated and they are summarized in Table 3.2. The directly measured noise voltage is also listed in Table 3.2. We observe linear dependence of measured noise voltage on bias current and it decreases with increasing optical modulation frequency. According to Equation 3.12 and comparing the total measured noise voltage with G-R noise and Johnson noise, we conclude that 1/f noise dominates at low modulation frequencies (< 100 Hz) in our polycrystalline PbTe photoconductors.

Table 3.2 Calculated/measured noise voltages in polycrystalline PbTe photoconductors

Noise sources	Calculated/Measured data (V)
G-R noise	
Background irradiance on the detector	10^{-14} ~ 10^{-10}
Signal irradiance on the detector	10^{-13} ~ 10^{-9}
Thermal G-R noise	10^{-13} ~ 10^{-8}
Johnson noise	10^{-8} ~ 10^{-7}
1/f noise	
Total measured noise	10^{-7} ~ 10^{-6}

Since 1/f noise is proportional to the inverse of square root of optical modulation frequency, for commercial infrared detector optics, high electrical modulation frequencies (1~20 kHz) are implemented to circumvent 1/f noise[60,61]. Under such a circumstance, Johnson noise will be the dominant noise, and can be calculated by:

$$D^* = \frac{I(1+b)\tau\lambda \mathrm{QE}}{hcw\sqrt{4kTed^3p^3\mu_p}} \tag{3.15}$$

We extrapolate a Johnson-noise-limited detectivity of 1.4×10^{10} cmHz$^{1/2}$/W at -60 °C at 3.6 μm using the measured parameters of our polycrystalline PbTe film[62]. This detectivity figure compares favorably to current commercial mid-IR HgCdTe detectors using single-crystalline materials[61].

3.2. Photoconductivity mechanism in polycrystalline PbTe films

So far, we have demonstrated excellent photoconductivity in polycrystalline PbTe films, and usage of thin IR absorbing layer can greatly enhance the signal-to-noise ratio. 100 nm thick PbTe layer shows record-low carrier concentration and remains stable within a period of four month or even longer. However, no explanation for the observed photoconductivity or such low carrier concentration has been provided yet, which is critical and necessary not only for scientific research interest, but also for device performance improvement in the future. Thus the scope of this part is to study and discuss the photoconductivity mechanism in our polycrystalline PbTe films.

3.2.1. Oxygen sensitization in lead chalcogenides

Lead chalcogenides including PbS, PbSe, and PbTe are commonly used materials for IR detection due of their superior chemical and mechanical stability. Highly sensitive mid-IR lead chalcogenide photodetectors have been demonstrated through annealing as-deposited films at high temperatures in an oxidizing atmosphere[21,22]. It has been well established that the oxidation annealing incorporates p-type oxygen dopant in the film

and sensitizes the infrared photo-response of lead chalcogenide[38,53-55,57-59,63-72]. Oxygen can serve as acceptor depleting the electrons in as-deposited films and also form minority carrier traps increasing the photo-generated carrier lifetime, and thus enhance the photoconductivity. Some key findings are: (1) polycrystalline lead chalcogenide films evaporated from stoichiometric bulks are usually n-type due to Te or Se deficiency. After sensitization, oxygen serves as acceptors which can deplete electrons in the conduction band; (2) oxygen-sensitized films exhibit p-type conduction, increased film resistivity and very long photo-generated carrier lifetime; (3) oxygen sensitization is a diffusion-limited process; and (4) grain boundaries assist in oxygen diffusion, as oxygen sensitization in polycrystalline films occurs over a much shorter time scale compared to their single-crystalline counterparts.

According to these observations, the oxygen sensitization in lead chalcogenides are attributed to two factors: (1) neutralization of free electrons which reduces dark current; and (2) carrier lifetime increase, which is explained by the spatial separation of photo-generated electrons and holes due to minority carrier traps $(PbO)^{2+}$. Despite the above progress made on lead chalcogenide materials, monolithic integration of highly sensitive photodetector arrays with Si ROIC still remains unexplored, largely due to high temperature annealing process involved (> 450 °C)[73-75].

We demonstrate significant photoconductivity in our polycrystalline PbTe films without high temperature annealing. There are two possible ways for the incorporation of oxygen into the films: (1) during the thermal evaporation process; and (2) oxygen diffusion when

the films are exposed to air. The second possibility is due to the fact that our polycrystalline PbTe films feature nanocrystalline microstructure with highly textured columnar grains as shown in part 3.1.1. The vertically aligned grain boundaries between columnar nanocrystalline grains offer abundant diffusion "short-cuts" for oxygen diffusion and sensitization at much reduced temperature. To demonstrate the existence of oxygen in the PbTe films and find out which oxygen incorporation process is dominant for the photoconductivity and low carrier concentration, we perform more detailed study on oxygen sensitization mechanism and electronic structure of oxygen sensitized PbTe films.

3.2.2. Oxygen sensitization in polycrystalline PbTe films

With the help of a capping layer of thermally evaporated $Ge_{23}Sb_7S_{70}$ film, PbTe films with two different oxygen concentrations are prepared. They are denoted as "PbTe w/ capping layer" and "PbTe w/o capping layer" as shown in Figure 3.15 and Table 3.3. For sample "PbTe w/ capping layer", Sn metal contacts are pre-deposited through a shadow mask onto the substrate (6" 3 μm SiO_2 coated Si wafers) for electrical measurement. PbTe and $Ge_{23}Sb_7S_{70}$ capping layer are then deposited by thermal evaporation in sequence without breaking the vacuum of the chamber (two separate evaporation sources are employed). Sample "PbTe w/o capping layer" is the normal PbTe film exposed to air immediately after deposition. All films are deposited under a background pressure lower than 5×10^{-7} Torr.

Secondary ion mass spectrometry (SIMS) is employed to acquire the oxygen concentration and distribution in PbTe films. Cs ion beam is used to sputter material out of the sample. The background pressure is on the order of 10^{-9} Torr, and the detection limit for oxygen is 1×10^{18} atoms/cm^3. Oxygen concentration depth profiles in two samples are shown in Figure 3.15 and the concentration values in the middle of the PbTe films are listed in Table 3.3. The result demonstrates $Ge_{23}Sb_7S_{70}$ capping layer serves as very effective oxygen diffusion barrier, since oxygen concentration in the sample "PbTe w/ capping layer" is almost two orders of magnitude lower than in "PbTe w/o capping layer". Moreover, Figure 3.15 suggests oxygen in the air indeed could diffuse into our polycrystalline PbTe films due to the nanometer-sized grains and vertically aligned through thickness grain boundaries. And this diffusion process happens very fast event at room temperature.

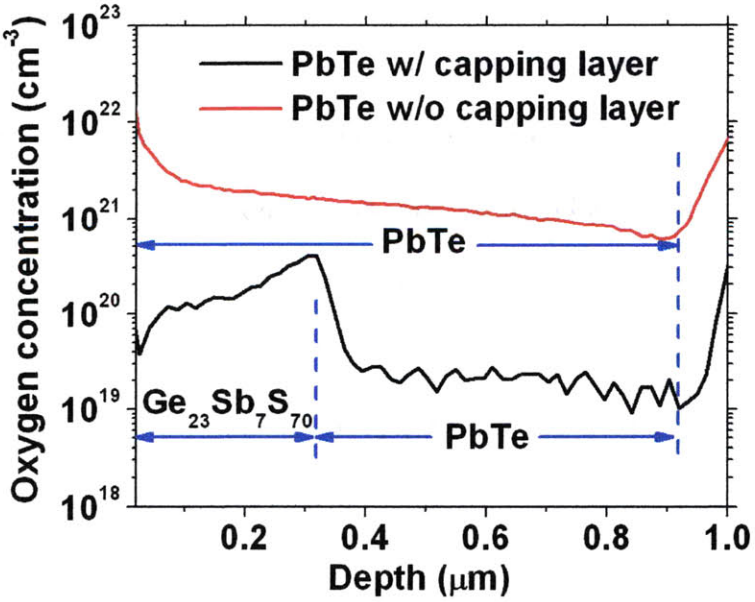

Figure 3.15 Oxygen concentration depth profiles obtained by SIMS for PbTe films with and without $Ge_{23}Sb_7S_{70}$ capping layer.

Table 3.3 Comparison of PbTe films with and without $Ge_{23}Sb_7S_{70}$ capping layer.

	PbTe w/ capping layer	PbTe w/o capping layer
Oxygen concentration (cm^{-3})	2.3×10^{19}	1.3×10^{21}
Carrier concentration at 300 K (cm^{-3})	7.36×10^{16}	12.5×10^{16}
Activation energy (eV)	0.125	0.109
Calculated N_v (cm^{-3})	9.3×10^{18}	8.5×10^{18}

X-ray photoelectron spectroscopy (XPS) is employed to reveal the chemical status of the oxygen in the PbTe films. Ar ion beam is used to get rid of the surface oxidation layer. We have identified two chemical states for both Pb and Te: one is due to normal Pb-Te bonds in PbTe, and the other is due to oxidation of Pb and Te. This conclusion is further supported by two chemical binding states observed in oxygen's XPS spectrum in sample "PbTe w/o capping layer", which is shown in Figure 3.16. A TeO_2 film has been sputtered and serves as the reference sample to identify the two signals in Figure 3.16. We find out the ratio of oxygen bonded with Pb and Te is about 8:1, thus even though both chemical bonds Pb-O and Te-O can be formed, oxygen ions mostly preferentially bond with Pb. This result is consistent with people's postulate of the formation of minority carrier traps $(PbO)^{2+}$ in lead chalcogenides[55].

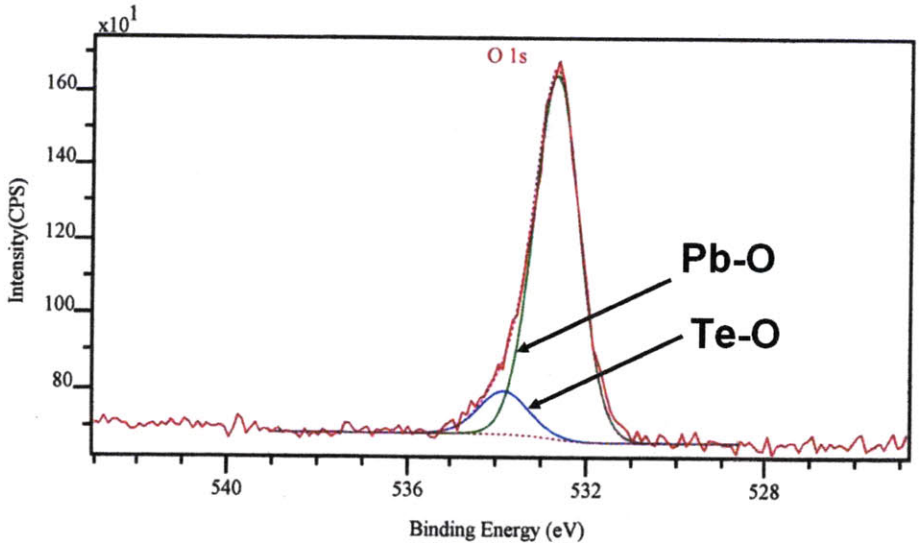

Figure 3.16 Oxygen XPS spectrum (O 1s) obtained after surface oxidation layer of PbTe film is etched away by Ar ion beam.

Hall experiment and temperature dependence of resistivity are studied to further investigate the electronic structure of oxygen sensitized PbTe films. Room temperature carrier concentration values for the above two samples are listed in Table 3.3. Both samples are p-type. Notably, carrier concentration is 3~4 orders of magnitude lower than oxygen concentration, thus the majority of the oxygen incorporated into the PbTe films should be electrically non-active. As we have discussed earlier, oxygen serves as acceptor that can deplete the electrons in the conduction band in lead chalcogenides. Study in part 3.1.3 indicates all PbTe films of different thicknesses after exposed to air have near mid-gap Fermi level (0.11 eV above valence band edge), and the location of the Fermi level does not change afterwards. This suggests the Fermi level in PbTe films has been pinned by the incorporated oxygen. From Table 3.3, the sample "PbTe w/ capping layer" shows much lower carrier concentration than "PbTe w/o capping layer". This could be due to

non-complete Fermi level pinning given much lower oxygen concentration resulted from the oxygen diffusion barrier.

Temperature dependence of resistivity of these two PbTe films further supports the above conclusion. As shown in Figure 3.17, PbTe with capping layer is more resistive than normal PbTe film without capping layer, and the fitted activation energy is also higher. According to results in Figure 3.8 and Table 3.1, mobility shows much weaker temperature dependence, and the exponential dependence of resistivity is mainly due to the carrier concentration. Therefore the fitted activation energy can help locate the Fermi level in the band structure, which is shown in Figure 3.18 for the two samples. In PbTe film without capping layer, oxygen can diffuse into the film through abundant diffusion "short-cuts", i.e. vertically aligned grain boundaries between columnar nanocrystalline grains. Due to this large amount of oxygen incorporation, Fermi level can be pinned completely even thought most oxygen atoms are electrically non-active (non-active: active ~ 10^4:1 according to Table 3.3). In PbTe film with capping layer, however, oxygen can only be introduced into the film during the deposition. After films are exposed to air, further oxygen incorporation is blocked by the $Ge_{23}Sb_7S_{70}$ diffusion barrier. Thus the amount of oxygen in the film is not enough to pin the Fermi level completely and Fermi level is closer to the mid-gap as shown in Figure 3.18 (a). Compared to the theoretical intrinsic carrier concentration at 300 K[77], i.e. 8×10^{15} cm^{-3}, one finds the carrier concentration for the sample "PbTe w/ capping layer" is about one order of magnitude higher. Therefore in order to further reduce the carrier concentration in the PbTe films down to the intrinsic value, the oxygen concentration should be at least one order of

magnitude lower, i.e. ~10^{18} cm^{-3}. This will require background pressure of ~10^{-8} Torr during the deposition and a diffusion barrier before the film is exposed to the air.

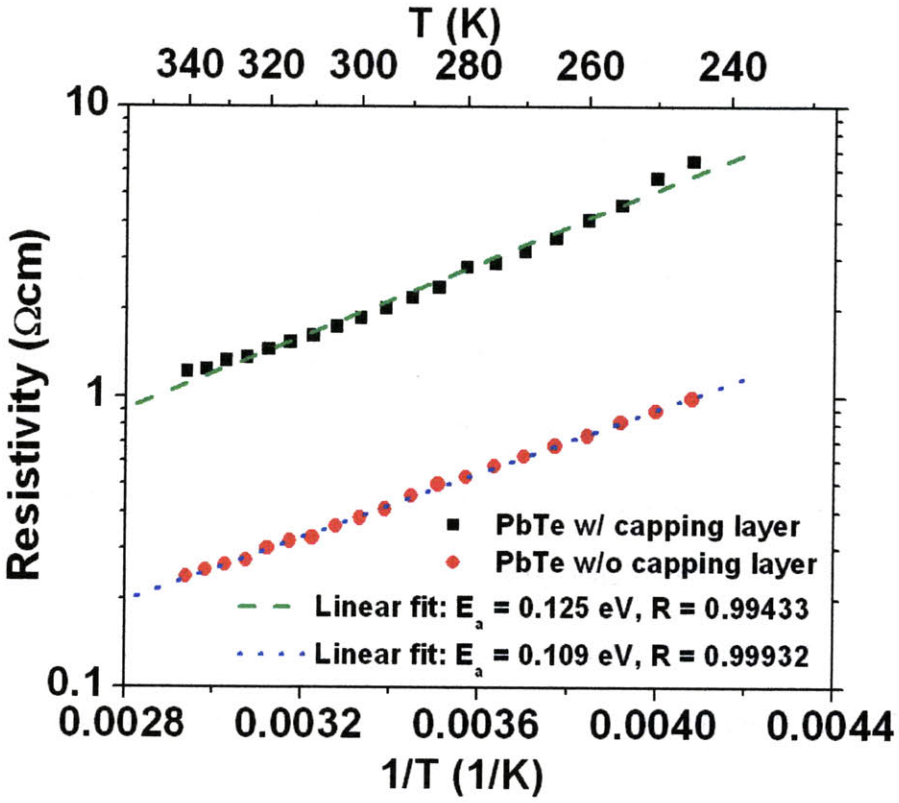

Figure 3.17 Temperature dependence of resistivity of PbTe films with and without $Ge_{23}Sb_7S_{70}$ capping layer.

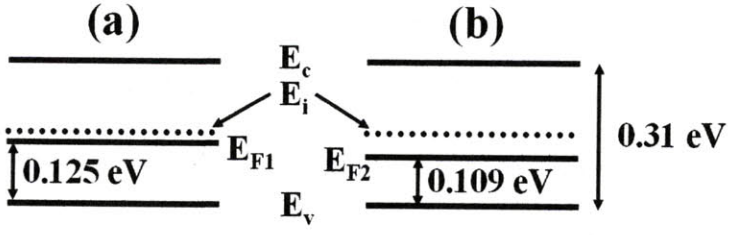

Figure 3.18 Band structure of PbTe films: (a) with and (b) without $Ge_{23}Sb_7S_{70}$ capping layer.

With carrier concentration values (p) at room temperature and activation energy (E_a) listed in Table 3.3, effective density of states for valence band (N_v) can be calculated by:

$$N_v = p\exp\left(\frac{E_F - E_v}{kT}\right) \approx p\exp\left(\frac{E_a}{kT}\right) \tag{3.16}$$

which is also shown in Table 3.3. The values of 8~9 × 10^{18} cm^{-3} agree quite well with the model provided by Galeskii[76]. Two PbTe films with distinct oxygen concentration yield almost the same N_v values, indicating oxygen incorporation just introduces mid-gap states without disrupting the overall band structure.

To sum up, we have demonstrated oxygen exists in our polycrystalline PbTe films and the oxygen preferentially forms bonds with Pb. Oxygen acts as acceptor and pins Fermi level near mid-gap giving rise to the very low carrier concentration and high photoconductivity in PbTe films. Oxygen can be incorporated into the films either during film deposition or through diffusion process once the film is exposed to air. Thus controlling oxygen concentration down to ~10^{18} cm^{-3} during the fabrication process is critical for improving device performance. With capping layer and reduced oxygen residue in the background of the deposition chamber, lower carrier concentration and higher photoconductive signal could be expected. Even though we show the evidence of the existence of minority carrier traps $(PbO)^{2+}$, the carrier lifetime in our PbTe films (~1 ns at -60 °C) is much shorter than values reported for single crystalline PbTe films (100~1000 ns around -60 °C)[77], which is possibly due to the polycrystalline nature of our PbTe films. Annealing at alleviated temperature may increase the carrier lifetime and thus enhance the photoconductivity which has be demonstrated in most polycrystalline PbSe and PbS films[60].

3.3. Summary

In this chapter, we focus on developing thin polycrystalline PbTe film for IR light detection with enhanced signal-to-noise ratio. By varying film thickness, we perform a systematic study on the microstructure, optical, electrical, and photoconductive properties of polycrystalline PbTe films. The films exhibit strong (200) texture with columnar grain microstructures governed by preferential nucleation orientations. The film grain size decreases with decreasing film thickness and reaches an average grain size down to 25 nm for the 100 nm thick film. Further, the vertically aligned grain boundaries serve as diffusion "short-cuts" for oxygen. The unique microstructures of our nanocrystalline films enables oxygen incorporation at room temperature, as is evident by the p-type electrical conduction and high infrared sensitivity of our films. Both carrier number modulation model and our measurement confirm higher responsivity in thinner films than thicker films, and high peak responsivity up to 25 V/W is attained in the 100 nm thick PbTe film.

Detailed noise analysis shows 1/f noise dominates at lower optical modulation frequency (<100 Hz), and Johnson noise is the dominant intrinsic noise in our PbTe photoconductors. We extrapolate a Johnson-noise-limited detectivity of 1.4×10^{10} $cmHz^{1/2}/W$ at -60 °C at 3.6 μm using the measured parameters of our polycrystalline PbTe film, which compares favorably to current commercial mid-IR HgCdTe detectors using single-crystalline materials.

Study on the photoconductivity mechanism in our PbTe films reveals oxygen plays an important role in pinning Fermi level near mid-gap. This leads to very low carrier concentration and excellent photoconductivity in the PbTe films. Oxygen can be introduced into the film either during film deposition or through diffusion process once the film is exposed to air. Thus controlling oxygen concentration down to ~10^{18} cm^{-3} during the fabrication process is essential for device performance improvement. With oxygen diffusion barrier or reduced oxygen residue in the deposition chamber, lower carrier concentration and higher photoconductive signal could be expected.

Chapter 4. Design of resonant-cavity-enhanced (RCE) multispectral infrared (IR) photodetectors[50,52,78]

In last chapter, we have demonstrated polycrystalline PbTe film as thin as 100 nm can be used as mid-IR light absorbing layer. Thinner PbTe films show much higher photo-responsivity and detectivity than thicker films due to strong thickness dependence of these two characteristics. However, experimental results also indicate the quantum efficiency of a single 100 nm thick PbTe layer is only 6.7% at 3.6 μm wavelength. Thus if we could enhance the quantum efficiency as close to 100% as possible, performance will be improved by more than one order of magnitude.

In this chapter we will show how mid-IR distributed Bragg reflector (DBR) is developed to form a cavity structure to enhance the quantum efficiency. The DBR consists sputtered Ge and evaporated As_2S_3 films serving as high and low index materials. Then we discuss how to design such cavity structures with thin PbTe absorbing layers incorporated inside to achieve "critical coupling condition", under which near unity quantum efficiency can be realized. Meanwhile, we theoretically analyze a novel design of cavity-enhanced photodetectors capable of sensing multiple wavelengths simultaneously in a *single* pixel. The design is based on phase-tuned propagation of resonant modes in cascaded planar resonant cavities. We show that this concept can be generalized to detect multiple wavelength combinations covering the entire near to far infrared spectrum. Besides its multispectral detection capability, the design also features minimal spectral cross talk and significantly suppressed noise. The intrinsic design versatility and scalability, as well as

process compatibility with planar microfabrication, suggest the design's wide application potential for telecommunications, infrared imaging, and biochemical sensing.

4.1. Distributed Bragg reflector (DBR) for mid-IR[52]

As shown previously in Figure 1.4, in order to form a cavity structure, two mirror stacks are required to sandwich the cavity region. Light of resonant wavelength will then be trapped in the cavity region and interact with the absorbing layer in this region. One prerequisite for the two mirror stacks is high transparency in the wavelength range of our interest, i.e. mid-IR (3~5 μm). As we will discuss later, the reflectance value of the mirror stack should be adjustable to obtain "critical coupling condition". Thus we use one-dimensional photonic crystals (1d-PC) serving as distributed Bragg reflectors (DBR, the mirror stacks), since their reflectance values can be easily modified by changing bilayer number or film thickness. Ge and As_2S_3 films are employed as high and low index materials to fabricate 1d-PC given their excellent mid-IR transparency and large refractive index contrast. At first we will show how single layers of these two materials could be fabricated and their optical properties could be calculated. Afterwards, fabrication and demonstration of a 1d-PC designed for 3.6 μm will be provided.

4.1.1. Optical properties of single layer films: Ge and As_2S_3

2" diameter poly-Ge with Cu backing plate of 99.999% purity from Williams Advanced Materials is used as sputtering target, and As_2S_3 bulk of 99.999% purity from Amorphous Materials Inc. is used as the source material for thermal evaporation. Both the sputtering and the thermal evaporation are carried out at a base pressure lower than 5×10^{-7} Torr. Si

wafers (6" Si wafers with 3 μm oxide) and optically polished CaF_2 discs are used as starting substrates. Films deposited on CaF_2 discs are used for optical property measurements given the IR transparency of CaF_2. The substrates are held on a rotating substrate holder, at room temperature, throughout the depositions. Film deposition rate is monitored in real-time through two separate quartz crystal sensors and is maintained at 1.3 Å/s for Ge, and ~10 Å/s for As_2S_3.

Profilometry measurements performed on single-layer Ge and As_2S_3 films yield excellent uniformity across an entire substrate with thickness variations < 3%. X-ray diffraction analysis on both Ge and As_2S_3 films confirms their amorphous nature. Figures 4.1 (a) and 4.1 (b) show the transmittance spectra of single layers of sputtered Ge and evaporated As_2S_3 films respectively. Both materials show excellent transparency in the mid-IR wavelength range. The fringes in both curves are due to the interference effect.

Using Swanepoel approach coupled with Cauchy's dispersion formula[43], refractive index n and extinction coefficient k of Ge and As_2S_3 have been calculated from their transmittance spectra, as shown in Figures 4.2 (a) and 4.2 (b). Strong wavelength dependence of refractive index and absorption are observed from 0.9 μm to 3 μm in the result of Ge, as shown in Figure 4.2 (a). As_2S_3 shows weaker wavelength dependence of refractive index and higher transparency in this range, as shown in Figure 4.2 (b). For a rigorous design of resonant-cavity-enhanced (RCE) photodetectors, the wavelength dependence of n and k values is critically important in determining the thickness of each layer and the resonant wavelength, and thus should be taken into account.

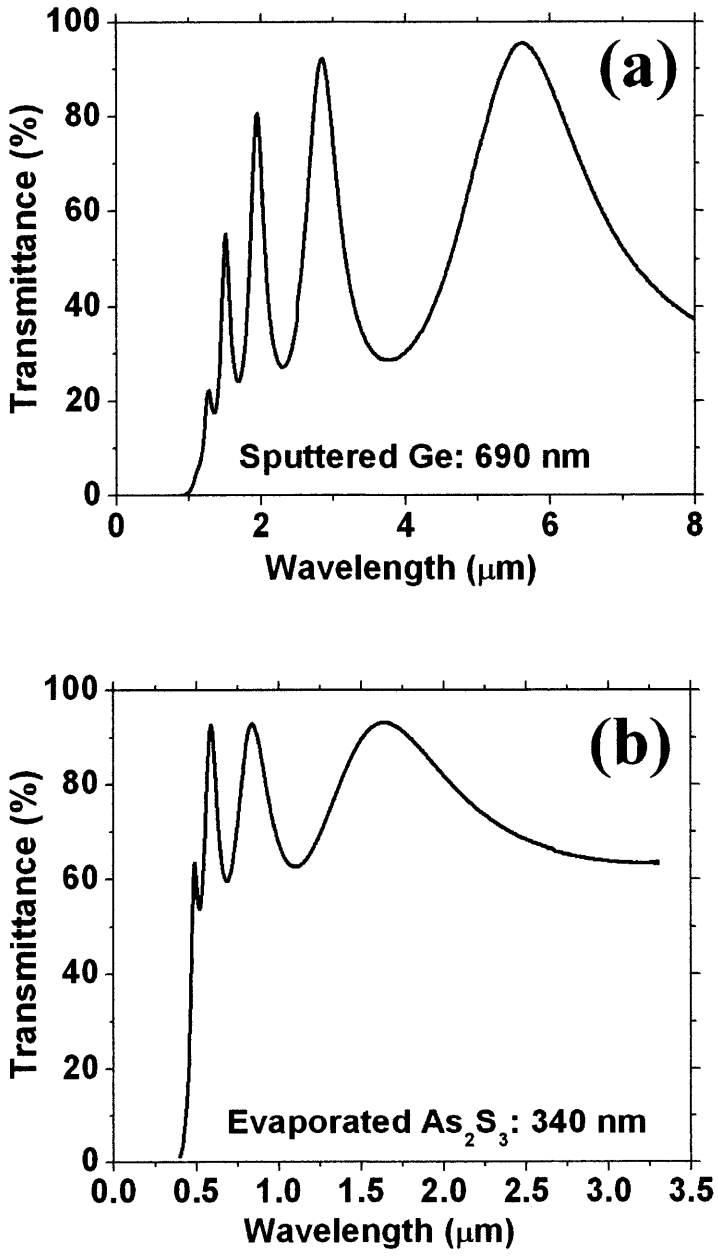

Figure 4.1 Transmittance spectra of (a) sputtered Ge and (b) thermally evaporated As_2S_3 on CaF_2 show excellent transparency in mid-IR wavelength range.

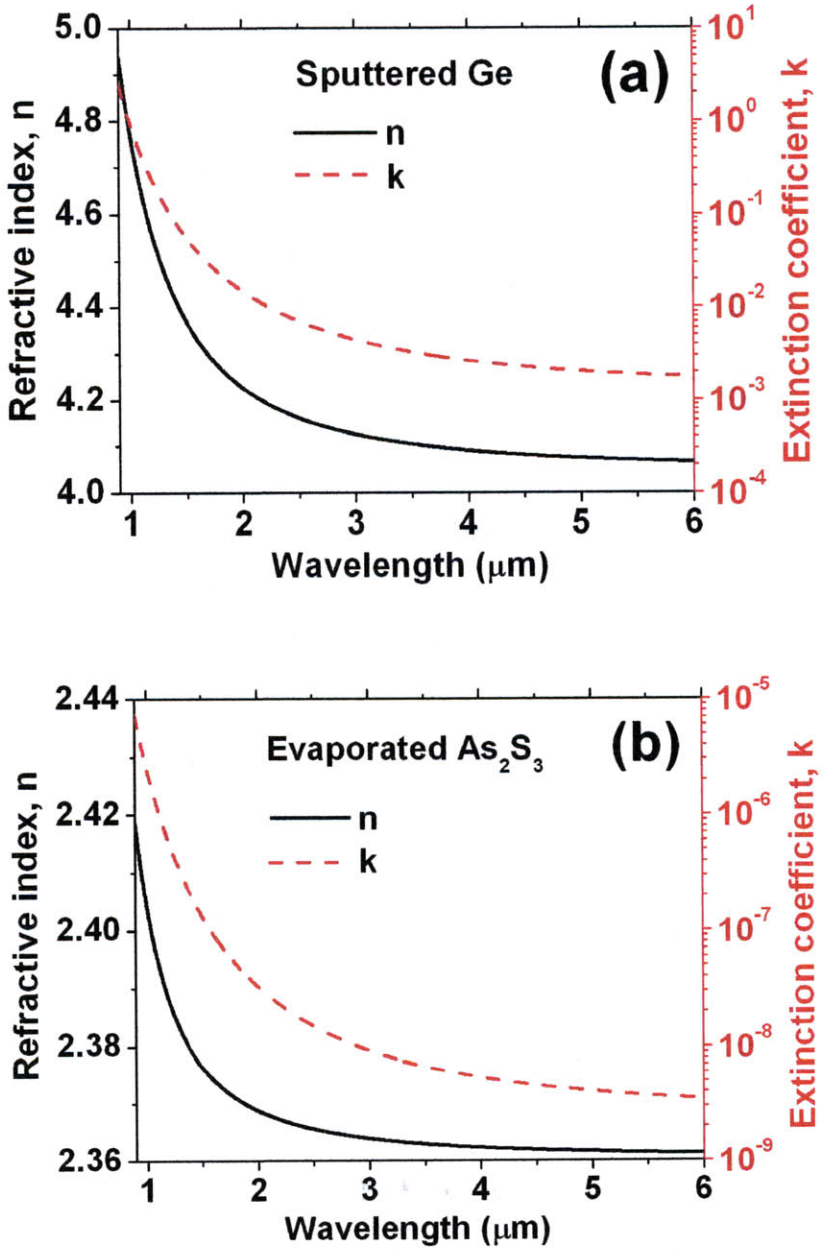

Figure 4.2 Refractive index n and extinction coefficient k of (a) sputtered Ge and (b) thermally evaporated As_2S_3 calculated from the transmittance spectra in Figure 4.1, using Swanepoel approach coupled with Cauchy's dispersion formula. Ge shows strong wavelength dependence of refractive index and absorption in the 0.9~3 μm range, while As_2S_3 shows weaker wavelength dependence of refractive index and higher transparency in this range. These effects are critically important in determining the thickness of each layer and the resonant wavelength for the design of RCE photodetectors.

4.1.2. Fabrication and optical property of $(Ge/As_2S_3)_3/Ge$ DBR

Based on optical properties obtained for Ge and As_2S_3 films, one-dimensional photonic crystal (1d-PC) serving as mid-IR DBR mirror stack has been designed, fabricated, and tested. The 1d-PC is designed to have maximum reflectance value at 3.6 μm. Quarter wavelength stack of 219 nm thick Ge and 381 nm thick As_2S_3 is deposited layer by layer in a single chamber without breaking the vacuum as shown in Figure 4.3. Two pre-calibrated quartz crystal sensors are used to monitor the deposition rate and thickness of Ge and As_2S_3 films separately.

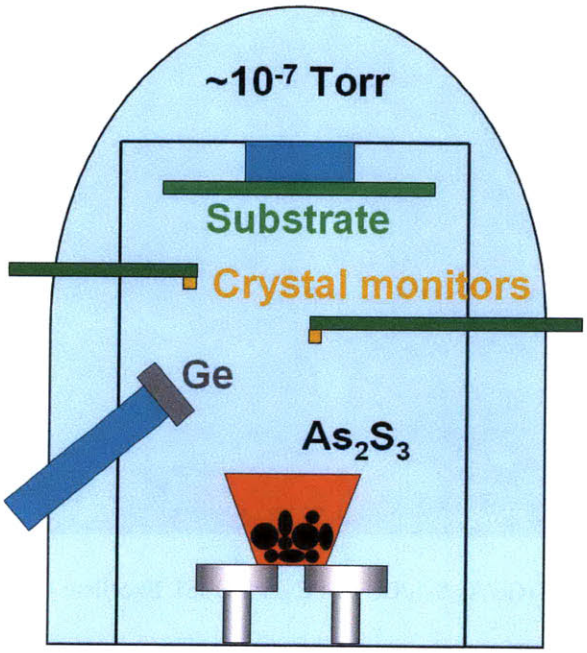

Figure 4.3 Configuration of deposition chamber for $(Ge/As_2S_3)_3/Ge$ mid-IR 1d-PC fabrication.

Figure 4.4 shows the cross-sectional SEM image of the $(Ge/As_2S_3)_3Ge$ quarter wavelength stack we have fabricated on SiO_2/Si substrate. Figure 4.5 shows the reflectance spectrum of this 1d-PC and the simulated curve based on transfer matrix method[79]. The agreement between experiment and simulation indicates excellent film thickness control and uniformity. The spectra feature a photonic band gap (PBG) from 3 μm to 5 μm, with reflectance higher than 99% in the range of 3.5~3.8 μm, again in excellent agreement with the designed operating wavelength of 3.6 μm.

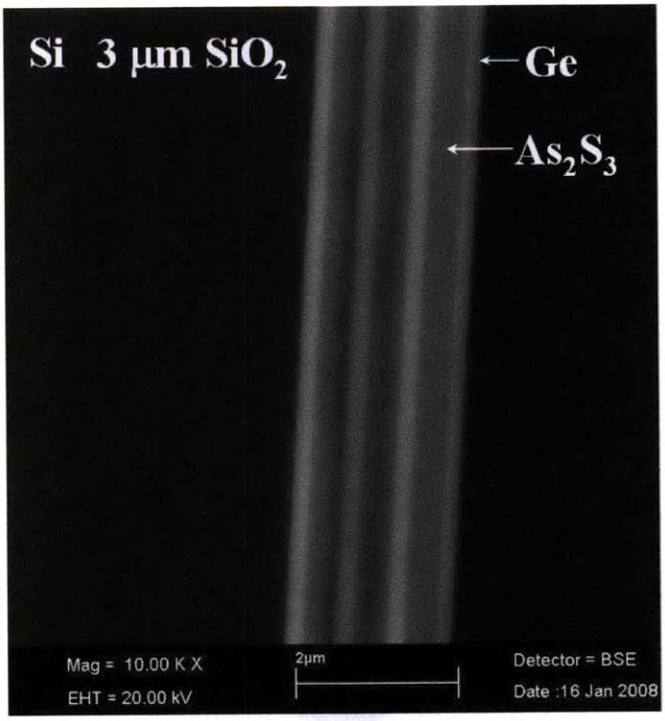

Figure 4.4 SEM image of $(Ge/As_2S_3)_3/Ge$ 1d-PC on SiO_2/Si. Excellent film thickness control and uniformity are demonstrated. The thickness of Ge is monitored to be 219 nm during deposition, and the thickness of As_2S_3 is 381 nm.

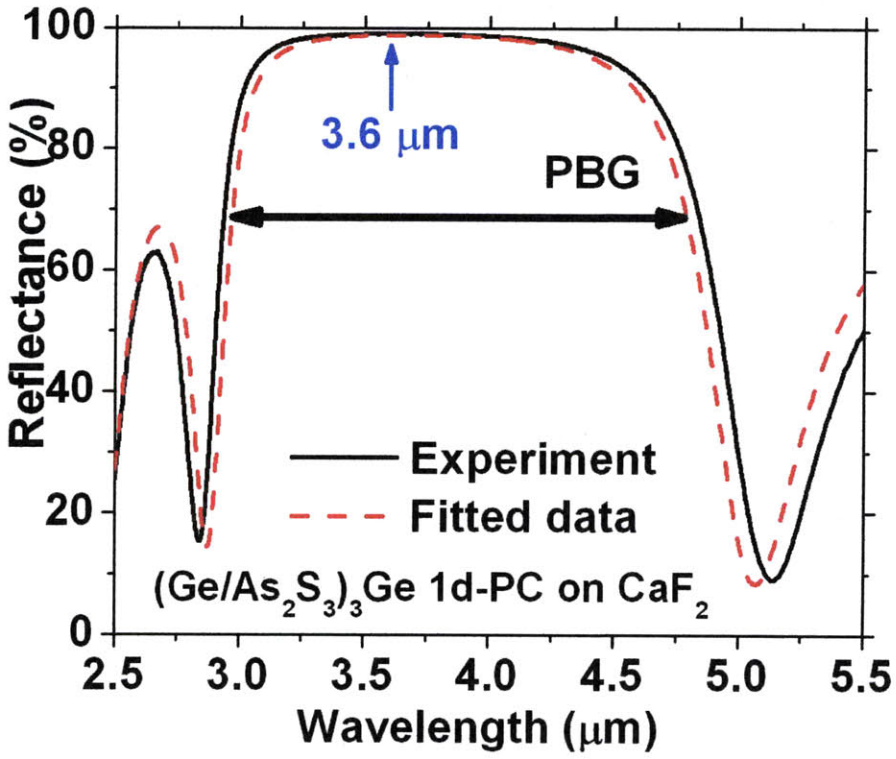

Figure 4.5 Reflectance spectra of $(Ge/As_2S_3)_3/Ge$ 1d-PC. Solid line: experimental data; dotted line: simulated spectrum. This 1d-PC is designed to have maximum reflectance at 3.6 μm wavelength. The experimental spectrum features a photonic band gap from 3 μm to 5 μm, with reflectance higher than 99% in the range of 3.5~3.8 μm. The agreement between experiment and simulation indicates excellent film thickness control and uniformity.

4.2. RCE multispectral photodetectors using phase-tuned propagation[50,78]

Multispectral infrared (IR) detection has been widely employed for applications including hyperspectral imaging, IR spectroscopy, and target identification. Traditional multispectral detection technology is based on the combination of single spectral Focal Plane Arrays (FPAs) and spectral filters or spectrometers, which require bulky, high-cost mechanical scanning instruments and have a slow response. Single pixels capable of detecting multiple wavebands simultaneously enable dramatically simplified system

design with superior mechanical robustness and thus have become the focus of third generation FPA development[9]. Recently, three-color HgCdTe photodiodes have been demonstrated, although their spectral cross talk is still large (> 10%)[18]. A competing multi-color detector technology is quantum-well IR photodetectors (QWIPs)[9]. However, QWIP device optimization is limited by its low quantum efficiency (< 10%)[17]. Other alternative solutions like tandem detectors have limited band selection options and large cross talk due to challenges associated with material compatibility and radiative coupling. A solution which combines high quantum efficiency and low spectral cross talk is yet to be explored.

Our approach involves a multi-layer cascaded cavity structure shown schematically in Figure 4.6. Each wavelength to be detected leads to a unique resonant cavity mode locally confined within its dedicated cavity, where an absorbing active layer is placed for spectral selective detection of this wavelength. The major challenge is the spatial localization of the resonant modes without compromising quantum efficiency. Our solution employs a novel phase-tuned propagation design. In this approach, we insert phase-tuning layers between the cascaded cavities to control the optical phase and hence the coupling strength between the incident light and the resonant modes. Thereby, we show that near unity quantum efficiency (QE) can be achieved for all cavities. Comparing to previous work on multispectral detection using a single cavity[80], spectral cross talk is significantly suppressed given the wavelength-selective spatial localization of resonant modes in different cavities. Electrical signal originating from each wavelength may be separately read out by contacting the corresponding active layer, either in a

photoconductive[80] or in a photovoltaic mode. Further, since resonant cavity enhancement effect leads to field build-up in the cavity and dramatically increases absorption, IR-active layers with reduced thickness can be used while maintaining near unity QE. Consequently, photodetector noise can be suppressed without compromising responsivity. In this part, we theoretically analyze the design principles of the multispectral pixel design using the transfer matrix method (TMM). These principles are then illustrated by a specific design example based on our previously developed materials: evaporated polycrystalline PbTe, sputtered Ge, and evaporated As_2S_3 films.

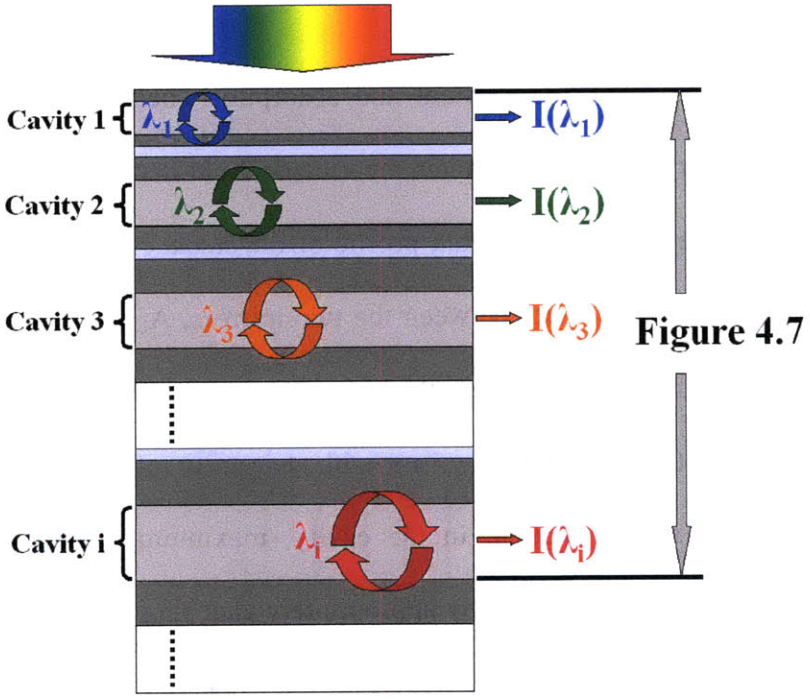

Figure 4.7

Figure 4.6 A cross-sectional schematic of a multispectral photodetector consisting of cascaded planar resonant cavities based on the phase-tuned propagation concept (not drawn to scale).

4.2.1. Analytical formulation

To start with, we consider an IR active layer sandwiched in a generic multi-layer resonant cavity stack, near-unity quantum efficiency can be attained when the critical coupling condition is met at the resonant wavelength[81]:

$$R_t = (1 - A_L)R_b,\ R_b \to 1 \tag{4.1}$$

where R_t and R_b are the reflectance values of top and bottom mirrors, and A_L denotes the optical resonant mode loss*. When the cavity quality factor Q >> 1, A_L can be calculated using cavity pertubration theory as[82]:

$$A_L = \varepsilon d \cdot \frac{\int_{active} \alpha |E_0|^2 \, dV}{\int_{stack} \varepsilon_c |E_0|^2 \, dV} \tag{4.2}$$

where ε and α are the dielectric constant and absorption coefficient of the IR active material, d is the cavity length, E_0 denotes the electric field distribution of the resonant mode, and ε_c gives the dielectric constant profile of the stack. Notably, when the active material completely fills the cavity between the two mirrors, A_L can simply be given as $(1\text{-}e^{-2\alpha d})$ and Equation 4.1 reduces to the critical coupling formulation by Unlu[83]. Equation 4.1 states that given a bottom mirror with near unity reflectance ($R_b \to 1$) and a specific thickness of active material in the cavity, maximum quantum efficiency at resonant wavelength may be obtained by appropriately choosing a top mirror reflectance (R_t) to satisfy Equation 4.1. Intuitively, there are two situations which can deviate from the critical coupling condition: if the top mirror is highly reflective, most of the incident

---

* Critical coupling condition expressed by Equation 4.1 is a very good approximation in our case. Strict formulation should use quality factors instead of reflectance values. More detailed discussion can be found in chapter 5.

light will be reflected back and cannot "feel" the existence of the absorbing layer in the cavity; if the top mirror is highly transparent, light cannot be trapped in the cavity region completely due to the top mirror loss. Thus there exists an optimal top mirror design to achieve the condition when light can be fully trapped and totally get absorbed by the absorbing layer.

Now we apply the above analysis to the ith (i = 1, 2, 3...) cavity in the cascaded structure shown in Figure 4.6. As is shown in Figure 4.7, the "top mirror" of the ith cavity essentially includes cavities 1 to i-1. In order to satisfy Equation 4.1, we insert an additional coupling-matching layer m in the top mirror stack. As we show below, incorporation of such a layer allows effective tuning of the top mirror reflectance $R_{t,i}$ (the 2^{nd} subscription i denotes the sequential number of cavity in the stack), and thereby the critical coupling condition can be met by choosing an appropriate coupling-matching layer thickness.

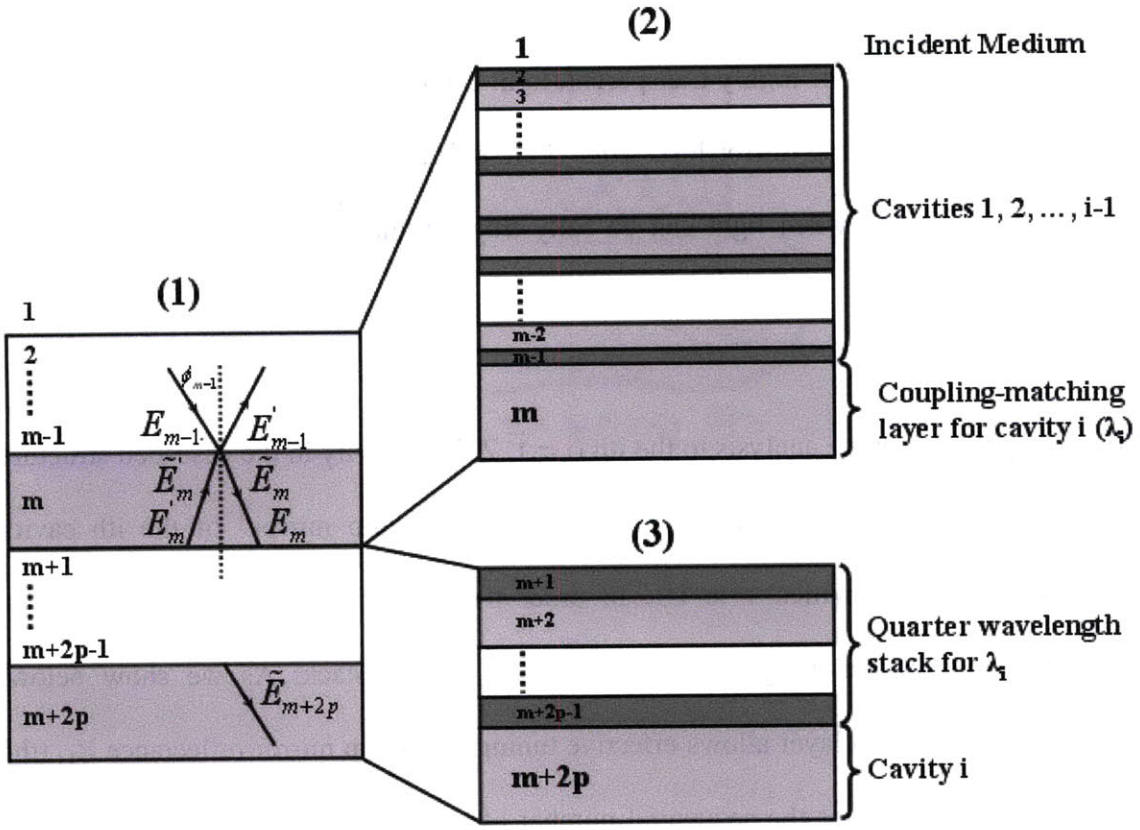

Figure 4.7 Structures used in deriving the coupling-matching condition for cavity i. Stack (1) is the entire structure which can be decomposed into stack (2) and stack (3). The layers corresponding to stack (1) are also shown in Figure 4.6.

Here we use TMM to derive the top mirror reflectance $R_{t,i}$ of the ith cavity in the stack, as is shown in Figure 4.7. Following the convention of Sun[79], we label the layers sequentially starting from the incident medium. The electric field of the transmitted light $\tilde{E}_{m+2p}$ is given as:

$$\begin{pmatrix} \tilde{E}_{m+2p} \\ 0 \end{pmatrix} = \begin{pmatrix} tE_1 \\ 0 \end{pmatrix} = M_{m+2p}^{-1} \cdot \left(M_{m+2p-1} \cdot L_{m+2p-1} \cdot M_{m+2p-1}^{-1}\right) \cdots \left(M_{m+1} \cdot L_{m+1} \cdot M_{m+1}^{-1}\right) \cdot \left(M_m \cdot L_m \cdot M_m^{-1}\right) \cdot$$
$$\cdot \left(M_{m-1} \cdot L_{m-1} \cdot M_{m-1}^{-1}\right) \cdots \left(M_2 \cdot L_2 \cdot M_2^{-1}\right) \cdot M_1 \cdot \begin{pmatrix} E_1 \\ E_1' \end{pmatrix} = T_f \cdot \begin{pmatrix} E_1 \\ rE_1 \end{pmatrix} \tag{4.3}$$

$$M_j = \begin{cases} \begin{pmatrix} 1 & 1 \\ \frac{n_j}{\mu_j}\cos\phi_j & -\frac{n_j}{\mu_j}\cos\phi_j \end{pmatrix}, s-wave \\ \begin{pmatrix} \cos\phi_j & \cos\phi_j \\ \frac{n_j}{\mu_j} & -\frac{n_j}{\mu_j} \end{pmatrix}, p-wave \end{cases} \tag{4.4}$$

$$L_j = \begin{pmatrix} e^{i\delta_j} & 0 \\ 0 & e^{-i\delta_j} \end{pmatrix}, \delta_j = \frac{2\pi}{\lambda} n_j t_j \cos\phi_j \tag{4.5}$$

where E_1 and $E_1^{'}$ are incident and reflected electric field components in the incident medium, ϕ_j denotes the incident angle of light at the interface of jth layer and (j+1)th layer, n_j, μ_j and t_j are refractive index, relative permeability, and thickness of the jth layer, r and t are the complex amplitude reflectivity and transmissivity of the top mirror, and λ is the wavelength of incident light. It is obvious that $r = -\frac{T_{f21}}{T_{f22}}$ and $R_{t.i} = |r|^2$.

The transfer matrix T_f of the entire stack may be written as:

$$T_f = T_{(3)} \cdot M_1^{-1} \cdot M_m \cdot L_m \cdot T_{(2)} \tag{4.6}$$

where $T_{(2)}$ corresponds to the transfer matrix of layers from the 1st to the (i-1)th cavity including the mth coupling-matching layer, and $T_{(3)}$ is transfer matrix of the quarter wavelength stack (QWS) designed for the ith cavity's resonant wavelength λ_i. It can be proven that the matrix $T_{(2)}$ may be generically represented as:

$$T_{(2)} = M_m^{-1} \cdot \left(M_{m-1} \cdot L_{m-1} \cdot M_{m-1}^{-1}\right) \cdots \left(M_2 \cdot L_2 \cdot M_2^{-1}\right) \cdot M_1 = \begin{pmatrix} T_{(2)22} e^{-i\theta_{22}} & T_{(2)21} e^{-i\theta_{21}} \\ T_{(2)21} e^{i\theta_{21}} & T_{(2)22} e^{i\theta_{22}} \end{pmatrix} \tag{4.7}$$

where $T_{(2)21}$, $T_{(2)22}$, θ_{21}, and θ_{22} are functions of ϕ_j, n_j, μ_j, t_j (j = 1 to m), and λ. Equation 4.7 is valid for both s-wave and p-wave. In high-index-contrast Bragg cavities, the angular dependence of spectral response is minimal[84]. In the design example we show below, the resonant wavelength shifts less than 2% at an incidence angle from air of 30°. Therefore, practically we only need to consider normal incidence light. $T_{(3)}$ follows the general formulation of QWS transfer matrices at normal incidence ($\lambda = \lambda_i$, p pairs):

$$T_{(3)} = M_{m+2p}^{-1} \cdot \left(M_{m+2p-1} \cdot L_{m+2p-1} \cdot M_{m+2p-1}^{-1}\right) \cdots \left(M_{m+1} \cdot L_{m+1} \cdot M_{m+1}^{-1}\right) \cdot M_1 = (i)^{2p-1} \cdot \begin{pmatrix} A+B & -A+B \\ A-B & -A-B \end{pmatrix} \tag{4.8}$$

$$\text{where } A = \frac{n_1}{2n_{m+2p-1}} \cdot \left(\frac{n_{m+2}}{n_{m+1}}\right)^{p-1}, B = \frac{n_{m+2p-1}}{2n_{m+2p}} \cdot \left(\frac{n_{m+1}}{n_{m+2}}\right)^{p-1} \tag{4.9}$$

Substituting Equations 4.7 and 4.8 into Equation 4.6, we have:

$$R_{t,i} = |r|^2 = \left|-\frac{T_{f21}}{T_{f22}}\right|^2 = \left|\frac{A \cdot n_m \cdot \left(T_{(2)21} e^{i(\theta_{21}+\theta_{22})} - T_{(2)22} e^{2i\delta_m}\right) + B \cdot n_1 \cdot \left(T_{(2)21} e^{i(\theta_{21}+\theta_{22})} + T_{(2)22} e^{2i\delta_m}\right)}{A \cdot n_m \cdot \left(T_{(2)22} e^{i(\theta_{21}+\theta_{22})} - T_{(2)21} e^{2i\delta_m}\right) + B \cdot n_1 \cdot \left(T_{(2)22} e^{i(\theta_{21}+\theta_{22})} + T_{(2)21} e^{2i\delta_m}\right)}\right|^2 \tag{4.10}$$

where $\delta_m = \frac{2\pi}{\lambda_i} n_m t_m$, and n_m and t_m are refractive index and thickness of the mth layer, i.e. the coupling-matching layer at λ_i. Equation 4.10 suggests that the mirror reflectance $R_{t,i}$ is a periodic function of t_m, and the period is $\frac{\lambda_i}{2n_m}$. Such a functional dependence provides a lever to tune $R_{t,i}$ simply by adjusting t_m to satisfy Equation 4.1 and thereby reach near unity quantum efficiency. In the example we give later, we illustrate how the critical coupling condition can be solved graphically.

There are two special cases though where the $R_{t,i}$ tuning mechanism fails. To see that, we note that the reflectance of stack (2) is given by $R_{(2)} = \left| \frac{T_{(2)21}}{T_{(2)22}} \right|^2$. When the resonant wavelength of the ith cavity λ_i falls in one of the photonic stop bands of cavities 1 to i-1, $R_{(2)} \sim 1$. This is equivalent to $\left|T_{(2)21}\right| \approx \left|T_{(2)22}\right|$; under this condition, Equation 4.10 reduces to $R_{t,i} \approx 1$ regardless of the value of t_m. In the second case, $R_{(2)} \sim 0$. This happens when λ_i coincides with the reflectance minimum of ripples outside the photonic stop bands of cavities 1 to i-1. Thus $\left|T_{(2)21}\right| \approx 0$ and Equation 4.10 becomes $R_{t,i} \approx \left| \frac{An_m - Bn_1}{An_m + Bn_1} \right|$, suggesting $R_{t,i}$ is independent on t_m. Both of these special cases can be avoided by properly choosing the refractive index contrast of mirror materials in cavities 1 to i.

To summarize, we can follow the generic procedures to design multispectral detectors for selectively detecting N different wavelengths $\lambda_1, \lambda_2, \ldots \lambda_N$:

(1) Select mirror materials for the N wavelengths to avoid overlapping λ_i and the photonic stop bands of cavities 1 to i-1, and to minimize parasitic loss due to mirror absorption;

(2) Start from the first cavity on top of the stack, choose appropriate numbers of top/bottom mirror QWS pairs to satisfy Equation 4.1;

(3) Move on to the next cavity i, adjust the coupling-matching layer thickness sandwiched between cavity i-1 and cavity i so that the critical coupling condition is met;

(4) Repeat step (2) and (3) until the entire stack design is completed.

The design procedures ensure that near unity quantum efficiency is attained for all N different wavelengths; in addition, as we will show in the following example, the high degree of modal spatial localization ensures minimal cross talk between the different wavelengths to be detected.

4.2.2. Simulation of complex top mirror stack

To validate the tunability of $R_{t,2}$ in Equation 4.10, $\lambda_1 = 1.55$ μm is chosen as the shorter wavelength trapped by cavity 1, and then we change second wavelength to be detected λ_2 and the thickness of the coupling-matching layer $t_m(As_2S_3)$. Sputtered Ge and evaporated As_2S_3 are chosen to form the whole structure shown in Figure 4.7, and their refractive indices are fixed at 4.101 and 2.363 respectively.

Firstly, we design critically coupled cavity 1 to trap near-IR light at resonant wavelength λ_1 ($\lambda_1 = 1.55$ μm). Since no material absorption has been considered, the optical resonant mode loss $A_L = 0$. According to Equation 4.1, as long as $R_t = R_b$, critical coupling condition will be satisfied and light of λ_1 will be trapped in the cavity. In part 4.1.2, we demonstrate quarter wavelength stack of only 3.5 pairs, i.e. $(Ge/As_2S_3)_3Ge$, shows over 99% reflectance. Thus we employ 3.5 and 4.5 pairs for the top and bottom DBR mirrors. The thickness of the cavity is chosen to be one half of the wavelength, so only the first order mode can be supported by the cavity.

Figure 4.8 shows the simulated reflectance spectrum of cavity 1 by TMM, which is also shown as stack (2) in Figure 4.7, i.e. Air/$(Ge/As_2S_3)_3$/Ge/(As_2S_3 cavity)/Ge/$(As_2S_3/Ge)_4/As_2S_3$. In order to test Equation 4.10, we choose several wavelengths as λ_2 and design quarter wavelength stack (QWS) for each λ_2 accordingly, which is shown as stack (3) in Figure 4.7, i.e. Air/$(Ge/As_2S_3)_1$/Ge/As_2S_3. The reflectance value of this QWS equals to 0.8298 at each λ_2. The location of these wavelength λ_2 is indicated in Figure 4.8 and also listed in Table 4.1. Varying the thickness of the coupling-matching layer As_2S_3 between cavity 1 and QWS for λ_2, we simulate the reflectance value $R_{t,2}$ of the stack (1) in Figure 4.7, and the result is shown in Figure 4.9.

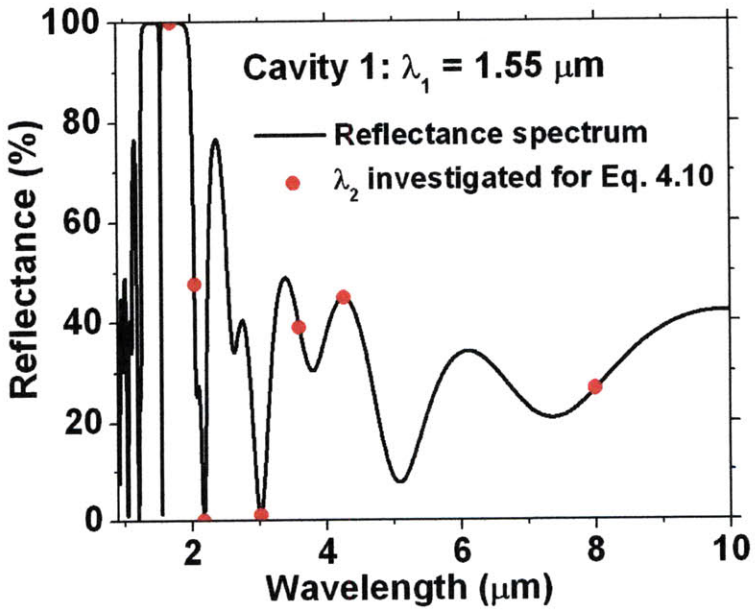

Figure 4.8 Reflectance spectrum of cavity 1 for λ_1 = 1.55 μm. Cavity 1 is also shown as stack (2) in Figure 4.7. As_2S_3 and Ge are used as low and high index materials. Cavity 1 is designed to support only the first order resonant cavity mode. The red solid dots denote several wavelength locations used as wavelength λ_2 to verify Equation 4.10.

Table 4.1 Wavelengths as λ_2 investigated to demonstrate tunability of $R_{t,2}$ in Equation 4.10 by changing the thickness of coupling-matching layer As_2S_3.

Wavelength λ_2 (μm)	Reflectance of cavity 1($R_{(2)}$ of stack (2) in Figure 4.7)	$R_{t,2}$ when t_m=0	$R_{t,2}$ when t_m varies from 0 to 1.4 μm
1.7	0.9995	0.9989	0.9956~0.9999
2.04	0.4760	0.9204	0.0644~0.9223
2.173	0.0013	0.6223	0.6211~0.6629
3.014	0.0110	0.6925	0.5784~0.6992
3.6	0.3901	0.8889	0.1258~0.9032
4.257	0.4479	0.1009	0.0815~0.9164
8	0.2652	0.7962	0.2382~0.8684

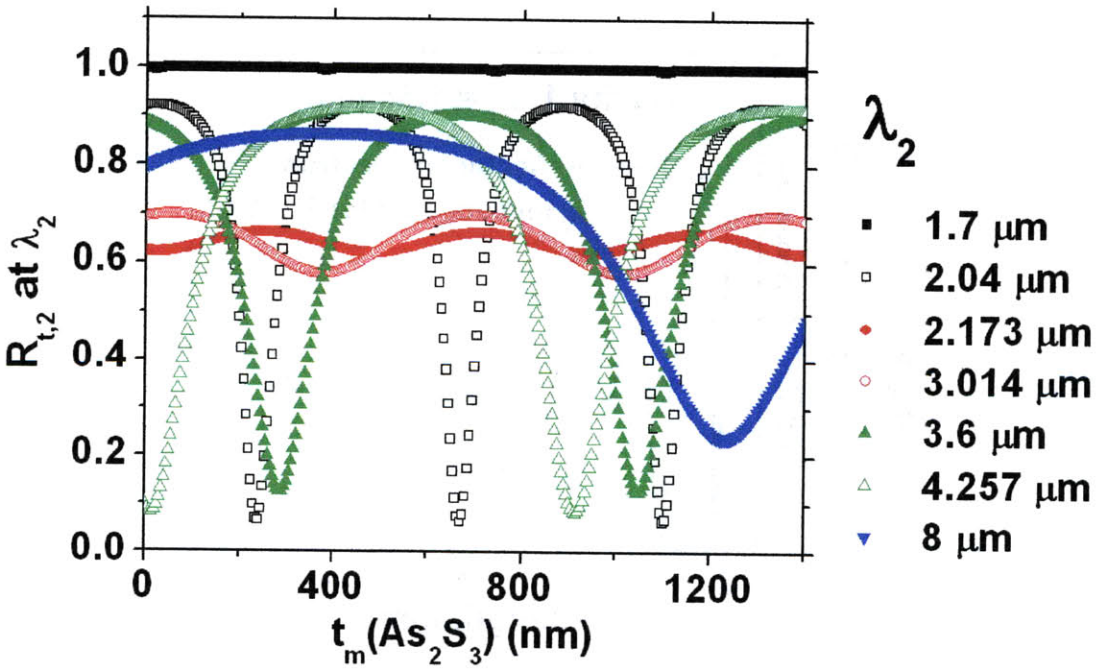

Figure 4.9 $R_{t,2}$ values at λ_2 for different wavelengths chosen as λ_2. The simulated structure is shown as stack (1) in Figure 4.7. Consistent with Equation 4.10, $R_{t,2}$ shows periodic dependence on the thickness of the coupling-matching layer As_2S_3 which is sandwiched by cavity 1 and QWS of λ_2. Tunability of $R_{t,2}$ is clearly seen for each chosen λ_2.

In Figure 4.9, we demonstrate when the thickness of the coupling-matching layer As_2S_3 is changed from 0 nm to 1400 nm, $R_{t,2}$ can be tuned continuously and a fairly broad range (0.1~0.9) can be obtained. The tunable range of $R_{t,2}$ for each λ_2 is also summarized in Table 4.1 (4^{th} column). This result is consistent with Equation 4.10. The period of $\frac{\lambda_2}{2n_m}$ predicted by Equation 4.10 is also clearly observed in Figure 4.9. As we have discussed before, reflectance value at λ_2 of cavity 1 (2^{nd} column in Table 4.1) will influence the effectiveness of the coupling-matching layer. As shown in Table 4.1 and Figure 4.9, when λ_2 = 1.7 μm which falls into the photonic stop band of cavity 1, $R_{(2)}$ = 0.9995 ~ 1. Thus $R_{t,2}$ ~ 1 and $R_{t,2}$ is independent on $t_m(As_2S_3)$. When λ_2 = 2.173 μm (or 3.014 μm), $R_{(2)}$ = 0.0013 (or 0.0110) ~ 0. Therefore $R_{t,2}$ shows very weak periodic dependence on $t_m(As_2S_3)$ and its tunable range is much narrower than other λ_2. Figure 4.9 also suggests that the closer $R_{(2)}$ approaches 0, the narrower the tunable range of $R_{t,2}$.

4.2.3. Design example of dual waveband RCE photodetectors

As an example to validate the principles, we have designed a dual waveband RCE photodetector for λ_1 = 1.55 μm and λ_2 = 3.6 μm. More realistic material properties are used. Evaporated PbTe, sputtered Ge, and evaporated As_2S_3 are chosen as the three materials to form the dual waveband RCE photodetector. As_2S_3 and Ge are used as the low and high index mirror materials given their IR transparency. And their wavelength-dependent refractive indices are calculated from experimentally measured transmittance spectra using the Swanepoel approach as discussed in part 4.1.1. PbTe layers of 50 nm

and 100 nm in thickness are used as IR absorbers in two cascaded cavities, and the refractive indices are measured using IR ellipsometry as discussed in part 2.4.

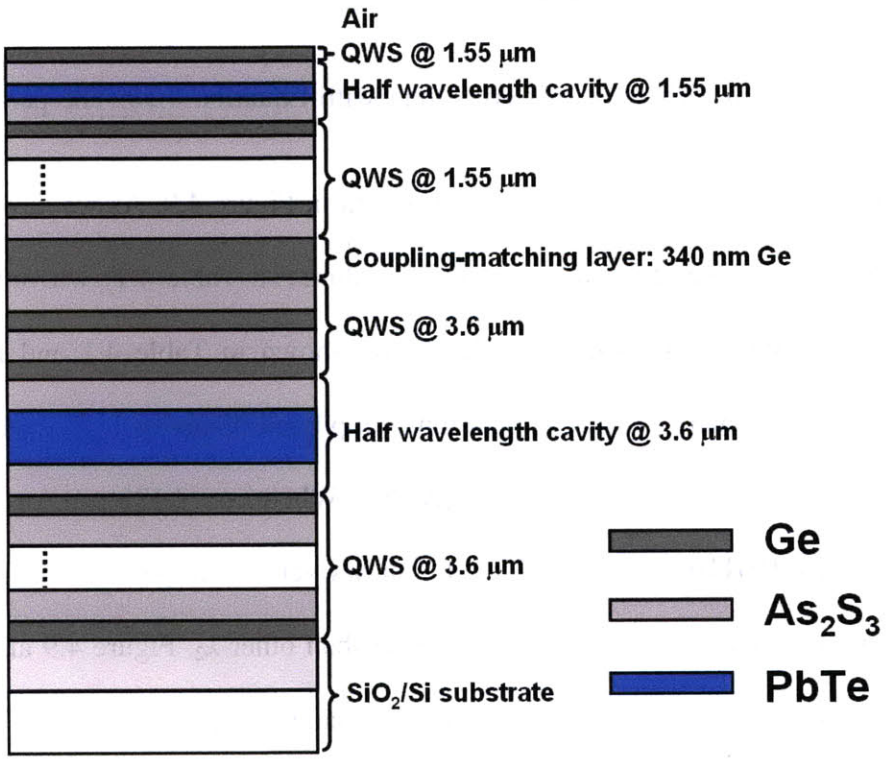

Figure 4.10 Schematic cross section of the photodetector designed to detect 1.55 μm and 3.6 μm wavelengths simultaneously.

Figure 4.10 shows a schematic cross-section of the photodetector designed following the procedures detailed above. The solid curves in Figure 4.11 plot $R_{t,2}$ as a function of coupling-matching layer's thickness (t_{Ge}) for different QWS pair numbers, the dashed line indicates the reflectance corresponding to the critical coupling condition Equation 4.1, and the green crosses denote the thickness values at which Equation 4.1 is met. Here we use a 340 nm thick Ge layer sandwiched between the two cavities as the coupling-matching layer. Using TMM, the electric field distribution across the photodetector's

whole structure is calculated as a function of wavelength, and then the quantum efficiency spectra in two PbTe absorbers can be calculated separately by[79]:

$$\mathrm{QE}(\lambda) = n \cdot \int_{active} \alpha \left| E(\lambda, z) \right|^2 dz \tag{4.11}$$

where n and α are the refractive index and absorption coefficient of PbTe, and E(λ, z) denotes the electric field distribution across the photodetector.

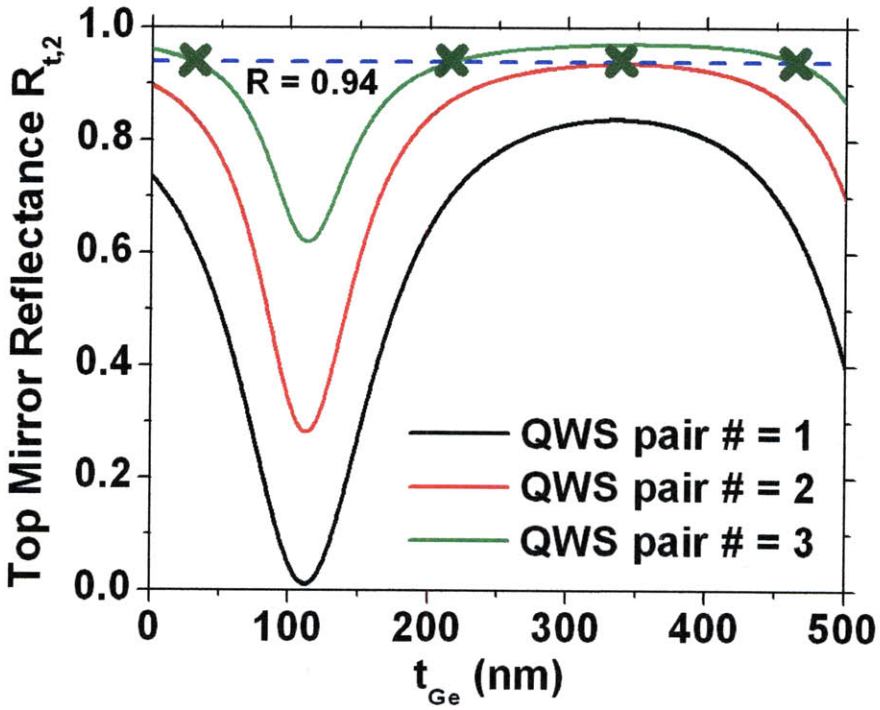

Figure 4.11 Solid curves: $R_{t,2}$ as a function of coupling-matching layer's thickness for different QWS pair numbers; dashed line: reflectance corresponding to the critical coupling condition Equation 4.1; green crosses: thickness values at which the critical coupling condition is met.

Figure 4.12 shows the QE spectra for the two PbTe absorbers. Peak quantum efficiencies over 80% have been realized in both wavebands with only 50 nm and 100 nm thick PbTe absorbers given the strong resonant cavity enhancement. In comparison, a conventional

free-space PbTe photodetector operating at 3.6 μm wavelength requires an absorber layer as thick as 10 μm. As a consequence, the generation-recombination and Johnson noise in our design will be 10 times lower, since both types of noises scale with the square root of the active material volume. The ripples between peaks (side lobes) can be suppressed by integrating a planar band-stop filter or employing an apodized cavity design[85].

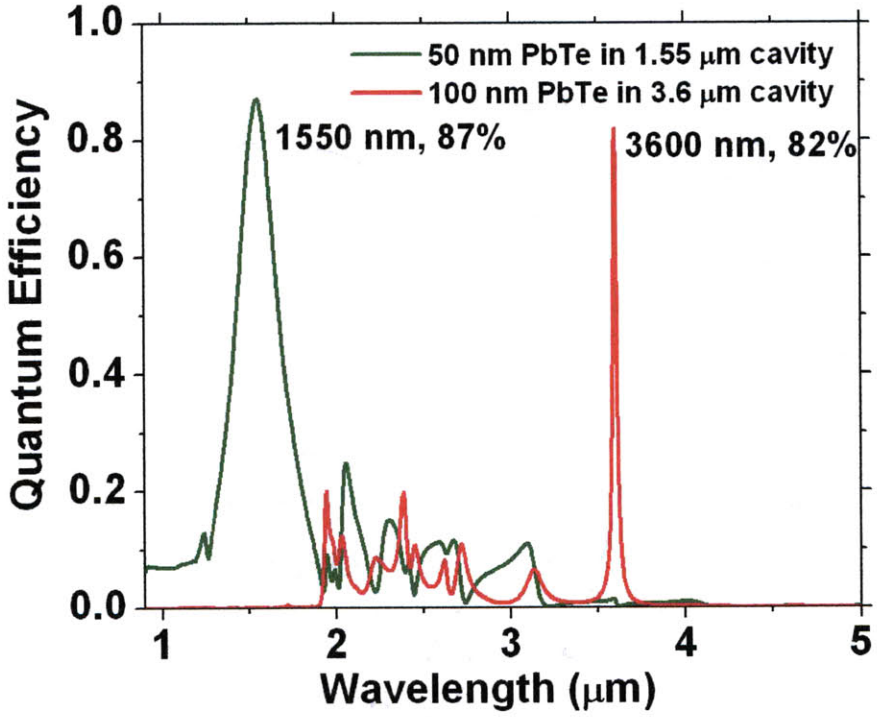

Figure 4.12 QE spectra calculated for two PbTe absorbers in the two cascaded resonant cavities, showing two detection bands peaked at 1.55 μm and 3.6 μm with high QE and low spectral cross talk.

Besides the high QE, the high degree of spatial localization of modes effectively minimizes cross talk between the two IR absorbing layers. Figure 4.13 plots the light intensity distributions in the stack at the two resonant wavelengths. Spectral cross talk in a dual wavelength detector can be measured using[86]:

$$Crosstalk = \frac{\eta_{active2}(\lambda_1)}{\eta_{active2}(\lambda_2)}, \lambda_1 < \lambda_2 \tag{4.12}$$

where $\eta_{active2}(\lambda_1)$ is the QE of second active layer at λ_1, and $\eta_{active2}(\lambda_2)$ is the peak QE of second active layer at λ_2. Our design leads to spectral cross talk as low as 0.1%, more than two orders of magnitude lower compared to a tandem design[86] or a single cavity design[80].

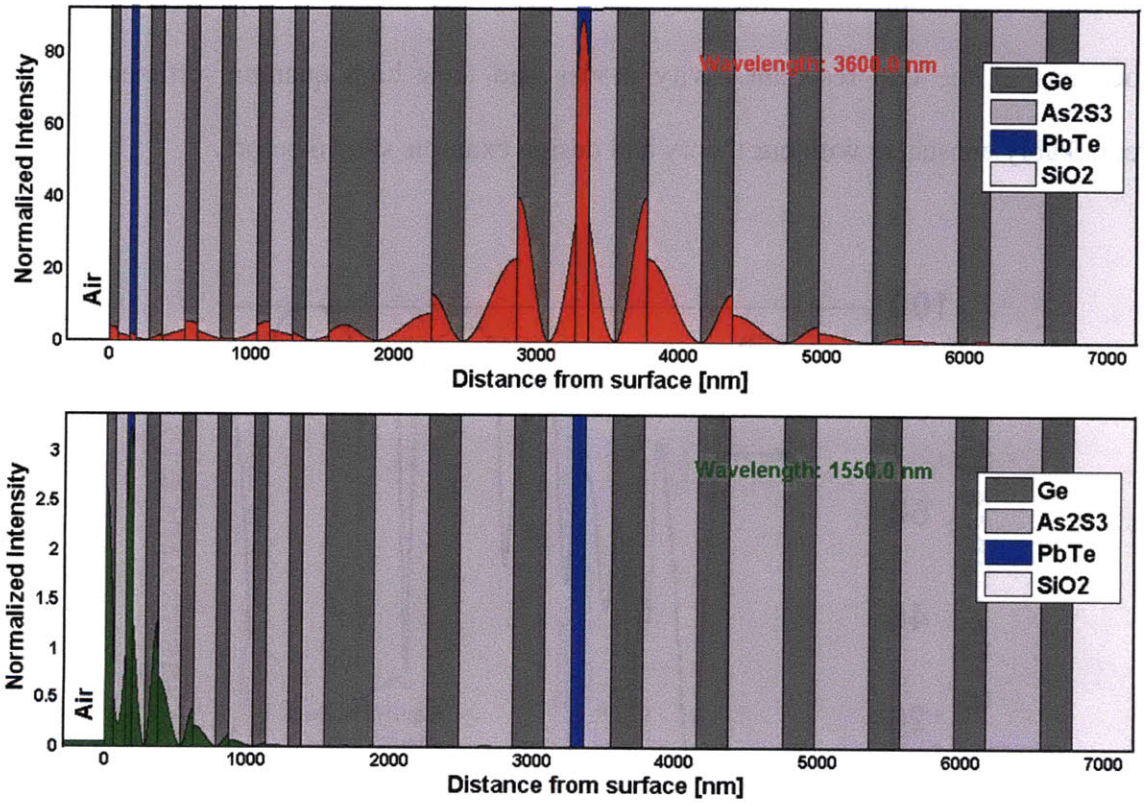

Figure 4.13 Normalized light intensity spatial distribution for 3.6 μm and 1.55 μm wavelengths, respectively, illustrating high degree of modal spatial localization.

4.2.4. Optical properties of dual waveband RCE photodetectors

According to precious design for dual waveband RCE photodetectors, the whole stack has been fabricated onto transparent CaF_2 substrate layer by layer and its optical properties are measured. Figure 4.14 shows the preliminary optical experimental results, i.e. reflectance and transmittance spectra of the dual waveband RCE photodetectors. Two resonant cavity modes are clearly identified in the reflectance spectrum, i.e. one at 1.61 μm and the other at 3.70 μm. Using the measured reflectance and transmittance values, we calculate peak quantum efficiency values to be 92% and 68% respectively. Both the locations of the two resonant cavity modes and their high quantum efficiencies are remarkably consistent with our theory and design example shown before.

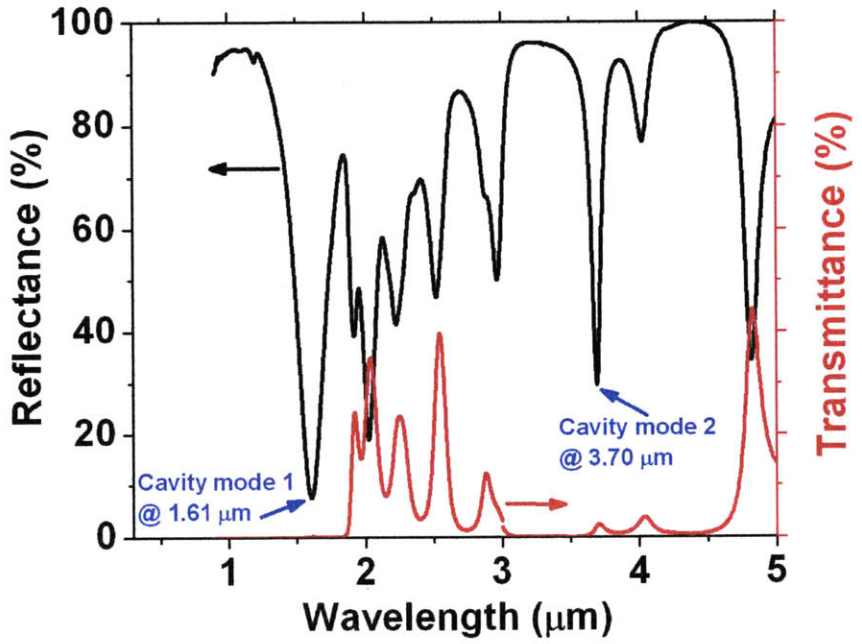

Figure 4.14 Reflectance and transmittance spectra of dual waveband RCE photodetector. Two resonant cavity modes are clearly seen in the reflectance spectrum, i.e. one at 1.61 μm and the other at 3.70 μm. Based on the measured reflectance and transmittance values, peak quantum efficiencies are calculated as 92% and 68% respectively.

4.3. Summary

In this chapter, we discuss the strategy to enhance the quantum efficiency of thin polycrystalline PbTe films, i.e. using cavity structures. Mid-IR distributed Bragg reflectors serving as mirror stacks are developed to form such cavity structures. Due to the excellent IR transparency, sputtered Ge and evaporated As_2S_3 films are chosen as high and low index materials to fabricate the DBR structures.

We propose and analyze a versatile and scalable design for cavity-enhanced photodetectors capable of sensing multiple wavebands simultaneously in a single pixel. The design is based on phase-tuned propagation in cascaded planar resonant cavities and this concept can be generalized to detect virtually any arbitrary number of wavelengths. Theoretical analysis indicates a coupling-matching layer with optimized thickness is necessary between adjacent cavities to achieve near unity quantum efficiencies at desired wavelength. A design example shows that the cross talk between two detected wavebands (1.55 μm and 3.6 μm) is negligible owing to the separation of the two bands in both wavelength and spatial domains. Even with very thin absorbers, quantum efficiencies over 80% can be obtained at both resonant wavelengths due to the strong resonant cavity enhancement. Preliminary optical experiments on the fabricated dual waveband RCE photodetector's stack demonstrate the existence of the two expected resonant cavity modes (1.61 μm and 3.70 μm). Peak quantum efficiency values as high as 92% and 68% have been achieved for these two wavebands respectively. This proposed photodetector

structure combines high QE, reduced detector noise as well as low spectral cross talk, and thus may find wide applications in security surveillance, imaging, and IR spectroscopy.

Chapter 5. Single waveband RCE photodetectors on a silicon platform for mid-IR[87,88]

In last chapter we discuss design of multiple waveband RCE photodetectors using cascaded resonant cavities. Actually, each resonant cavity serves as a building block for the whole structure and can be treated as a single waveband RCE photodetector. Thus in reality demonstration of such single waveband RCE photodetector is essential for the development of multiple waveband RCE photodetectors.

Single waveband RCE photodetectors for mid-IR have been demonstrated in single-crystalline PbTe[89], $Pb_{1-x}Eu_xSe$[90], and HgCdTe[91]. Our approach, which uses polycrystalline and amorphous materials for cavity fabrication, not only enables simultaneous multispectral detection within a single RCE detector, but also reduces the cost and allows monolithic integration with Si readout integrated circuits (Si ROIC). In this chapter we present a demonstration of mid-IR RCE detectors monolithically integrated on silicon using polycrystalline PbTe as the IR active material. The entire detector structure can be directly deposited onto a silicon substrate free of lattice match constraints. While it was previously believed that high-temperature sensitization is required for polycrystalline lead chalcogenide films to become IR sensitive[21,22,31], our polycrystalline PbTe films show excellent IR response through a room-temperature oxygen sensitization process as we have discussed in chapter 3. As low temperature processing (150 °C) is implemented in the entire fabrication process, our detector is promising for monolithic integration with Si ROIC.

5.1. Design using critical coupling condition

Quantum efficiency in this work is defined in the same way as before, which is the ratio of the number of photon generated excess electron-hole pairs over the number of incident photons, and will be denoted as QE. Due to the fact that PbTe is direct band gap semiconductor, we have made the assumption that all absorbed photons contribute to generating electron-hole pairs. The key design challenge for RCE detectors is how to attain critical coupling, the prerequisite of achieving near unity quantum efficiency as we have discussed in chapter 4.

In a planar cavity sandwiched between two mirrors, the critical coupling condition can be generically written as:

$$Q_{tm} = Q_{abs} \text{ and } Q_{bm} \to \infty \left(\text{i.e. } R_{bm} \to 1\right) \tag{5.1}$$

where Q_{tm}, Q_{bm}, and Q_{abs} represent the cavity quality factors (Q) due to top mirror loss, bottom mirror loss, and absorption of the IR active layer, and R_{bm} is the bottom mirror reflectance. One may notice critical coupling condition formulated by Equation 5.1 has different expression from Equation 4.1. Actually Equation 4.1 is applicable for the case when the light absorbing material fills the whole cavity region, while Equation 5.1 is a general formula describing critical coupling condition though it seems less explicit. As a reminder, a thin active layer contributes to enhanced signal-to-noise ratio, thus one important subtlety with our multi-layer cavity is that the active absorbing material (PbTe) does not fill the entire region between the two DBR mirrors. Therefore we resort to a general formulation Equation 5.1 applicable to a "sandwiched" cavity configuration (Figure 5.1).

In this case, the interfaces between the two As_2S_3 spacer layers and the PbTe layer sandwiched between them cause additional reflections which complicates the cavity optical response. Therefore, the apparent mirror reflectance values calculated using TMM is not directly correlated with the cavity Q factor, and Equation 4.1 is an approximation for Equation 5.1. In other words, the Q factor now cannot be calculated simply using the mirror reflectance values, and the Q factor is a much better representation of the cavity property.

When the IR active material completely fills the cavity, Equation 5.1 still can be reduced to Unlu's formulation[83]. Perturbation theory gives Q_{abs} as[82]:

$$Q_{abs} = \frac{4\pi}{\lambda n\alpha} \frac{\int_{stack} dr\varepsilon_c |E_0|^2}{\int_{active} dr |E_0|^2} \approx \frac{4\pi}{\lambda n\alpha d} \frac{\int_{stack} dr\varepsilon_c |E_0|^2}{|E_{0,active}|^2} \tag{5.2}$$

where n, α and d are the index of refraction, absorption coefficient and thickness of the IR active material, λ is the resonant wavelength, E_0 denotes the electric field distribution of the resonant mode, and ε_c gives the relative dielectric constant profile of the stack. The second equality in Equation 5.2 holds when $\lambda >> d$, in which case the electric field can be treated as a constant in the IR active layer ($E_{0,active}$). Since Q_{tm} is determined by the top mirror reflectance R_{tm}, similar to Equation 4.1, Equation 5.1 also states that given a bottom mirror with near unity reflectance ($R_{bm} \rightarrow 1$), maximum QE at resonant wavelength may be obtained by appropriately choosing a top mirror reflectance to satisfy Equation 5.1.

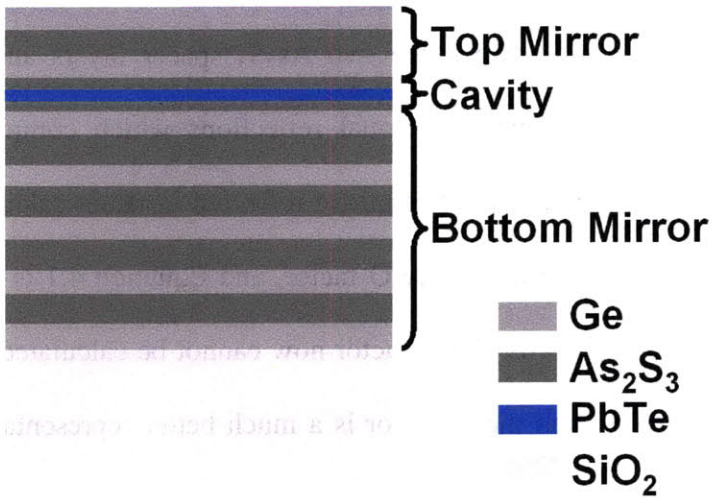

Figure 5.1 Schematic cross-sectional picture of the designed resonant cavity structure. In the cavity region, two As_2S_3 spacer layers sandwich the PbTe IR absorbing layer.

To illustrate the principle of critical coupling, Figure 5.2 plots quantum efficiency in an RCE detector as a function of Q_{tm} given $R_{bm} \rightarrow 1$. The Q_{abs} value of the designed RCE detector structure is derived to be 85 using Equation 5.2 and fixed as a constant in the calculation. The calculation employs a modified two-port coupling matrix approach[92]. Clearly, unity QE is attained only when $Q_{tm} = Q_{abs}$, in agreement with the condition specified by Equation 5.1.

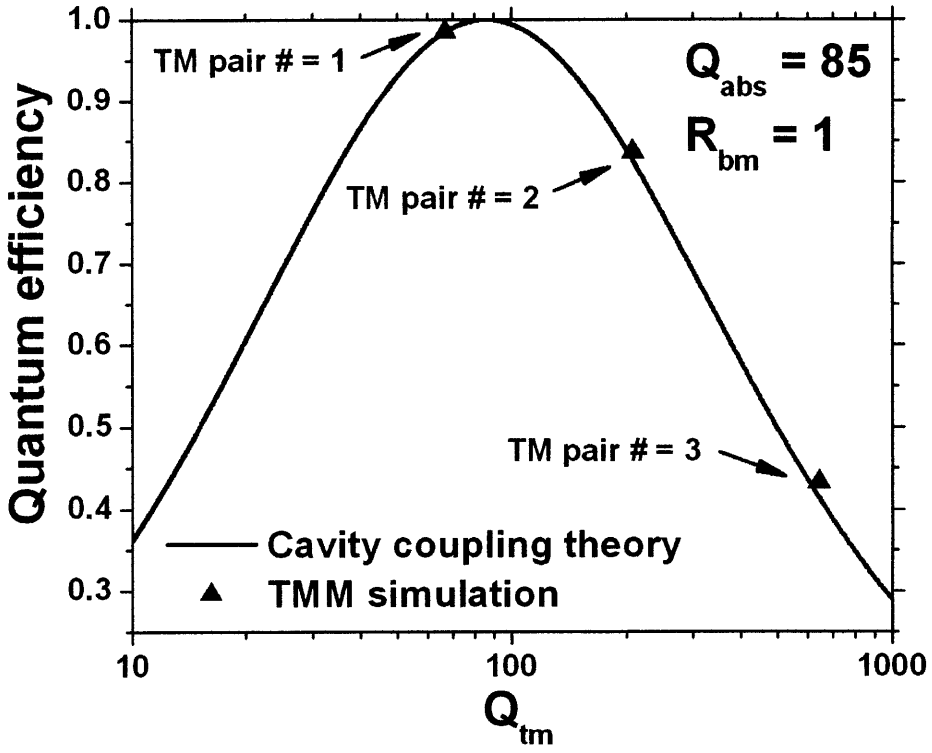

Figure 5.2 QE of RCE detector plotted as a function of Q_{tm} calculated using a modified coupling matrix method; the triangles correspond to TMM simulated QE values of designs with different top mirror (TM) Bragg pair numbers. Near unity QE is attained under critical coupling condition, i.e. $Q_{tm} = Q_{abs}$.

To experimentally demonstrate near unity QE, we tune the top mirror reflectance and Q_{tm} by using a top mirror consisting of an appropriate number of Bragg pairs to satisfy Equation 5.1. As_2S_3 and Ge are used as the Bragg mirror materials given their IR transparency. Their wavelength-dependent refractive indices are calculated from experimentally measured transmittance spectra using the Swanepoel approach[43]. Refractive indices of As_2S_3 and Ge used to calculate the Bragg pairs are 2.363 and 4.105 respectively around 3.5 μm wavelength. The refractive indices of PbTe IR absorber are measured using IR ellipsometry as shown in chapter 1. Using the experimentally measured indices as input and a 100 nm thick PbTe layer as the IR active material, QE of

RCE detector designs with different top mirror As_2S_3-Ge Bragg pair numbers may be simulated using the transfer matrix method (TMM). The TMM simulated QE values are represented in Figure 5.2 as the triangles; the excellent agreement between the modified coupling matrix theory and TMM confirms that the coupling matrix method conventionally employed for micro-ring resonator simulations may also be applied for quantitative prediction of QE in RCE detectors.

5.2. Multi-step lift-off fabrication process

All films are deposited in the same chamber. 2" diameter poly-Ge of 99.999% purity is used as sputtering target, As_2S_3 bulk and PbTe bulk of 99.999% purity are used as the source material for thermal evaporation. Both sputtering and thermal evaporation are carried out at a base pressure of 5×10^{-7} Torr. Optically polished CaF_2 discs and oxide coated Si wafers are used as starting substrates. The substrates are held on a rotating substrate holder, at room temperature, throughout the depositions. Film deposition rate is monitored in real-time through a quartz crystal sensor and is maintained at 1.3 Å/s for Ge, and ~10 Å/s for As_2S_3 and PbTe.

Photodetectors are fabricated by a three-step lift-off process. The alignment is done manually using a mask aligner with a 350 W Hg bulb. Negative photoresist is exposed to 320 nm UV light and developed to make openings for film deposition, which is followed by lift-off process in an ultrasonic bath. Three lift-off steps are used to pattern the bottom mirror and PbTe, top mirror, and Sn contacts separately, as shown in Figure 5.3. Key process steps and corresponding recipe for each step are summarized in Table 5.1. To

demonstrate the success of the fabrication process, Figure 5.4 shows an 8 × 8 array of the photodetectors after the first lift-off step and a fabricated RCE photodetector (30 μm × 30 μm in size).

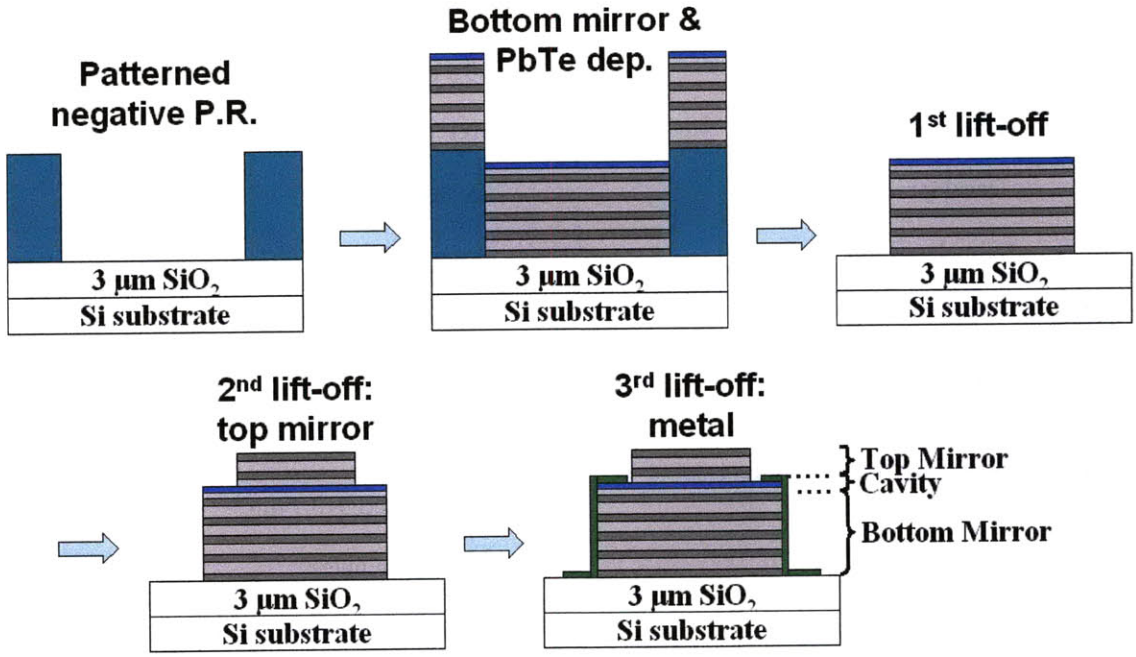

Figure 5.3 Three-step lift-off process for single waveband RCE photodetector fabrication. Three lift-off steps are used to pattern the bottom DBR mirror and PbTe, top DBR mirror, and Sn contacts separately.

Figure 5.5 (a) shows the cross-sectional SEM image of the resonant cavity structure deposited onto a SiO_2/Si substrate, and for comparison, Figure 5.5 (b) shows a schematic picture of the designed RCE detector structure. All fifteen layers are clearly identified in the SEM image, illustrating good film thickness control and uniformity. Sharp interfaces between different layers indicate negligible material inter-diffusion occurs since processing temperatures are low (150 °C).

Table 5.1. Key process steps and detailed recipe for single waveband RCE photodetector fabrication.

Step #	Process step	Process recipe/purpose
1	Pre-bake substrates to get rid of moisture	150 °C/15 minutes
2	Spin coat photoresist NR71-3000PY	20 s + 40 s (0 to 2500 rpm, 2500 rpm), for photoresist 3.3~3.7 μm
3	Pre-exposure bake	150 °C/2 minutes
4	Exposure	60 s by Broadband (EML)
5	Post-exposure bake	100 °C/2 minutes
6	Development	25~30 s in RD6
7	Film deposition	Bottom DBR and PbTe
8	First lift-off	~25 minutes in Acetone ultrasonic bath
9	Pre-bake substrates to get rid of moisture	120 °C/15 minutes
10	Spin coat photoresist NR71-3000PY	20 s + 40 s (0 to 2500 rpm, 2500 rpm), for photoresist 3.5~3.7 μm
11	Pre-exposure bake	150 °C/2 minutes
12	Exposure	60 s by Broadband (EML)
13	Post-exposure bake	100 °C/2 minutes
14	Development	30 s in RD6
15	Film deposition	Top DBR
16	Second lift-off	~14 minutes in Acetone ultrasonic bath
17	Pre-bake substrates to get rid of moisture	120 °C/15 minutes
18	Spin coat photoresist NR9-1000PY	10 s + 5 s + 35 s (750 rpm, 750 to 1600 rpm, 1600 rpm), for photoresist >1 μm
19	Pre-exposure bake	150 °C/80 s
20	Exposure	40 s by Broadband (EML)
21	Post-exposure bake	100 °C/80 s
22	Development	8 s in RD6

Table 5.1. (Continued) Key process steps and detailed recipe for single waveband RCE photodetector fabrication.

23	Metal deposition	200 nm Sn by e-beam evaporation (EML): X = 0; Y = 0; SX = 0.25; SY = 0.2; $<5.3 \times 10^{-5}$ Torr; 0.125 A; 1.5~2.0 Å/s; 15 minutes active cooling after 100 nm
24	Third lift-off	~1 minutes in Acetone ultrasonic bath

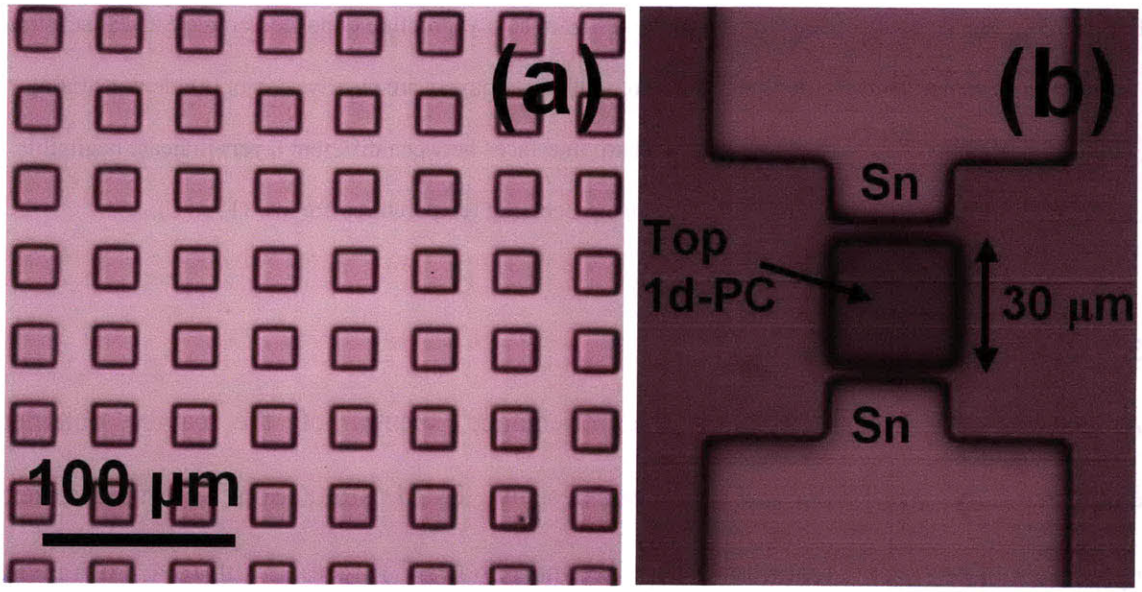

Figure 5.4 Pictures taken by an optical microscope: (a) an 8 × 8 array of the photodetectors after the first lift-off step; (b) one 30 μm × 30 μm fabricated photodetector.

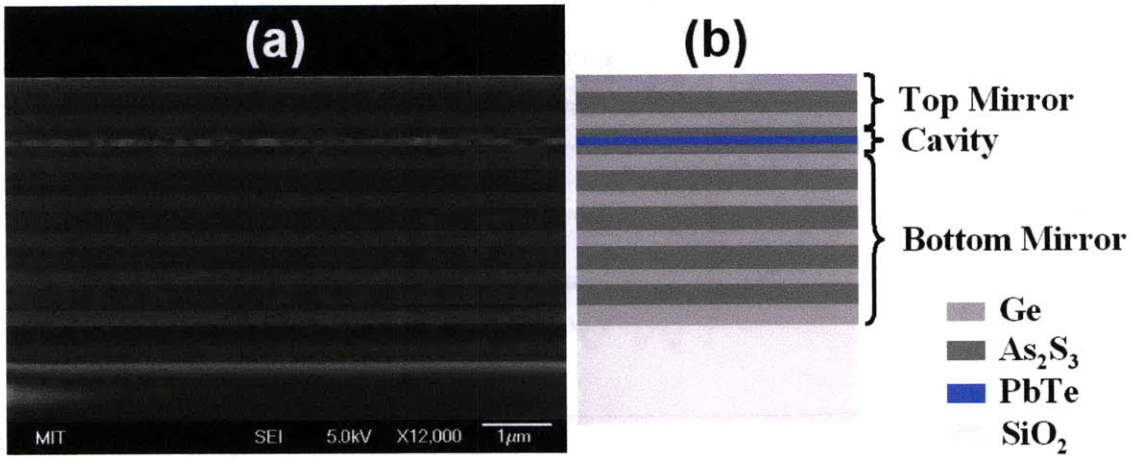

Figure 5.5 (a) SEM cross-sectional image of the resonant cavity structure deposited onto a SiO_2/Si substrate. (b) Schematic picture of the designed structure. All fifteen layers are clearly seen in (a), demonstrating good film thickness control and uniformity. Sharp interfaces between different layers indicate negligible material inter-diffusion occurs since processing temperatures are low (150 °C).

5.3. Optical characterization

A comparison (Figure 5.6) of the reflectance spectra of the cavity obtained experimentally by FTIR and theoretically by TMM simulation shows excellent agreement. The spectra feature a photonic band gap (PBG) from 2.5 μm to 4.5 μm and a resonant cavity mode at 3.5 μm, as designed. Figure 5.6 shows only first order cavity mode since here we use a half wavelength cavity and thus it does not support higher order cavity modes. At the resonant wavelength of 3.5 μm, directly measured reflectance and transmittance values are 6.6% and 3.5% respectively, indicating a quantum efficiency of 90%. Full width at half maximum (FWHM) is 92.53 nm, corresponding to a quality factor of 38, in good agreement with the simulated value of 43 ($=0.5Q_{abs}$).

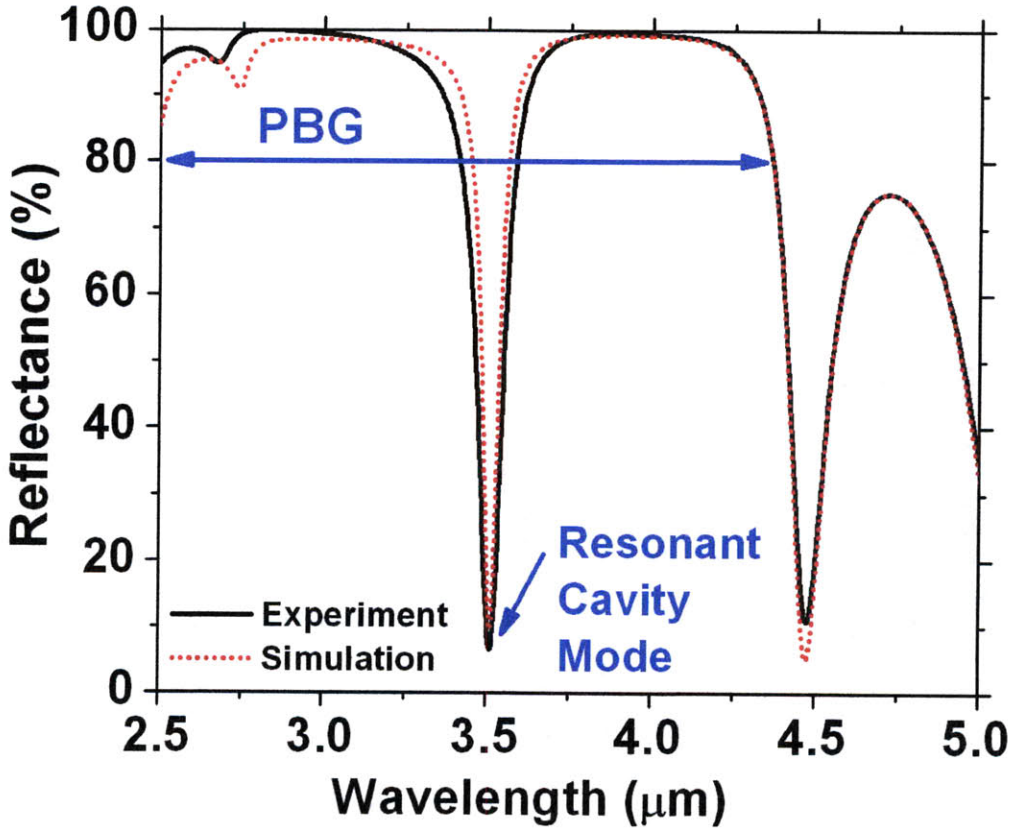

Figure 5.6 Reflectance spectra of the cavity structure obtained by FTIR measurement (solid line) and TMM simulation (dotted line), showing excellent agreement. The spectra feature a PBG from 2.5 μm to 4.5 μm and a resonant cavity mode at 3.5 μm as designed.

Figure 5.7 presents a comparison of two cavity structures with different top mirror (TM) Bragg pair numbers. It illustrates the deviation from the critical coupling condition due to highly reflective top mirror with two Bragg pairs. When the top mirror has one Bragg pair, the cavity is closer to the critical coupling condition than the case of two Bragg pairs, which is indicated by two reflectance values at resonant wavelength of 3.5 μm (6.6% for one Bragg pair vs. 33.9% for two Bragg pairs). This experimental result is consistent with the design curve shown in Figure 5.2.

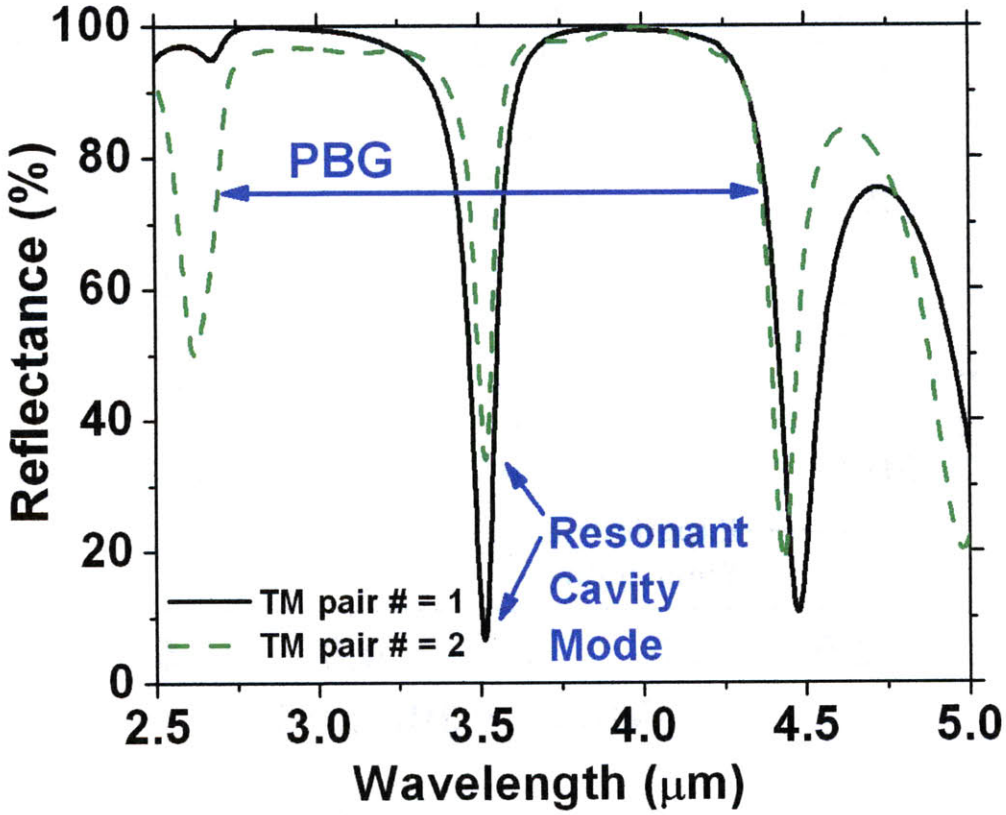

Figure 5.7 Reflectance spectra of two cavity structures with different top mirror (TM) Bragg pair numbers. Both curves are obtained by FTIR measurement. Solid line: TM Bragg pair number is 1; dashed line: TM Bragg pair number is 2.

5.4. Photoconductivity experiment

Unlike single layer films, there are more challenges to measure photoconductivity of RCE photodetectors due to the requirement of high resolution. According to Figure 5.6, FWHM is 92.53 nm for the cavity structure, thus the resolution of the photoconductivity experiment should be smaller than 92.53 nm. In our previous photoconductivity study on single layer PbTe films, sodium chloride prism is used to disperse IR light providing a resolution of ~500 nm. This will lead to very coarse IR light dispersing and cannot offer

fine enough resolution for RCE photodetectors. Therefore, we have developed a new measurement system for high-resolution IR photoconductivity experiment as shown in Figure 5.8.

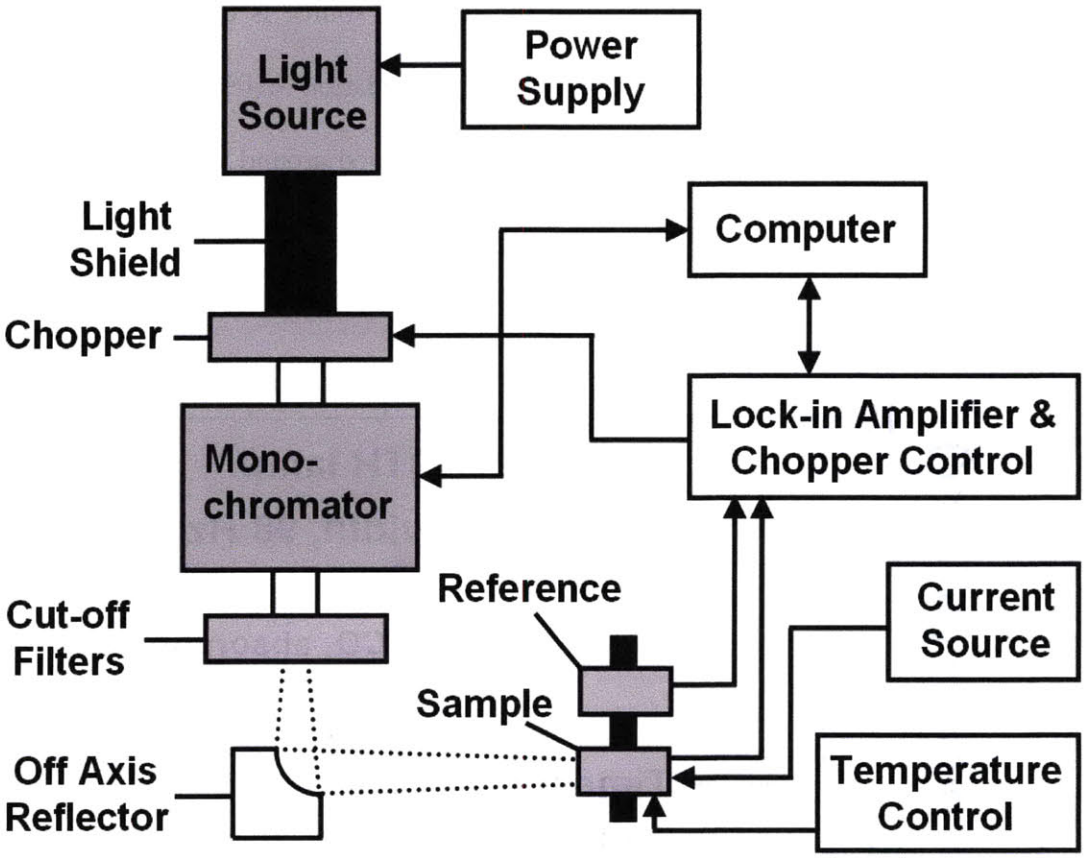

Figure 5.8 Schematic layout of high-resolution IR photoconductivity measurement system.

Light from a 100 W quartz tungsten halogen (QTH) lamp is modulated at 98.0 Hz and monochromatized by a Newport Oriel MS257 monochromator. Long-pass optical filters are used to block higher order diffracted light. A pyroelectric detector with known photo-responsivity is used as a reference detector to obtain the power density of light incident onto the samples. A thermoelectric cooler (TEC) is used to cool down samples and a

Keithley 6220 current source is used to provide bias current. The wavelength resolution is ~45 nm in mid-IR using 2 mm slit width for both entrance and exit slits attached to the monochromator. Output optical power density is recorded by the standard pyroelectric detector each time during photoconductivity measurement. Curves taken at four different times are shown in Figure 5.9. Stability of the IR light source is demonstrated by the highly repeatable measured output power density (deviation <10%). Given the high resolution of the system, CO_2 absorption is clearly resolved around 4.2 μm as shown in Figure 5.9.

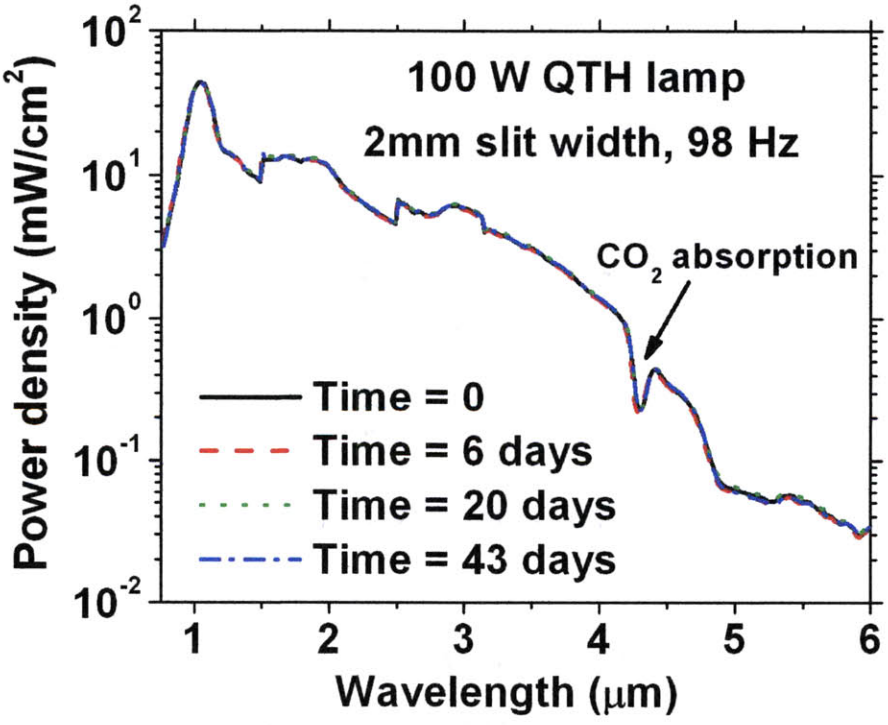

Figure 5.9 Output optical power density of the IR photoconductivity measurement system. Curves are recorded by a standard pyroelectric detector at four different times. Deviation is smaller than 10%.

Room temperature Hall measurement shows p-type conduction in the PbTe absorbing layer with a Hall mobility of 99 $cm^2V^{-1}s^{-1}$ and a carrier concentration of 4.1×10^{16} cm^{-3}. This is consistent with our PbTe plain film results in chapter 3 and indicates no film quality degradation has occurred during the photodetector fabrication. Figure 5.10 demonstrates the operation of the polycrystalline PbTe based RCE photodetector with a dimension of 1200 μm × 1200 μm. In the photoconductivity measurement samples are biased under fixed current (0.1 mA) and cooled by TEC (-56 °C), and the photovoltage caused by the IR light illumination is recorded. Photon incident flux and spectral shape are obtained from the pyroelectric reference detector with known area and responsivity. The inserted picture on the right shows the electric circuit used. Peak responsivity of 100 V/W is measured at the resonant wavelength of 3.45 μm. The small discrepancy (< 2%) of the resonant wavelength location between Figure 5.6 and Figure 5.10 is due to non-normal incidence of light in both experiments. To quantify the resonant cavity enhancement effect, PbTe plain film photodetector of the same thickness and dimensions has been measured under the same conditions as shown in Figure 5.10. 100 nm thick PbTe plain film shows much lower photoresponse (< 10 V/W) in mid-IR range due to very weak light absorption, while PbTe in the cavity shows 13.4 times higher responsivity at the designed resonant wavelength.

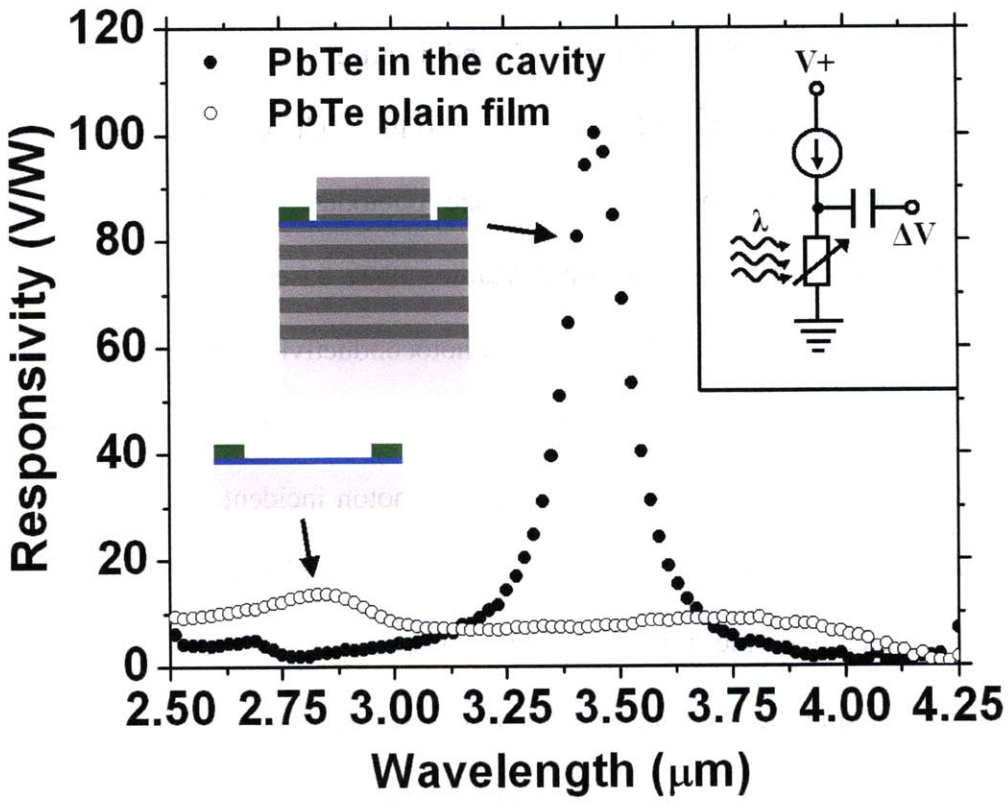

Figure 5.10 Responsivity spectra of the 100 nm PbTe thin film photodetector within the cavity (filled circles) and without cavity (plain film only, open circles) with 0.1 mA bias current at -56 °C (sample dimension is 1200 μm × 1200 μm). The two inserted pictures on the left show the tested device structures schematically after metal deposition and patterning (green colored regions). The inserted picture on the right shows the electric circuit employed in the photoconductivity measurement. Plain film shows much lower photoresponse (< 10 V/W) in mid-IR range due to very weak light absorption, while PbTe in the cavity shows 13.4 times higher responsivity at the designed resonant wavelength.

Figure 5.11 shows the photoconductivity experiment results for a 400 μm × 400 μm RCE photodetector. Compared with the result of a 1200 μm × 1200 μm RCE photodetector in Figure 5.10, smaller size photodetector shows responsivity about one order of magnitude higher than larger size photodetector. This is consistent with our previous discussion on

responsivity in chapter 3. Equation 5.3 (same as Equation 3.5) predicts responsivity's size dependence as follows:

$$\Re = \frac{\mathrm{IQE}\tau(1+b)\lambda}{hcew^2d^2p^2\mu_p} \propto \frac{1}{w^2} \tag{5.3}$$

where w is the width of the photodetector, I is the bias current, τ is carrier lifetime, b is the mobility ratio (μ_e/μ_p), λ is wavelength, QE is the quantum efficiency, d is thickness of the photoactive layer, p is holes' concentration, μ_p is holes' mobility, and h, c, and e are Plank constant, speed of light in vacuum, and elementary charge respectively. Furthermore, Figure 5.11 (a) indicates peak responsivity of the RCE photodetector increases with bias current, and they obey a linear relationship which is shown more clearly in Figure 5.11 (b). Again, this result agrees quite well with Equation 5.3.

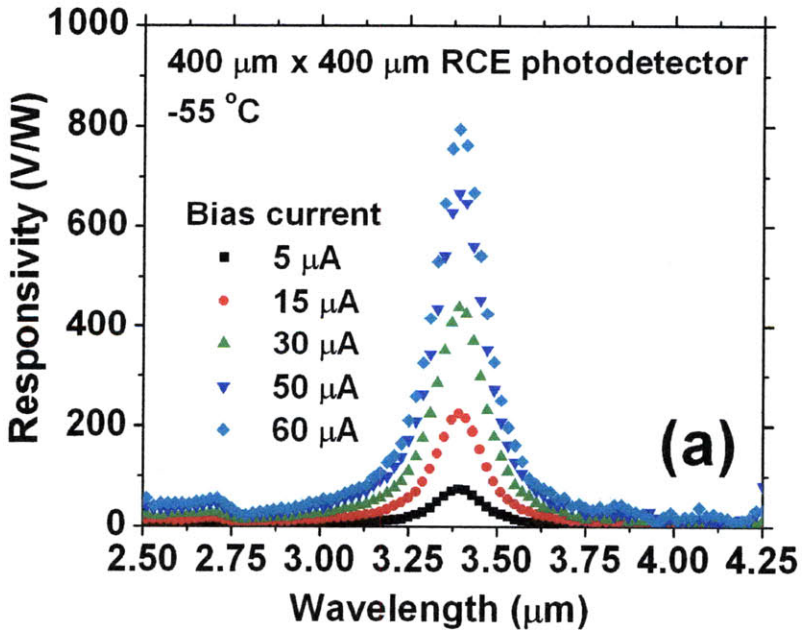

Figure 5.11 (a) Responsivity spectra of the 400 μm × 400 μm RCE photodetector with 100 nm PbTe thin film in the cavity. The results are obtained at -55 °C and under different bias currents.

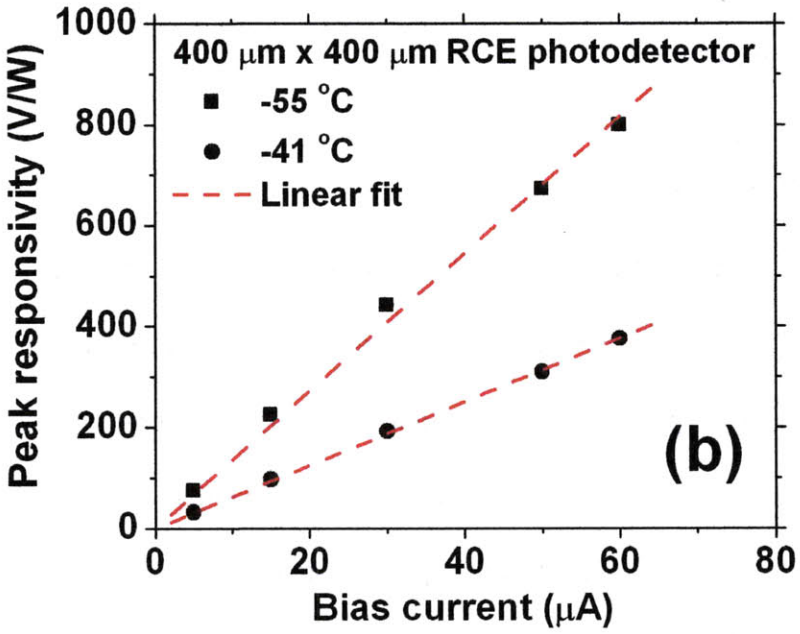

Figure 5.11 (Continued) (b) Linear dependence of peak responsivity on the bias current at -55 °C and -41 °C. The result is consistent with Equation 5.3.

5.5. Detectivity and power consumption

As we have discussed in chapter 3, Johnson noise is the intrinsic dominant noise for our polycrystalline PbTe photodetectors. With the measured resistance values of the RCE photodetectors (R_d), Johnson noise voltage can be calculated by:

$$v_{nJ} = \sqrt{4kTR_d\Delta f} \tag{5.4}$$

where k is the Boltzmann constant, T is absolute temperature, and Δf is the effective noise bandwidth. And Johnson-noise-limited detectivity is given by:

$$D^* = \frac{\Re\sqrt{A_d\Delta f}}{v_{nJ}} \tag{5.5}$$

where $\Re$ is the responsivity of the photodetector, A_d is the area of the photodetector, Δf is the effective noise bandwidth, and v_{nJ} is Johnson noise voltage. Thus with

experimentally measured responsivity $\Re$ and resistance R, one can measure Johnson-noise-limited detectivity according to Equation 5.5.

On the other hand, plugging Equations 5.3 and 5.4 into Equation 5.5, Johnson-noise-limited detectivity can be expressed explicitly as follows:

$$D^* = \frac{I(1+b)\tau\lambda \mathrm{QE}}{hcw\sqrt{4kTed^3p^3\mu_p}} \tag{5.6}$$

Notably, even though detectivity is typically independent of detector size when the device operates in the photovoltaic mode, Equation 5.6 suggests Johnson-noise-limited detectivity in a photoconductive detector is inversely proportional to the linear dimension of the photodetector. Thus higher detectivity values can be expected for photodetectors with smaller size. To demonstrate this mechanism, RCE photodetectors of different sizes (100~1200 μm) are tested under the same bias current of 50 μA. Their peak detectivity values measured according to Equation 5.5 are shown as solid squares in Figure 5.12. With the known dependence of detectivity on w as described in Equation 5.6, the measured data is fitted according to Equation 5.6. Excellent agreement between theoretical fit based on Equation 5.6 and experimental data can be seen in Figure 5.12. Detectivity value up to 0.72×10^9 $\mathrm{cmHz^{1/2}W^{-1}}$ is obtained in a 100 μm wide RCE photodetector while photoactive layer's thickness is only 100 nm, comparable with commercial polycrystalline mid-IR photodetectors fabricated via chemical bath deposition[93]. Further reduction of photodetector size will lead to higher detectivity value ($\sim10^{10}$ $\mathrm{cmHz^{1/2}W^{-1}}$) as is predicted by Equation 5.6.

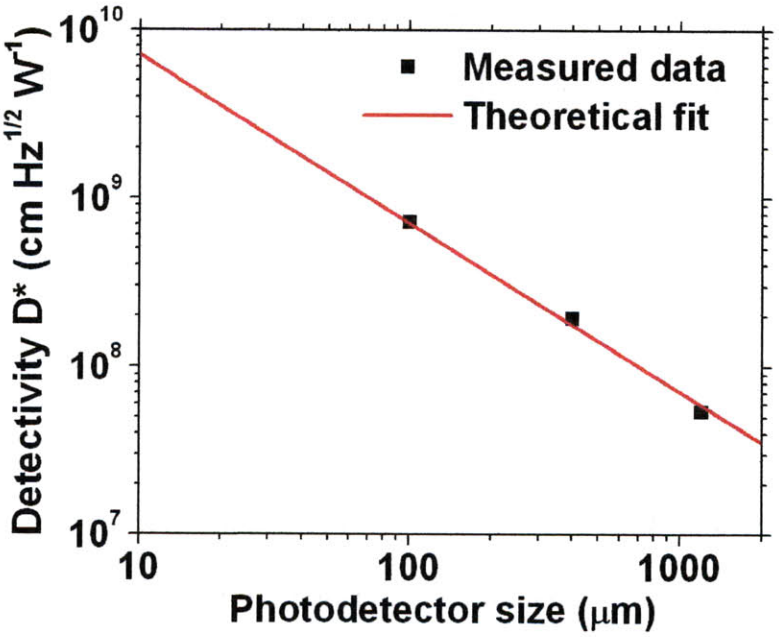

Figure 5.12 Detectivity D^* as a function of photodetector size with square shape. Theoretically fitted curve is based on Equation 5.6 showing the inversely proportional relationship between D* and photodetector size. Solid squares correspond to experimentally measured data.

Based on the experimental data in Figure 5.12 and Equation 5.6, Johnson-noise-limited detectivity values at different bias current levels can be calculated, as shown in Figure 5.13. Even though Equation 5.6 predicts detectivity increases with bias current obeying a linear relationship without limitation, in reality this trend will stop at certain bias current level due to the Joule heating effect and the increase of related current noise. This is determined by the cooling capability of the thermoelectric cooler (TEC) and the heat sink underneath taking out the heat generated during photodetector's operation. With known photodetector's resistance value R and bias current I, the power consumption or the heat generated can be calculated by:

$$P = I^2R \tag{5.7}$$

As shown in Figure 5.13, with 100 μA bias current, power consumption of one photodetector is 9.7 mW. For a focal plane array (FPA) with 8 × 8 photodetectors, the power consumption is less than 1 W, which is in the acceptable range. However, for FPA with over one million photodetectors, this will result in a power consumption level of 10 kW which is totally unacceptable (~20 kW for FPA of dual waveband RCE photodetectors). So as shown in Figure 5.14, a trade-off has to be made between the desired detectivity value and the power consumption budget and heat dissipation strategy. This will be determined by the real application needs, Si ROIC specifications, TEC's cooling capability, and specially designed heat sink for faster heat dissipation.

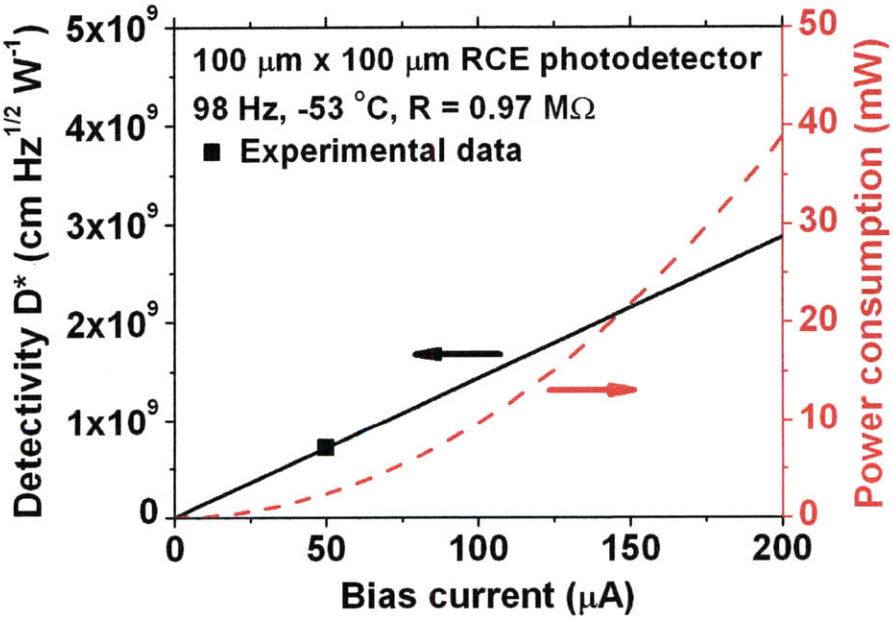

Figure 5.13 RCE photodetector's detectivity and power consumption as a function of bias current.

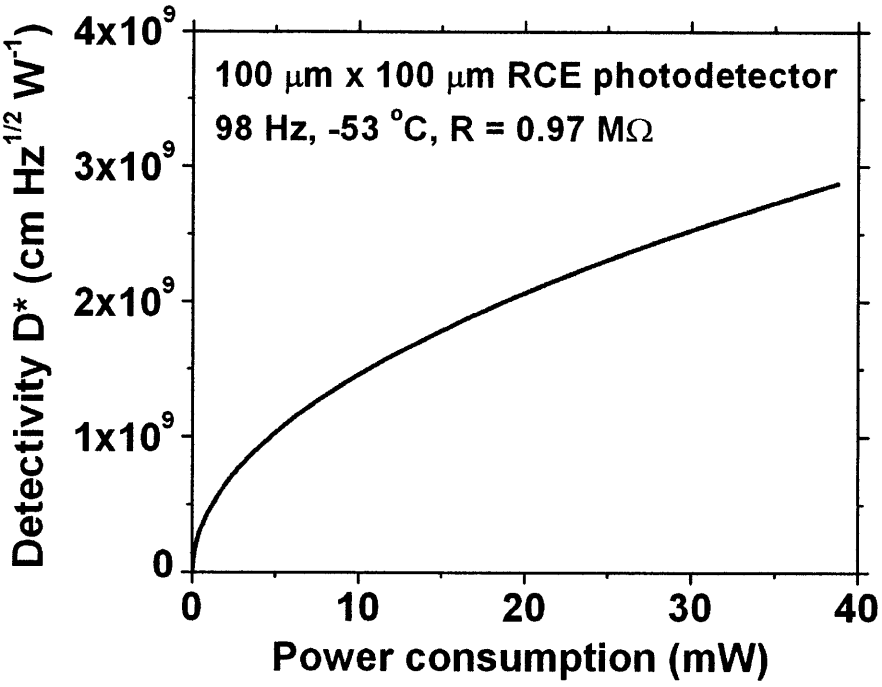

Figure 5.14 RCE photodetector's detectivity as a function of power consumption.

5.6. Summary

In this chapter, we present a demonstration of fully functional single waveband RCE mid-IR photodetectors on a silicon platform. Single waveband RCE photodetectors can serve as building blocks for multiple waveband RCE photodetectors, so this step is essential for the development of multispectral photodetectors.

We design our RCE photodetectors to work under critical coupling condition, and we have developed multi-step lift-off process to fabricate such RCE photodetectors monolithically on a silicon platform. High quality photoconductive polycrystalline PbTe film is thermally evaporated, oxygen-sensitized at room temperature and acts as the infrared absorber. The cavity-enhanced detector operates in the critical coupling regime

and shows high quantum efficiency (90%). With an improved high-resolution photoconductivity measurement system, we successfully resolve the resonant cavity peak in the responsivity spectra. In a 1200 μm × 1200 μm RCE photodetector, we demonstrate a peak responsivity of 100 V/W at the resonant wavelength of 3.5 μm, 13.4 times higher compared to blanket PbTe film of the same thickness (100 nm). Both responsivity and detectivity are demonstrated to have dimension dependence and higher performance can be achieved in smaller size photodetectors. Detectivity as high as 0.72×10^{9} $cmHz^{1/2}W^{-1}$ has been measured in a 100 μm × 100 μm RCE photodetector, comparable with commercial polycrystalline mid-IR photodetectors. As low temperature processing (150 °C) is implemented in the entire fabrication process, this demonstration shows promise for monolithic integration of RCE photodetectors with Si readout integrated circuits (Si ROIC).

Chapter 6. Integration of single waveband RCE photodetectors and silicon readout integrated circuits (Si ROIC)

Based on the successful demonstration of mid-IR RCE photodetectors in last chapter, for the first time, two integration strategies for such single waveband RCE photodetectors and Si ROIC chips are evaluated in this chapter*. The first strategy adopts a hybrid structure of "wire-bonded" chips of separate RCE photodetectors and Si ROIC: photodetectors and Si ROIC chips are fabricated on different Si substrates and electrical connection between them is realized by ultrasonic wire bonding and wire soldering. The second one is monolithic integration of photodetectors and Si ROIC: single waveband RCE photodetectors are fabricated onto Si ROIC chips directly by three-step lift-off process developed previously. One prominent advantage of the integration is that we could simplify the whole system by incorporating more functions in the Si ROIC chip, e.g. changing from the heavy and bulky external mechanical chopper to on-chip "Electronic Chopper" realized by novel Si ROIC design.

6.1. Si ROIC design

According to previously obtained PbTe material properties and single waveband RCE photodetector's performance, Si ROIC is designed considering following parameters summarized in Table 6.1.

---

* Work shown in this chapter is from our collaboration with Nanyang Technological University (NTU) in Singapore. Customized Si ROIC chips are designed and provided by NTU. Fabrication of RCE photodetectors and monolithic integration of photodetectors and Si ROIC are done by us. All the test work on integrated devices is also achieved through our collaboration with NTU.

Table 6.1 Design parameters for single waveband RCE photodetectors and Si ROIC integration

Design Parameters	Values
Mid-IR wavelength	3.6 μm
Temperature of operation	-60 °C (-40 °C)
RCE photodetector dimension	100 μm × 100 μm
Cell dimension	150 μm × 150 μm
PbTe IR absorbing layer thickness	100 nm
Photoconductor resistance	500 kΩ (280 kΩ)
Bias current	0.1 mA
Optical modulation frequency	1 kHz
Maximum responsivity	1.36×10^5 V/W
Maximum incident light power density	2.56 mW/cm^2
Maximum photovoltage signal	34.8 mV
Johnson noise	122 nV (81 nV)
Maximum Johnson-noise-limited D*	1.4×10^{10} (2.8×10^9) cm·Hz$^{1/2}$/W

Unlike photodiodes, photoconductive devices require a larger bias current to establish an electric field that drifts the photo-generated carriers, and normally the bias current is much higher than the photocurrent. In general, for discrete IR photoconductive devices, to detect a small photo-signal embedded in a much higher total current and also to suppress noise, incident light beam is usually modulated by an external mechanical chopper and a lock-in amplifier is used to extract the photo-signal (Figure 5.8). To avoid using an external mechanical chopper in an integrated device, an "Electronic Chopping" concept using analog circuits on a Si ROIC has been proposed by Professor Joseph Chang's group at NTU. Based on this idea, we have designed and constructed a hybrid

PC-board prototype, and demonstrated the "electronic chopper". Therefore on-chip electronic chopping has been shown as a feasible alternative to off-chip optical modulation.

Figure 6.1 (a) illustrates the concept of "Electronic Chopping" schematically. Two un-illuminated adjacent photodetectors show identical electrical properties such as resistance and bias current. Under illumination, however, a differential signal can be obtained between these two neighboring photodetectors when one (reference) is shadowed from the incident IR light by a metal layer while the other (working) is exposed. A switch controlled by the electronic circuit then samples voltages from each of these two photodetectors at a chosen frequency, and the voltage difference between the two is the output. In dark space the output is zero since the two photodetectors are identical, and under illumination the output is a function of the wavelength of the incident light, i.e. responsivity spectrum of the working photodetector. Using this strategy, optical modulation by an external mechanical chopper can be mimicked by an on-chip "Electronic Chopper". The conditions for optimal electronic chopping are determined by: resistance matching between reference and working photodetectors, and frequency range of operation.

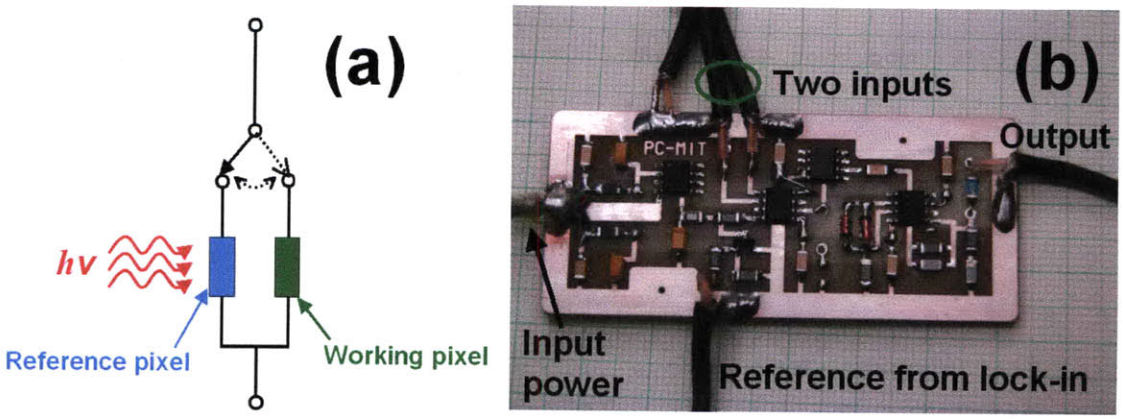

Figure 6.1 To avoid using an external mechanical chopper in an integrated device, an "Electronic Chopping" concept using analog circuits on Si ROIC has been proposed by Professor Joseph Chang's group at NTU, and demonstrated in hybrid format at MIT. (a) Schematic diagram showing the "Electronic Chopper" for integrated devices. This circuit mimics the optical modulation typically obtained by an external mechanical chopper. (b) Based on this idea, a hybrid PC-board "electronic chopper" has been designed and demonstrated at MIT as a prototype.

For the first time, a hybrid PC-board has been constructed using discrete components to demonstrate the feasibility of the above "Electronic Chopping" concept (Figure 6.1 (b)). Two photodetectors made from 500 nm thick PbTe films have been measured using both the traditional optical modulation method and the novel "Electronic Chopping" method, at the same temperature (-60 ^{o}C) and bias current (1 mA). As shown in Figure 6.2, the "Electronic Chopping" approach yields almost identical responsivity spectra as optical modulation for both photodetectors, which is a very important pre-condition for acceptance of this technique in the integration of our photodetectors and Si ROIC.

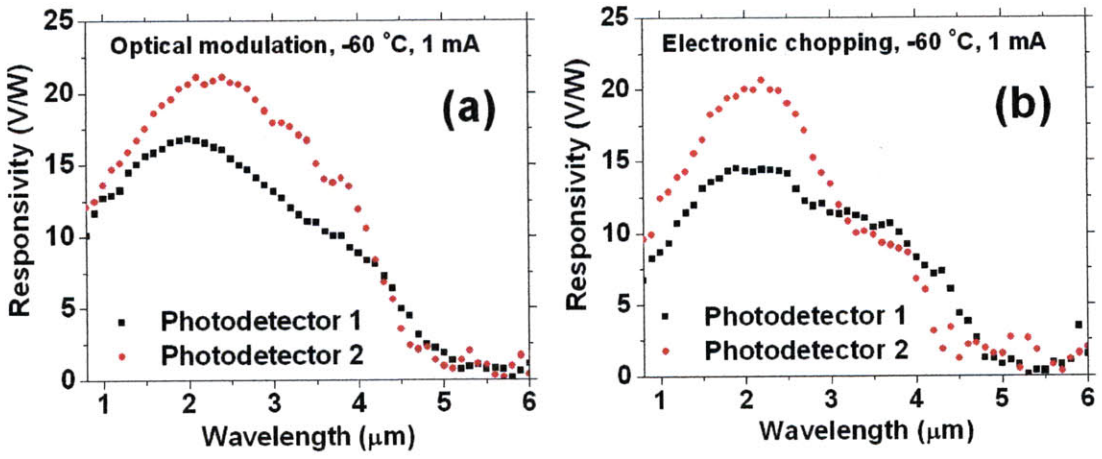

Figure 6.2 Responsivity spectra of two photodetectors at -60 °C and 1 mA. (a) Optical modulation approach using external mechanical chopper. (b) "Electronic Chopping" approach. "Electronic Chopping" yields almost identical results as optical modulation, which is very important for further integration of our photodetectors and Si ROIC.

6.2. Hybrid integration

Before the integration, room temperature I-V curves are tested for all used single waveband RCE photodetectors to ensure their functionality. Figures 6.3 (a) and 6.3 (b) present the results of 400 μm × 400 μm and 200 μm × 200 μm RCE photodetectors respectively. All photodetectors show linear behavior demonstrating ohmic contacts as expected in polycrystalline PbTe photoconductors. The high degree of overlap of all I-V curves illustrates the performance of the photodetectors is very uniform across large substrate area. Table 6.2 summarizes the fitted resistance values from Figure 6.3 results, yielding 169.0 ± 2.9 kΩ corresponding to only 3.4% non-uniformity.

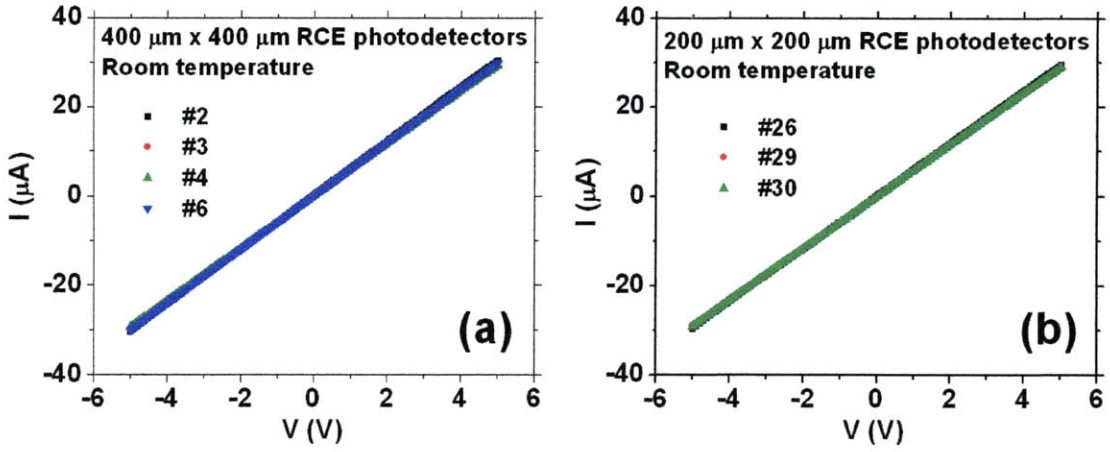

Figure 6.3 Room temperature I-V curves of (a) 400 μm × 400 μm and (b) 200 μm × 200 μm RCE photodetectors. Ohmic contacts are demonstrated in all RCE photodetectors from the linear behavior of the I-V curves. The high degree of overlap of all I-V curves illustrates the performance of the photodetectors is very uniform across large substrate area.

Table 6.2 Fitted resistance values from Figure 6.3 results, yielding 169.0 ± 2.9 kΩ corresponding to a non-uniformity of 3.4%.

400 μm × 400 μm	R (kΩ)	200 μm × 200 μm	R (kΩ)
2	164.5	26	169.4
3	168.0	29	172.8
4	170.1	30	171.8
6	166.6		
Average	169.0	STD	2.9

A TEC cooled chamber for testing Si ROIC and RCE photodetector integrated devices is shown in Figure 6.4 (a). The top surface of the thermoelectrically cooled platform for chip carrier with the electrical connection arrangement (metal "fingers") is also shown in Figure 6.4 (a). Figure 6.4 (b) is the enlarged area highlighted by the green box in Figure

6.4 (a), showing the arrangement of chip carrier, Si ROIC chip, and RCE photodetector chips. Two photodetector chips are placed on both sides of the Si ROIC chip, and together they are glued onto the chip carrier. The chip carrier is then attached to the surface of the TEC's stage with thermally conductive glue. There are several different types of electrical connections for the hybrid structure using different techniques, which are summarized in Table 6.3. Before the chip carrier is loaded into the chamber and the wire soldering, the ultrasonically bonded wires are examined under optical microscope to make sure no wires are disconnected or cross-linked. Figure 6.4 (c) shows the enlarged area highlighted by the red box in Figure 6.4 (b), i.e. one active area of the Si ROIC with all bonded wires.

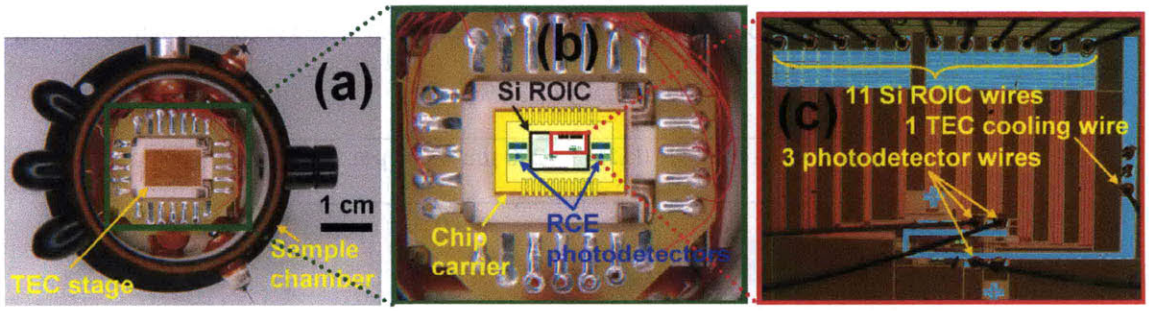

Figure 6.4 (a) TEC cooled chamber for Si ROIC and RCE photodetector integrated devices; (b) enlarged area highlighted by the green box in (a), showing the arrangement of chip carrier, Si ROIC chip, and RCE photodetector chips; (c) enlarged area highlighted by the red box in (b), illustrating one active area of the Si ROIC with all ultrasonically bonded wires.

Table 6.3 Electrical connections for hybrid integration of Si ROIC and single waveband RCE photodetectors.

Electrical connections	Techniques
Si ROIC to chip carrier	Standard ultrasonic wire bonding
Si ROIC to RCE photodetectors	Standard ultrasonic wire bonding & Wire soldering by silver paste
RCE photodetectors to chip carrier	Wire soldering by silver paste
Chip carrier to samples' chamber	Wire soldering by silver paste

Two hybrid devices are fabricated. However, only one device is found to be measurable while the other one is found to have short circuits that could not be fixed. This is possibly due to the cross-link during the wire soldering process from chip carrier to the chamber. The other device is cooled down to -60 °C for measurement. However, during the test the digital section of the Si ROIC is partially non-functional at -60 °C, and this problem remains even after the device is returned back to room temperature. Actually, CMOS process used for the fabrication of the Si ROIC is rated for the temperature range of -40~125 °C, and cooling down to -60 °C may have damaged certain digital circuits in Si ROIC. Other possible failure mechanisms are electrostatic discharge and high voltage across the RCE photodetectors (> 3.3 V limit of Si ROIC). In summary, even though lots of effort has been spent on this hybrid integration strategy, no result has been obtained from the integrated device.

6.3. Monolithic integration

Based on the successful demonstration of single waveband RCE photodetectors in last chapter, RCE photodetectors for 3.6 μm IR light detection are fabricated onto small size

Si ROIC chips (3 mm × 5 mm) monolithically for the first time. Figure 6.5 shows an overview of the three-step lift-off process performed on Si ROIC chips. Only partial region of the Si ROIC is shown in each picture. Starting with bare Si ROIC chip as shown in Figure 6.5 (a), the first lift-off step patterns the bottom mirror stack and PbTe film as shown in Figure 6.5 (b), the second lift-off step patterns the top mirror stack as shown in Figure 6.5 (c), and the third lift-off step patterns the Sn metal layer as shown in Figure 6.5 (d).

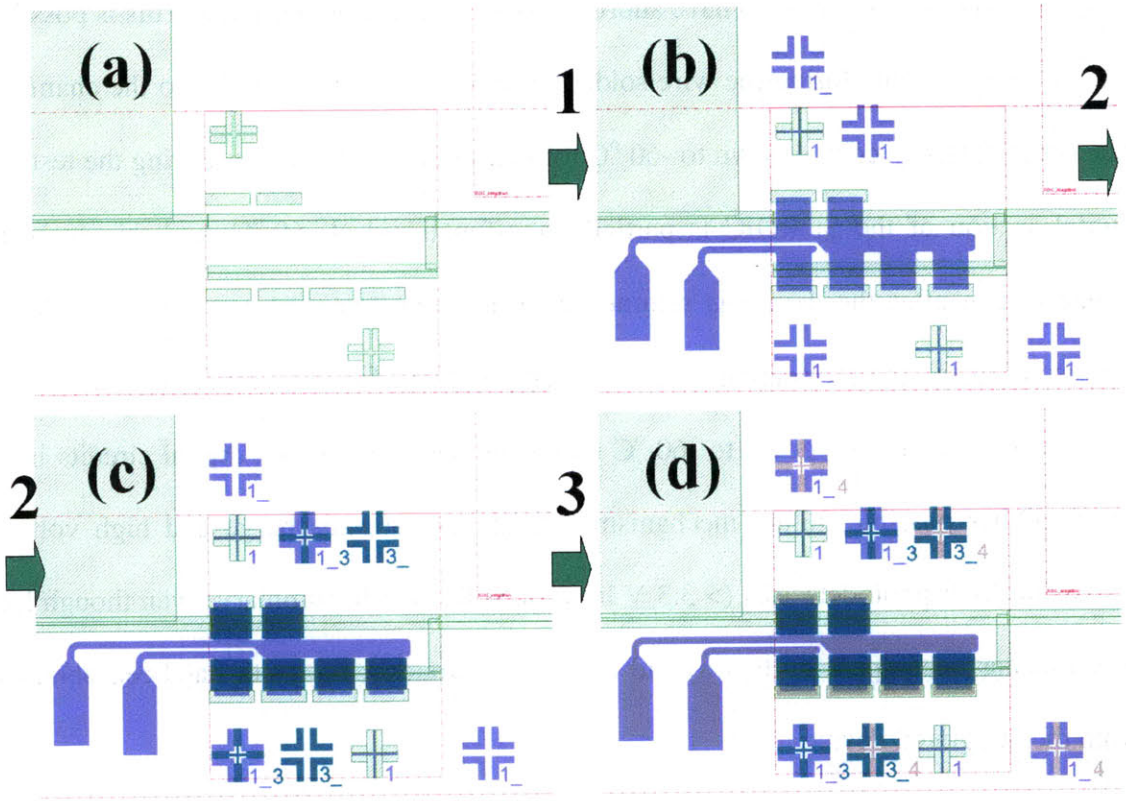

Figure 6.5 An overview of the three-step lift-off process performed on Si ROIC chips. Only partial region of the Si ROIC is shown in each picture. (a) Bare Si ROIC chip; (b) after the first lift-off process to pattern the bottom mirror stack and PbTe film after; (c) after the second lift-off process to pattern the top mirror stack; (d) after the third lift-off process to pattern the Sn metal layer.

Figure 6.6 Small size Si ROIC chip (3 mm × 5 mm) for monolithic integration.

One process challenge arises due to the very small size of Si ROIC chip. It is only 3 mm × 5 mm as shown in Figure 6.6. Our mid-IR RCE photodetector design indicates that the thickness of the photoresist used in the first lift-off process needs to be at least 3 μm, which is already much thicker than commonly used photoresist. Normally, spin-coating and patterning photoresist are performed on a wafer scale substrate which is typically at least several centimeters in diameter. Due to the edge bead effect, photoresist could accumulate at the edge of the wafer up to several times of the nominal thickness in central region. For large size substrates, photoresist thickness non-uniformity and its thickness control are not issues since most active device regions are far away from the edge of the substrate. But when the dimension of the substrate is on the order of millimeters, which is the case for Si ROIC chips, the edge bead effect becomes more prominent across the whole substrate. The handling of such small size substrates as they traverse the entire process sequence is also extremely challenging. Therefore to accommodate such small size Si ROIC chips, we have designed and successfully

demonstrated a technique in which we glue the small chip onto a larger size holder. A new process has been developed to satisfy following requirements*:

(1) Firm attachment: the chip will stay glued during the entire process sequence of 150 °C baking, photoresist spin-coating and patterning, and development in RD6;

(2) Flat surfaces: on both attaching medium and small chip, to make sure excellent/flat mask contact during exposure (glass contact masks are used);

(3) Clean top surface of the chip: avoid touching small Si ROIC chip surface, since circuits and photodetectors will be on top of it. Besides, keep chip surface as clean as possible, to ensure controllable photoresist coating;

(4) Uniform photoresist coating: need to get rid of edge beads and achieve excellent photoresist thickness control.

SU8 2002 is identified as the attaching medium due to its ease of usage in a process and for its robustness against high temperature and most chemicals. Each lift-off step shown in Figure 6.5 by itself includes several processes as illustrated in details in Figure 6.7. Process flow in Figure 6.7 needs to be repeated for every mask level due to the challenges of handling small size Si ROIC chips and patterning films on them. Key process steps and corresponding recipe for each step are summarized in Table 6.4.

---

* The process challenge due to the small size of Si ROIC chip should only exist in the early development stage of this research, but not in the manufacturing stage at full wafer level in the future. For us, cost reduction in the Si ROIC development is more important, but still, one Si ROIC chip costs about $1400.

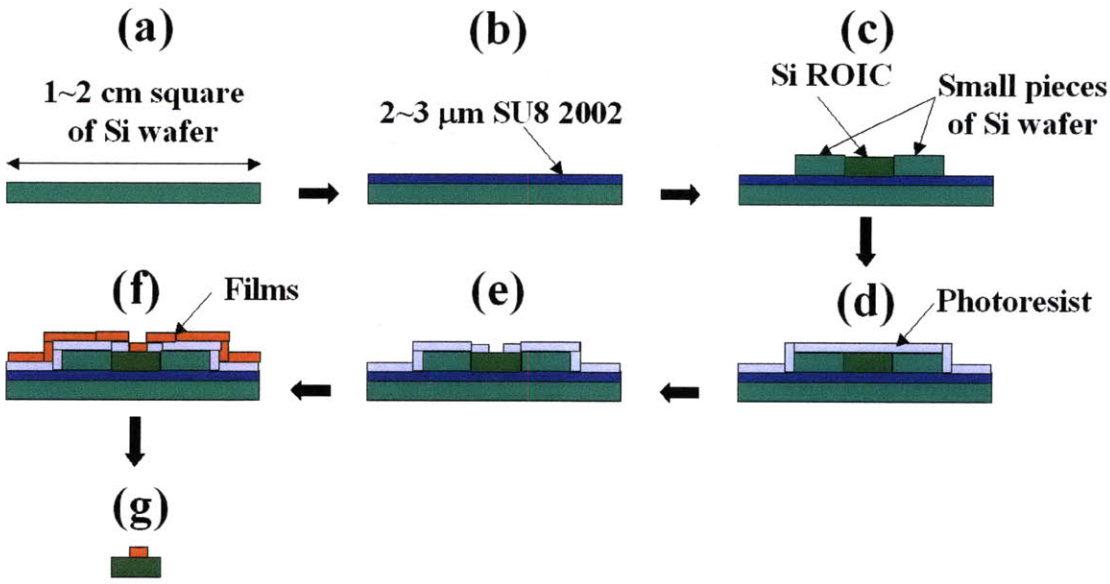

Figure 6.7 Process flow of one lift-off step employed to monolithically integrate mid-IR RCE photodetectors and small size Si ROIC chip (3 mm × 5 mm). (a) Squares of larger size cut from Si wafer as Si ROIC holder; (a) to (b) spin-coating SU8 2002; (b) to (c) loading small size Si ROIC chip and dummies (small pieces of Si wafer sandwiching Si ROIC chip to remove edge beads of photoresist) on SU8 2002; (c) to (d) spin-coating photoresist; (d) to (e) photoresist development; (e) to (f) films deposition; (f) to (g) lift-off in acetone ultrasonic bath.

Table 6.4. Key process steps and detailed recipe for mid-IR RCE photodetectors monolithic integration on Si ROIC chips.

Step #	Process step	Process recipe/purpose
1	Pre-bake to get rid of moisture	150 °C/15 minutes
2	Spin coat SU8 2002	5 s + 35 s (0 to 1500 rpm, 1500 rpm), 2~3 μm in thickness
3	Load Si ROIC chip and two Si wafer pieces onto Si substrate holder	Two Si wafer pieces sandwiching Si ROIC chip to get rid of photoresist edge beads afterwards
4	Cure SU8 2002	100 °C/2 minutes

Table 6.4. (Continued) Key process steps and detailed recipe for mid-IR RCE photodetectors monolithic integration on Si ROIC chips.

5	Spin coat photoresist NR71-3000PY	20 s + 40 s (0 to 3000 rpm, 3000 rpm), for photoresist >3 μm
6	Pre-exposure bake	150 °C/2 minutes
7	Exposure	60 s by Broadband, 40 s by MA4 (EML)
8	Post-exposure bake	100 °C/2 minutes
9	Development	60~80 s in RD6
10	Film deposition	Bottom DBR and PbTe
11	First lift-off	5~6.5 minutes in acetone ultrasonic bath
12	Repeat steps 1-4	
13	Spin coat photoresist NR9-1000PY	10 s + 5 s + 35 s (750 rpm, 750 to 1600 rpm, 1600 rpm), for photoresist >1 μm
14	Pre-exposure bake	150 °C/80 s
15	Exposure	20 s by MA4 (EML)
16	Post-exposure bake	100 °C/80 s
17	Development	7 s in RD6
18	Film deposition	Top DBR
19	Second lift-off	1~2 minutes in acetone ultrasonic bath
20	Repeat steps 1-4	
21	Spin coat photoresist NR9-1000PY	10 s + 5 s + 35 s (750 rpm, 750 to 1600 rpm, 1600 rpm), for photoresist >1 μm
22	Pre-exposure bake	150 °C/80 s
23	Exposure	20 s by MA4 (EML)
24	Post-exposure bake	100 °C/80 s
25	Development	7 s in RD6

Table 6.4. (Continued) Key process steps and detailed recipe for mid-IR RCE photodetectors monolithic integration on Si ROIC chips.

26	Metal deposition	100 nm Sn by e-beam evaporation (EML): X = 0; Y = 0; SX = 0.25; SY = 0.25; <4.3×10^{-5} Torr; 0.13 A; 1.8~1.9 Å/s
27	Third lift-off	80~90 s in acetone ultrasonic bath

Figure 6.8 shows the top down view and cross-sectional view of the RCE photodetectors monolithically integrated on Si ROIC schematically. Even though this fabrication process is extremely challenging due to the small size (3mm × 5mm) and non-flat surface (~1.5 μm step) of Si ROIC chips, three-step lift-off process is performed on four Si ROIC chips, and two integrated chips are successfully fabricated. Electrical connections between Si ROIC chip and chip carrier is achieved by standard ultrasonic wire bonding. Connections from RCE photodetectors to chip carrier (for external bias current) and from chip carrier to samples' chamber are achieved by wire soldering using silver paste. Of the two integrated devices, one is found to have internal short circuits and despite different strategies are attempted to solve this problem, the short circuits remains. The other device is found to be measurable and the Si ROIC circuits are functional.

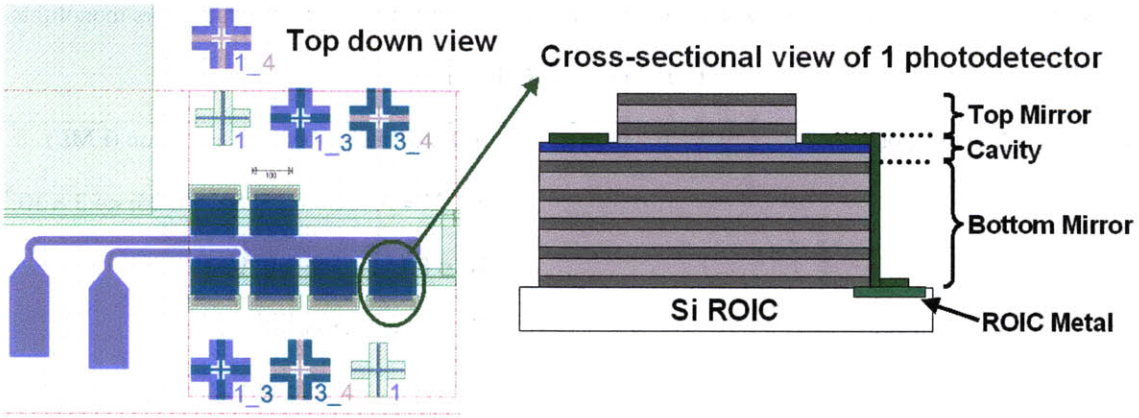

Figure 6.8 Schematic top down view and cross-sectional view of the monolithically integrated device.

Figure 6.9 shows the top down view of the Si ROIC active area before and after the RCE photodetector fabrication. From Figure 6.9 (b), we demonstrate excellent alignment for all three mask levels. The devices are characterized by photoconductivity measurements. Temperature is lowered down to -30 ^{o}C gradually to make sure Si ROIC circuits remain functional. Bias current is also increased from 0 μA to 20 μA slowly. Under monochromatic light illumination, no output voltage has been observed due to low light power density, low bias current, and limited cooling required by Si ROIC. Under broadband light source illumination (100 W quartz tungsten halogen, or QTH lamp), a linear relationship between the output voltage from Si ROIC and the bias current is obtained as shown in Figure 6.10. This is consistent with our previous experimental results and analytical model showing linear dependence of responsivity on the bias current.

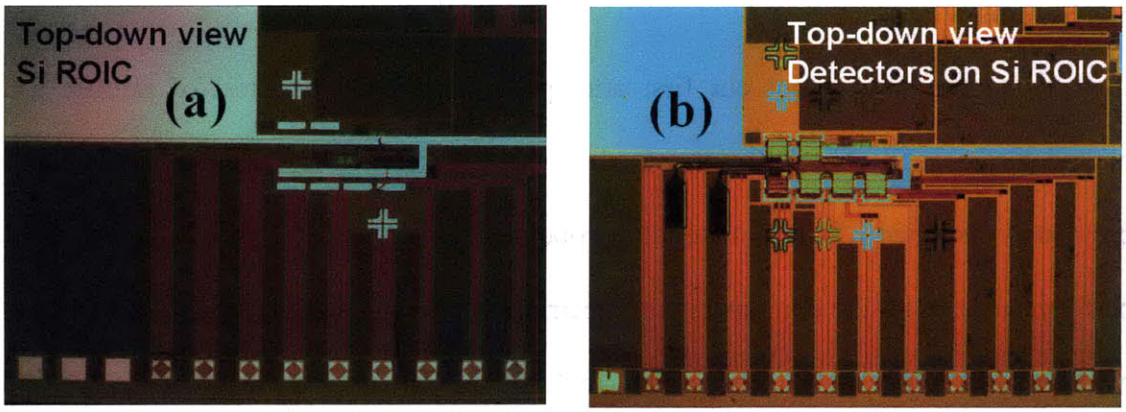

Figure 6.9 Top down view of the Si ROIC active area (a) before and (b) after the single waveband RCE photodetector fabrication. Excellent alignment for all three mask levels has been demonstrated by Figure 6.9 (b).

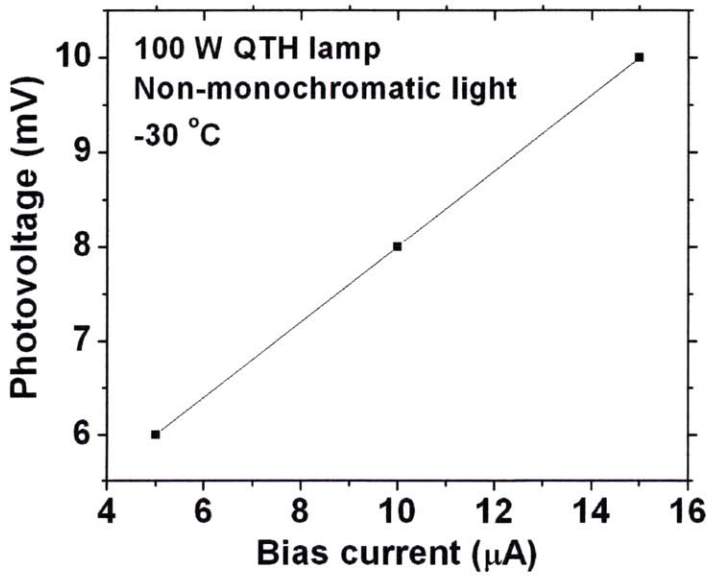

Figure 6.10 Photovoltage signal from Si ROIC as a function of bias current under non-monochromatic light illumination from a 100 W QTH lamp. Linear dependence is demonstrated as expected.

6.4. Summary

In this chapter, we present our first attempt in fabrication and test of mid-IR RCE photodetectors and Si ROIC integrated devices. Si ROIC is designed according to previously studied PbTe material properties and mid-IR RCE photodetector performances. With the demonstrated "Electrical Chopping" concept, optical modulation by an external mechanical chopper is replaced by an on-chip integrated "Electronic Chopper" for our photoconductive devices.

Two integration strategies for 3.6 μm RCE photodetectors and Si ROIC chips are evaluated. One is hybrid structure, and the other is monolithic integration. The test of the hybrid devices is largely unsuccessful, due to cross-link during the wire soldering process, excessive cooling, electrostatic discharge, and high voltage developed across the photodetector. On the other hand, based on the process developed for small size Si ROIC chips (3 mm × 5 mm), monolithically integrated devices are successfully fabricated and tested. The result is partially successful as linear dependence of output voltage on the bias current is obtained. This data unambiguously depicts that a monolithically integrated device of RCE photodetectors and Si ROIC is indeed feasible.

Chapter 7. Summary and future work

7.1. Summary

The holy grill of this work is monolithic integration of focal plane arrays (FPA) of multispectral infrared (IR) photodetectors and silicon readout integrated circuits (Si ROIC). We investigate and develop appropriate polycrystalline material to detect IR radiation, explore and establish a novel way to realize IR multi-band detection on a single photodetector, design and demonstrate resonant-cavity-enhanced (RCE) photodetectors with improved device performance, and finally evaluate and validate the feasibility of monolithic integration of RCE photodetectors and Si ROIC. With properly chosen polycrystalline and amorphous materials, the cost of fabrication can be greatly reduced. Our work also opens the way to integrate the IR photodetector arrays with Si ROIC to further reduce the cost and improve the reliability of the system.

In chapters 2 and 3, we focus on the development of mid-IR photosensitive polycrystalline material, i.e. PbTe films, which could enable monolithic integration of IR photodetectors and Si ROIC. We demonstrate the feasibility of using thin polycrystalline PbTe film (100 nm) as IR absorbing layer in order to enhance signal-to-noise ratio in the wavelength range of 0.8~5 μm. Study on PbTe films' structural, electrical, and optical properties facilitate understanding photoconductivity mechanism in the films and constructing models to predict photo-responsivity and detectivity. Our PbTe films can be deposited by more cost-effective technique than MBE or MOCVD, i.e. single source thermal evaporation. Microstructure study confirms the films are stoichiometric single-phase polycrystalline with (200) texture and through thickness grain boundaries.

Electrical properties of the films are analyzed in the framework of a grain boundary channel conduction model. We demonstrate the existence of oxygen in the films and find out oxygen is responsible for the p-type conduction and very low carrier concentrations, since oxygen can diffuse through the grain boundaries and pin the Fermi level near mid-gap. According to our model of responsivity, low carrier concentration is essential to achieve excellent photo-responsivity as observed in our polycrystalline PbTe films. Quantum efficiency spectra can be directly measured by optical experiment. Optical property study also yields wavelength dependent refractive index and extinction coefficient, which are critical for simulating RCE multi-layer structures afterwards. Moreover, all possible noises in polycrystalline PbTe photoconductors are evaluated and compared with experimental results. Johnson noise is identified as dominant intrinsic noise in PbTe photoconductors and detectivity as high as 10^{10} $cmHz^{1/2}/W$ (-60 °C, 3.6 μm) could be expected.

Chapter 4 presents a novel design of cavity-enhanced multispectral photodetectors using phase-tuned propagation, and also preliminary experimental results of dual waveband RCE photodetectors. We start with design and fabrication of mid-IR distributed Bragg reflectors (DBR) used to form cavity structures to enhance quantum efficiency. With single layer's optical properties, quarter wavelength stack (QWS) of thermally evaporated As_2S_3 and sputtered Ge films is designed, fabricated, and analyzed. We demonstrate mid-IR photonic band gap (PBG) and >99% reflectance in the range of 3.5~3.8 μm in the DBR structure designed for 3.6 μm. Then we theoretically analyze our novel design of cavity-enhanced photodetectors capable of sensing multiple wavelengths

simultaneously in a single photodetector. Peak quantum efficiencies over 80% have been realized in both wavebands (1.55 μm and 3.6 μm) with only 50 nm and 100 nm thick PbTe IR absorbers, and spectral cross talk as low as 0.1% is obtained. The design is based on phase-tuned propagation of resonant modes in cascaded planar resonant cavities, and due to its versatility and scalability, this concept can be generalized to detect virtually any arbitrary number of wavelengths. Preliminary optical measurement on our first attempt of fabricated dual waveband RCE photodetectors demonstrate the two resonant cavity modes at 1.61 μm and 3.70 μm. Quantum efficiencies as high as 92% and 68% have been achieved in two wavebands respectively.

In chapter 5, we design, fabricate, and validate fully functional single waveband mid-IR RCE photodetectors on a silicon platform (3.5 μm). According to the design in chapter 4, single waveband RCE photodetectors serve as building blocks for multiple waveband RCE photodetectors, thus this step is essential for the development of multispectral photodetectors. We demonstrate high quantum efficiency (90%) and a peak responsivity of 100 V/W at the resonant wavelength of 3.5 μm, 13.4 times higher compared to blanket PbTe film of the same thickness. Detectivity as high as 0.72×10^{9} $cmHz^{1/2}W^{-1}$ has been achieved, comparable with commercial polycrystalline mid-IR photodetectors. As low temperature processing (150 °C) is implemented in the entire fabrication process, this demonstration shows promise for monolithic integration of RCE photodetectors with Si readout integrated circuits (Si ROIC).

Chapter 6 shows the preliminary results on our first attempt in fabricating single waveband (3.6 μm) RCE photodetectors integrated with Si ROIC. Both hybrid and monolithic integration strategies are evaluated. We have developed the fabrication process that enables monolithic integration of RCE photodetectors on Si ROIC chips with the area of only 3 mm × 5 mm. The devices are characterized by photoconductivity measurements. Under monochromatic light illumination, no output voltage has been observed due to low bias current and limited cooling restricted by Si ROIC. Under broadband light source illumination, a linear relationship between the output voltage from Si ROIC and the bias current is obtained as expected, which shows high promise for monolithic integration of RCE photodetector arrays and Si ROIC in the future.

7.2. Future work

There are several aspects that we could explore in more detail in the future work.

(1) Materials perspective: within the thermal budget of Si ROIC, we need to further improve the quality of polycrystalline PbTe films for mid-IR radiation detection, e.g. increasing carrier lifetime or reducing carrier concentration. One may notice: we use 100 nm thickness in the RCE photodetector compared to 1~10 μm in a commercial photodetector of similar type, and an RCE photodetector with a thinner active layer leads to less noise and higher signal-to-noise ratio than a thicker similar photodetector, but finally we have obtained "only" comparable detectivity (D^*) with commercial detectors (chapter 5). This is because even though the measured quantum efficiency is ~90%, the carrier lifetime is only ~1 ns at -60 °C, which is relatively much shorter than reported

values for single crystalline PbTe films (100~1000 ns around -60 °C)[77]. As a consequence, the responsivity is not as high as commercial photodetectors, and with reduced noise, the detectivity is comparable with commercial ones. One could expect at least one order of magnitude improvement in responsivity and D^* with increased carrier lifetime. As we have discussed in part 3.2.2, most oxygen atoms incorporated into the films are electrically non-active, and no carrier lifetime enhancement has been observed due to minority carrier traps, e.g. $(PbO)^{2+}$. Annealing films at alleviated temperature and even in an oxidizing atmosphere may increase the carrier lifetime and thus enhance the photoconductivity as demonstrated in most polycrystalline PbSe and PbS films[60]. On the other hand, further reducing oxygen concentration down to ~10^{18} cm^{-3} level in the films by diffusion barrier or oxygen getter during deposition could lead to lower carrier concentration, which may also contribute to improved photoconductivity.

Another direction to explore is extending PbTe detection capability to long-IR (8~12 μm) by alloying with SnTe, as we have shown at the very beginning. Historically, PbSnTe alloy has been the primary alternative IR photodetector material replacing HgCdTe alloy. Two reasons retard PbSnTe research around late 1970s: high dielectric constant and large thermal mismatch with Si (different temperature coefficients of expansion). The former is not compatible with the scanned IR imaging devices at that time which need relatively short response times, and the latter can result in failure of the electrical connections in hybrid structure (indium bonds between the photodetector array and Si ROIC) since the devices have to undergone frequent thermal cycling between room temperature and cryogenic temperature during operation. However, nowadays staring focal plane arrays

become the dominant research trend, which do not consider fast response as critical as before. Additionally, with novel polycrystalline materials developed for monolithic integration on Si ROIC, neither lattice nor thermal mismatch with Si would be an issue. Therefore, PbSnTe alloy is still a very promising material candidate for mid-IR and long-IR radiation detection.

(2) Device structure perspective: instead of using a photoconductor's configuration, Schottky diodes may operate under much lower bias current or even without bias current, which could permit higher density focal plane arrays within the power budget. To achieve high collection efficiency, one prerequisite is long diffusion length of the photo-generated carriers that should be comparable to the length of the device l. Using Einstein relation, i.e. $D = \frac{\mu_p kT}{q}$, and experimentally measured carrier mobility (36 $cm^2V^{-1}s^{-1}$ at -60 °C), one can calculate the diffusion constant D=0.66 cm^2s^{-1}. For a 100 μm long diode, the carrier lifetime τ should satisfy $\tau \geq \frac{l^2}{D} = 151$ μs. This value is much larger than the value of our current polycrystalline PbTe films, i.e. ~1 ns at -60 °C. Thus further improving the material quality becomes the key to realize the high performance of the diode devices.

Some of our preliminary experiment shows contacts of different metals (Pb and Sn) on the polycrystalline PbTe films could yield non-ohmic behavior and act like a Schottky diode. However, there is very rare deposition facility for Pb arising from challenges of the environmental consideration against heavy elements. Besides, more complicated electrical contact configuration and thus fabrication process remain to be solved.

Although there are still many challenges to solve before we can monolithically integrate focal plane arrays of multispectral IR photodetectors and Si ROIC for real applications, the physics of the devices is sound and related fabrication problems should be resolved eventually. The polycrystalline PbTe devices have promising future for IR detection applications in which advanced functionality and affordable expense are dominant considerations.

References

[1] J. Liu, J. Michel, W. Giziewicz, D. Pan, D. Cannon, D. Danielson, S. Jongthammanurak, K. Wada, and L. Kimerling, "High-performance, tensile-strained Ge p-i-n photodetectors on a Si platform", *Appl. Phys. Lett.*, **87**, 103501 (2005).

[2] P. Norton, "Infrared detectors in the next millennium", *Proc. SPIE*, **3698**, 652-665 (1999).

[3] A. Rogalski, "Infrared detectors: an overview", *Infrared Physics and Technology*, **43**, 187-210 (2002).

[4] Y. Chen, S. Williamson, T. Brock, F. Smith, and A.Calawa, "375GHz-bandwidth Photoconductive Detector", *Appl. Phys. Lett.*, **59**, 1984 (1991).

[5] M.Razeghi, "Current status and future trends of infrared detectors", *Opto-Electron. Rev.*, **6**, 155-194 (1998).

[6] R. Wood, C. Han, P. Kruse, "Integrated uncooled IR detector imaging arrays", *Proc. IEEE Solid State Sensor and Actuator Workshop*, Hilton Head Island, S.C., June, 132-135 (1992).

[7] A. Rogalski, "IR detectors: status and trends", *Progress in Quantum Electronics,* **27**, 59-210 (2003).

[8] http://www.optoprecision.de/index.php?id=33&L=1

[9] A. Rogalski, J. Antoszewski, L. Faraone, "Third-generation infrared photodetector arrays", *J. Appl. Phys.* **105**, 091101 (2009).

[10] J. Albertz, H. Ebner, and G. Neukum, in *International Archives of Photogrammetry and Remote Sensing*, vol. **31**, Part B4, pp. 58{63 (Vienna, Austria, 1996).

[11] R. Sandau and A. Eckardt, in *International Archives of Photogrammetry and Remote Sensing*, vol. **31**, Part B4, pp. 170-175 (Vienna, Austria, 1996).

[12] S. Baronti, A. Casini, F. Lotti, and S.Porcinai, "Multispectral Imaging System for the Mapping of Pigments in Works of Art by use of Principal-Component Analysis," *Appl. Optics* **37**, 1299 (1998).

[13] S. W. Seo, D. Geddis, and N. M. Jokerst, "3D Stacked Thin Film Photodetectors for Multispectral Detection Applications," *IEEE Photon. Technol. Lett.* **15**, 578-580 (2003).

[14] D. Krapf, B. Adoram, J. Shappir, A. Saar, S. G. Thomas, J. L. Liu, and K. L. Wang, "Infrared multispectral detection using Si/Si_xGe_{1-x} quantum well infrared photodetectors," *Appl. Phys. Lett.* **78**(4), 495-497 (2001).

[15] A. Goldberg, S. Kennerly, J. Little, T. Shafer, C. Mears, H. Schaake, M. Winn, M. Taylor, and P. Uppal, "Comparison of HgCdTe and quantum-well infrared photodetector dual-band focal plane arrays," *Opt. Eng.* **42**, 30-46 (2003).

[16] A. Kock, E. Gornik, G. Abstretier, G. Bhom, M. Walther, and G. Weimann, "Double wavelength selective GaAs/AlGaAs infrared detector device," *Appl. Phys. Lett.* **60**(16), 2011-2013 (1992).

[17] S. D. Gunapala, S. V. Bandara, J. K. Liu, J. M. Mumolo, C. J. Hill, S. B. Rafol, D. Salazar, J. Woollaway, P. D. LeVan, and M. Z. Tidrow, "Towards dualband megapixel QWIP focal plane arrays," *Infrared Phys. Technol.* **50**, 217-226 (2007).

[18] L. G. Hipwood, C. L. Jones, C. D. Maxey, H. W. Lau, J. Fitzmaurice, R. A. Catchpole, and M. Ordish, "Three-color MOVPE MCT diodes," *Proc. SPIE* **6206**, 620612 (2006).

[19] http://www.dtic.mil/ndia/2002nightop/waterman.pdf, "Two Color IRFPAs for Navy Missile Warning," James R. Waterman (2002).

[20] J. Wang, J. Hu, X. Sun, A. M. Agarwal, L. C. Kimerling, D. R. Lim, and R. A. Synowicki, "Structural, electrical, and optical properties of thermally evaporated nanocrystalline PbTe films," *J. Appl. Phys.* **104**, 053707 (2008).

[21] D. E. Bode, T. H. Johnson, and B. N. McLean, "Lead selenide detectors for intermediate temperature operation," *Applied Optics* **4**, 327 (1965).

[22] T. H. Johnson, H. T. Cozine, and B. N. McLean, "Lead selenide detectors for ambient temperature operation," *Applied Optics* **4**, 693 (1965).

[23] R. Dalven, "A review of the semiconductor properties of PbTe, PbSe, PbS and PbO," *Infrared Physics* **9**, 141-184 (1969).

[24] P. J. Lin and L. Kleinman, "Energy bands of PbTe, PbSe, and PbS," *Phys. Rev.* **142**, 478 (1966).

[25] D. L. Mitchell, E. D. Palik, and J. N. Zemel, *Physics of Semiconductors; Proc. 7th Int. Congr.*, Paris 1964, edited by M. Hulin, p. 325. Academic Press (1964).

[26] J. N. Zemel, J. D. Jensen, and R. B. Schoolar, "Electrical and optical properties of epitaxial films of PbS, PbSe, PbTe, and SnTe," *Phys. Rev.* **140**, A330 (1965).

[27] http://www.marlow.com/thermoelectric-modules/four-stage/

[28] A. R. Calawa, T. C. Harman, M. Finn, and P. Youtz, "Crystal growth, annealing and diffusion of lead-tin chalcogenides," *Trans. Metall. Soc. AIME* **242**, 374 (1968).

[29] I. Melngailis, T. C. Harman, "Single-crystal lead-tin chalcogenides," in *Semiconductors and Semimetals*, New York 1970, edited by R. K. Willardson, A. C. Beer, vol. 5, pp111-174, Academic Press (1970).

[30] I. Melngailis, T. C. Harman, "Photoconductivity in single-crystal PbSnTe," *Appl. Phys. Lett.* **13**, 180 (1968).

[31] T. S. Moss, "Lead salt photoconductors," *Proc. IRE* **43**, 1869-1881 (1955).

[32] F. S. Terra, M. Abdel-Rafea, M. Monir, "Photoconductivity and electrical properties of $Pb_{1-x}Sn_xTe$ thin films," *Journal of Materials Science: Materials in Electronics* **12**, 561-567 (2001).

[33] Y. A. Ugai, A. M. Samoylov, M. K. Sharov, and A. V. Tadeev, "Crystal microstructure of PbTe/Si and PbTe/SiO2/Si thin films," *Thin Solid Films* **336**, 196 (1998).

[34] Powder Diffraction File (PDF) card No. 781905.

[35] U. P. Khairnar, P. H. Pawar, G. P. Bhavsar, "Study of transport properties co-evaporated lead telluride (PbTe) thin films," *Cryst. Res. Technol.* **37**(12), 1293 (2002).

[36] K. R. Maskaly, W. C. Carter, R. D. Averitt, and J. L. Maxwell, "The effect of interfacial roughness on the normal incidence bandgap of one-dimensional photonic crystals," *Opt. Express* **13**(21), 8380 (2005).

[37] K. R. Maskaly, G. R. Maskaly, W. C. Carter, and J. L. Maxwell, "Sample-inverted reflow technique for fabrication of a revolved-hyperboloid microlens array in hybrid solgel glass," *Opt. Lett.* **29**, 2791 (2004).

[38] T. Komissarova, D. Khokhlov, L. Ryabova, Z. Dashevsky and V. Kasiyan, "Impedance of photosensitive nanocrystalline PbTe(In) films," *Phys. Rev. B* **75**, 195326 (2007).

[39] O.A. Gudaev, V.K. Malinovsky, E.E. Paul and V.A. Treshikhin, "Nonactivation nature of conductivity in disordered materials," *Solid State Communications* **74**, 1169 (1990).

[40] Z. Dashevsky, *Handbook of Semiconductor Nanostructures and Nanodevices* **2**, 335 (2006).

[41] N. F. Mott, "Conduction in non-crystalline materials. III. Localized states in a pseudogap and near extremities of conduction and valence bands," *Phil. Mag.* **19**, 835 (1969).

[42] J. Hu, X. Sun, A. M. Agarwal, J. Viens, L. C. Kimerling, L. Petit, N. Carlie, K. C. Richardson, T. Anderson, J. Choi, and M. Richardson, "Studies on structural, electrical, and optical properties of Cu doped As-Se-Te chalcogenide glasses," *J. Appl. Phys.* **101**, 063520 (2007).

[43] R. Swanepoel, "Determination of the thickness and optical constants of amorphous silicon," *J. Phys. E* **16**, 1214 (1983).

[44] V. Srikant and D. R. Clarke, "On the optical band gap of zinc oxide," *J. Appl. Phys.* **83**(10), 5447 (1998).

[45] D.B. Haddad, J.S. Thakur, V.M. Naik, G.W. Auner, R. Naik, and L.E. Wenger, "Optical band gap measurements of InN films in the strong degeneracy limit," *Mat. Res. Soc. Symp. Proc.* **743**, L11.22.1-6 (2003).

[46] J. Tauc, in Amorphous and Liquid Semiconductors, edited by J. Tauc (Plenum, New York, 1974), p. 159.

[47] A. L. Rogach, A. Eychmüller, S. G. Hickey, and S. V. Kershaw, "Infrared emitting colloidal nanocrystals: synthesis, assembly, spectroscopy, and applications," *Small* **3**, 536 (2007).

[48] W. D. Lawson, F. A. Smith, and A. S. Young, "Influence of crystal size on the spectral response limit of evaporated PbTe and PbSe photoconductive cells," *J. Electrochem. Soc.* **107**(3), 206-210 (1960).

[49] J. Wang, J. Hu, P. Becla, A. Agarwal, and L. C. Kimerling, "Highly textured, room-temperature-sensitized nanocrystalline PbTe film on silicon for infrared detection," *Phys. Rev. B* (submitted, 2010).

[50] J. Wang, J. Hu, X. Sun, P. Becla, A. Agarwal, and L. Kimerling, "Cavity-enhanced Multispectral Photodetector on a Si Platform --- Theory, Materials, and Devices," in Integrated Photonics Research, Silicon and Nano Photonics, (Optical Society of America, 2010), ITuA4.

[51] J. Wang, J. Hu, P. Becla, A. Agarwal, and L. Kimerling, "Highly Textured Nanocrystalline PbTe Films on a Silicon Platform for Low Cost IR Detection," in MRS fall meeting in Boston, MA. December 2, 2009, B11.4.

[52] J. Wang, J. Hu, X. Sun, A. Agarwal, D. Lim, and L. Kimerling, "One-dimensional Photonic Crystal and Photoconductive PbTe Film for Multi-spectral Mid-infrared Photodetector," in Integrated Photonics and Nanophotonics Research and Applications, (Optical Society of America, 2008), IWE6.

[53] R. L. Petritz, "Theory of photoconductivity in semiconductor films," *Phys. Rev.* **104**, 1508 (1956).

[54] J. N. Humphrey and W. W. Scanlon, "Photoconductivity in lead selenide. Experimental," *Phys. Rev.* **105**, 469 (1957).

[55] J. N. Humphrey and R. L. Petritz, "Photoconductivity of lead selenide: theory of the mechanism of sensitization," *Phys. Rev.* **105**, 1736 (1957).

[56] J. C. Slater, "Barrier theory of the photoconductivity of lead sulfide," *Phys. Rev.* **103**, 1631 (1956).

[57] Y. Yasuoka, T. Seki, and M. Wada, "The effects of oxygen on evaporated PbSe films," *Jpn. J. Appl. Phys.* **7**, 1186 (1968).

[58] Y. Yasuoka and M. Wada, "Photoconductivity of PbSe films," *Jpn. J. Appl. Phys.* **9**, 452 (1970).

[59] Y. Yasuoka and M. Wada, "Thermally stimulated current of vacuum deposited PbSe films," *Jpn. J. Appl. Phys.* **13**, 1797 (1974).

[60] E. L. Dereniak and G. D. Boreman, in *Infrared Detectors and Systems*, edited by J. W. Goodman (Wiley-Interscience, New York, 1996).

[61] Vigo System, www.vigo.com.pl

[62] Following parameters are used for the extrapolation: quantum efficiency of 80% for a 100 nm thick PbTe film in a cavity structure, 100 μm square pixel, 0.1 mA bias current, 60 $cm^2/V/s$ as hole mobility, and 2×10^{16} cm^{-3} as hole concentration.

[63] D. E. Bode and H. Levinstein, "Effect of oxygen on the electrical properties of lead telluride films," *Phys. Rev.*, *96*, 259 (1954).

[64] K. S. Bhat and V. D. Das, "Electrical-conductivity changes in PbTe and PbSe films on exposure to the atmosphere," *Phys. Rev. B 32*, 6713 (1985).

[65] R. F. Egerton and C. Juhasz, "The effect of oxygen on epitaxial PbTe, PbSe and PbS films," *Thin Solid Films* ***4***, 239 (1969).

[66] F. Briones, D. Golmayo, and C. Ortiz, "The role of oxygen in the sensitization of photoconductive PbSe films," *Thin Solid Films* ***78***, 385 (1981).

[67] Z. Dashevsky, R. Kreizman, and M. P. Dariel, "Physical properties and inversion of conductivity type in nanocrystalline PbTe films," *J. Appl. Phys.* ***98***, 094309 (2005).

[68] E. I. Rogacheva, I. M. Krivulkin, O. N. Nashchekina, A. Yu. Sipatov, and V. V. Volobuev, and M. S. Dresselhaus, "Effect of oxidation on the thermoelectric properties of PbTe and PbS epitaxial films," *Appl. Phys. Lett.* **78** (12), 1661 (2001).

[69] E. I. Rogacheva, T. V. Tavrina, S. N. Grigorov, O. N. Nashchekina, V. V. Volobuev, A. G. Fedorov, K. A. Nasedkin, and M. S. Dresselhaus, "Effect of oxidation on the thermoelectric properties of PbSe thin films," *Journal of Electronic Materials* **31** (4), 298 (2002).

[70] E.I Rogacheva, T.V Tavrina, O.N Nashchekina, S.N Grigorov, A.Yu Sipatov, V.V Volobuev, M.S Dresselhaus, and G Dresselhaus, "Influence of oxidation on the transport properties of IV–VI-thin films," *Physica E* **17**, 310 (2003).

[71] E. I. Rogacheva, T. V. Tavrina, O. N. Nashchekina, V. V. Volobuev, A. G. Fedorov, A. Yu. Sipatov, and M. S. Dresselhaus, "Effect of non-stoichiometry on oxidation processes in n-type PbTe thin films," *Thin Solid Films* **423** (2), 257 (2003).

[72] E. I. Rogacheva, S. G. Lyubchenko, and M. S. Dresselhaus, "Effect of oxidation on thickness dependencies of thermoelectric properties in PbTe-mica thin films," *Thin Solid Films* **476**, 391 (2005).

[73] A. Munoz, J. Melendez, M. C. Torquemada, M. T. Rodrigo, J. Cebrian, A. J. de Castro, J. Meneses, M. Ugarte, F. Lopez, G. Vergara, J. L. Hernandez, J. M. Martin, L. Adell, and M. T. Montojo, "PbSe photodetector arrays for IR sensors," *Thin Solid Films* **317**, 425 (1998).

[74] M. C. Torquemada, M. T. Rodrigo, G. Vergara, F. J. Sanchez, R. Almazan, M. Verdu, P. Rodriguez, V. Villamayor, L. J. Gomez, M. T. Montojo, and A. Munoz, "Role of halogens in the mechanism of sensitization of uncooled PbSe infrared photodetectors," *J. Appl. Phys.* ***93***, 1778 (2003).

[75] J. Diezhandino, G. Vergara, G. Perez, I. Genova, M. T. Rodrigo, F. J. Sanchez, M. C. Torquemada, V. Villamayor, J. Plaza, I. Catalan, R. Almazan, M. Verdu, P. Rodriguez, L. J. Gomez, M. T. Montojo, "Monolithic integration of spectrally selective uncooled lead selenide detectors for low cost applications," *Appl. Phys. Lett.* **83**, 2751 (2003).

[76] F. Galeskii, A. E. Yunovich, K. H. Herrmann, H. Kostial, I. Rechenberg, and P. Schafer, "Stimulated emission, absorption spectra, and recombination in epitaxial PbTe," *Phys. Stat. Sol. B* **88**, 675 (1978).

[77] B. Schlicht, R. Dornhaus, G. Nimtz, L. D. Haas, and T. Jakobus, "Life time measurements in PbTe and PbSnTe," *Solid-state Electronics* **21**, 1481-1485 (1978).

[78] J. Wang, J. Hu, X. Sun, A. Agarwal, and L. Kimerling, "Cavity-enhanced multispectral photodetector with phase-tuned propagation: theory and design," *Optics Letters* **35** (5): 742-744 (2010).

[79] X. C. Sun, Ge-on-Si Light-Emitting Materials and Devices for Silicon Photonics, 167-177 (PhD thesis, MIT, 2009).

[80] X. C. Sun, J. J. Hu, C. Y. Hong, J. F. Viens, X. M. Duan, R. Das, A. M. Agarwal, and L. C. Kimerling, "Multispectral pixel performance using a one-dimensional photonic crystal design," *Appl. Phys. Lett.* **89**, 223522 (2006).

[81] A. Yariv, "Universal relations for coupling of optical power between microresonators and dielectric waveguides," *Electron. Lett.* **36**, 321-322 (2000).

[82] J. D. Joannopoulos, S. G. Johnson, J. N. Winn, and R. D. Meade, Photonic Crystals: Molding the Flow of Light (Princeton University Press, 2008).

[83] M. S. Unlu and S. Strite, "Resonant cavity enhanced photonic devices," *J. Appl. Phys.* **78**, 607-639 (1995).

[84] Y. Fink, J. N. Winn, S. Fan, C. Chen, J. Michel, J. D. Joannopoulos, E. L. Thomas, "A dielectric omnidirectional reflector," *Science* **282**, 1679-1682 (1998).

[85] S. Saini, C. Y. Hong, N. Pfaff, L. C. Kimerling, and J. Michel, "Partial confinement photonic crystal waveguides," *Appl. Phys. Lett.* **93**, 261102 (2008).

[86] R. A. Coussa, A. M. Gallagher, K. Kosai, L. T. Pham, G. K. Pierce, E. P. Smith, G. M. Venzor, T. J. De Lyon, J. E. Jensen, B. Z. Nosho, J. A. Roth and J. R. Waterman, "Spectral crosstalk by radiative recombination in sequential-mode, dual mid-wavelength infrared band HgCdTe detectors," *J. Electron. Mater.* **33**, 517-525 (2004).

[87] J. Wang, J. Hu, P. Becla, A. Agarwal, and L. Kimerling, "Resonant-cavity-enhanced mid-infrared photodetector on a silicon platform," *Opt. Express* **18** (12), 12890-12896 (2010).

[88] J. Wang, J. Hu, X. Sun, P. Becla, A. Agarwal, and L. Kimerling, "Spectral selective mid-infrared detector on a silicon platform," in Group IV Photonics, (IEEE, 2009), FB7.

[89] M. Boberl, T. Fromherz, T. Schwarzl, G. Springholz, and W. Heiss, "IV–VI resonant-cavity enhanced photodetectors for the mid-infrared," *Semicond. Sci. Technol.* **19**, L115–L117 (2004).

[90] M. Arnold, D. Zimin, and H. Zogg, "Resonant-cavity-enhanced photodetectors for the mid-infrared," *Appl. Phys. Lett.* **87**, 141103 (2005).

[91] J. G. A. Wehner, C. A. Musca, R. H. Sewell, J. M. Dell, and L. Faraone, "Mercury cadmium telluride resonant-cavity-enhanced photoconductive infrared detectors," *Appl. Phys. Lett.* **87**, 211104 (2005).

[92] M. Hammer, K. R. Hiremath, and R. Stoffer, "Analytical approaches to the description of Optical Microresonator Devices," in *Microresonators as Building Blocks for VLSI Photonics,* F. Michelotti, A. Driessen, and M. Bertolotti, eds. (AIP Conference Proceedings, Melville, New York, 2004).

[93] http://sales.hamamatsu.com/assets/pdf/parts_P/p9696-02_etc_kird1073e02.pdf